NASA TM SX-806

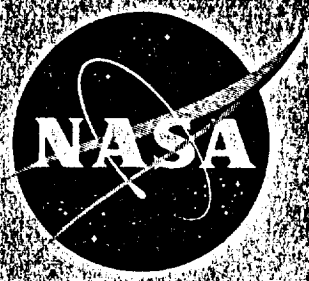

TECHNICAL MEMORANDUM

SX-806

for

Bureau of Naval Weapons, Department of the Navy

TRANSONIC STABILITY AND CONTROL CHARACTERISTICS OF A 1/9-SCALE MODEL OF A CANARD TARGET DRONE POWERED BY TWIN RAMJET ENGINES

By Theodore G. Ayers

Langley Research Center
Langley Station, Hampton, Va.

NATIONAL AERONAUTICS AND SPACE ADMINISTRATION
WASHINGTON
FEB 18 1963

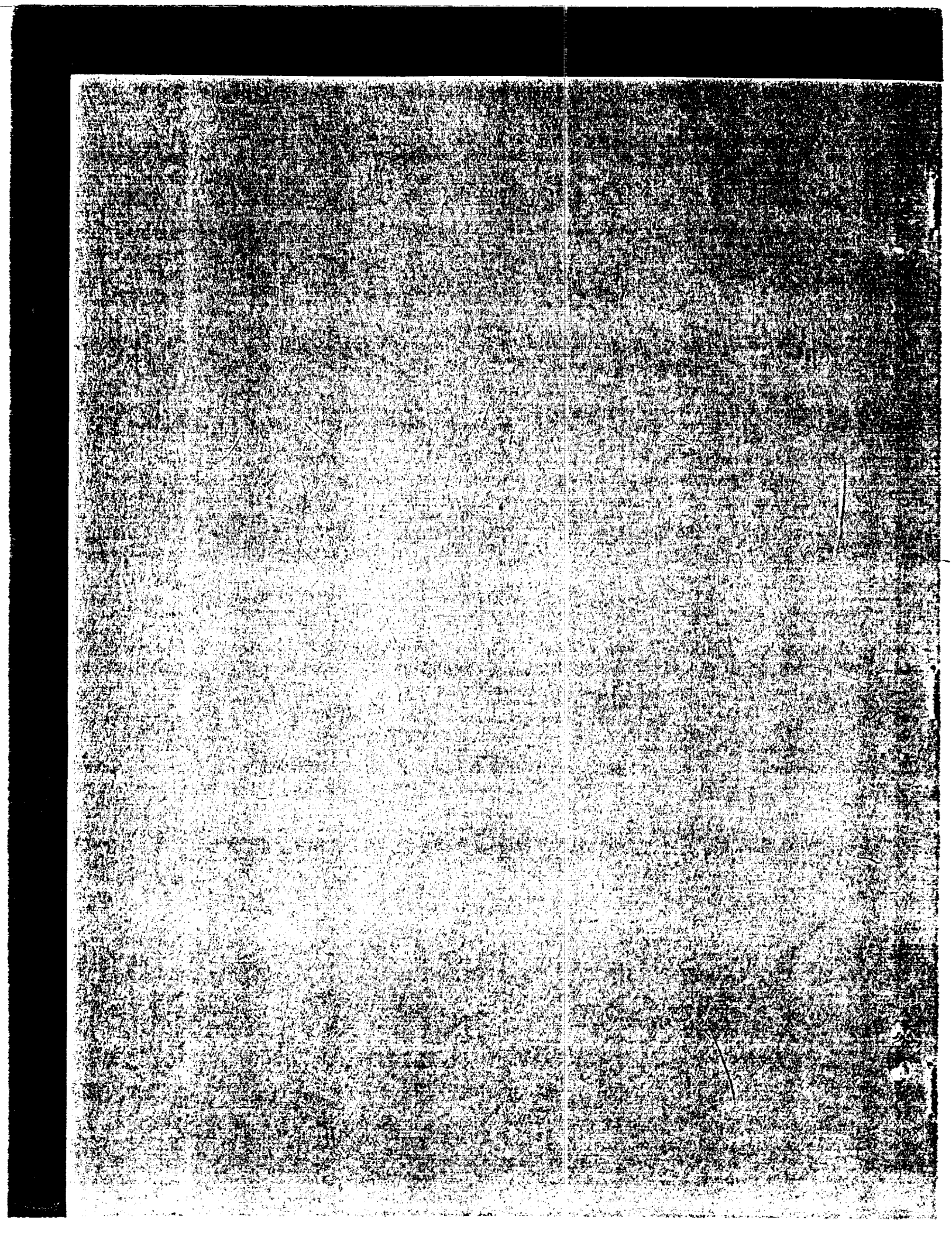

NATIONAL AERONAUTICS AND SPACE ADMINISTRATION

TECHNICAL MEMORANDUM SX-806

for

Bureau of Naval Weapons, Department of the Navy

TRANSONIC STABILITY AND CONTROL CHARACTERISTICS OF A 1/9-SCALE MODEL OF A CANARD TARGET DRONE POWERED BY TWIN RAMJET ENGINES

By Theodore G. Ayers

SUMMARY

An investigation has been conducted in the Langley 8-foot transonic pressure tunnel to determine the static longitudinal and lateral stability and control characteristics of a 1/9-scale model of a canard target drone powered by twin ramjet engines. The model was tested with and without twin simulated booster rockets, at Mach numbers from 0.60 to 1.20, over a range of angles of attack and sideslip.

Both model configurations demonstrate positive static longitudinal and lateral stability and control for the transonic Mach numbers at which they are expected to operate. A substantial difference between the stability levels of the two configurations was noted; this difference might cause some stability and trim problems if it exists at booster separation (Mach number of about 1.60).

Differentially extending a pair of off-on spoilers provided adequate roll control at small angles of attack, although adverse yawing moments occurred for the configuration without boosters at positive angles of attack. Reductions in the lateral control effectiveness at high positive and negative angles of attack cause the sideslip angles for which the rolling moments can be trimmed to become very small in some instances. Thus trim problems might be presented if flight should occur under conditions of sideslip.

INTRODUCTION

At the request of the Bureau of Naval Weapons, Department of the Navy, an investigation has been conducted at the Langley Research Center to determine the stability and control characteristics of a 1/9-scale model of a canard target drone at transonic and supersonic speeds. The drone is a canard configuration powered by twin ramjet sustainer engines mounted at the wing tips and is capable of operating at altitudes up to 65,000 feet in the Mach number range from 2.0 to

2.5. It is boosted to a Mach number of approximately 1.60 by twin booster rockets attached below the forward portion of the body. Pitch control is provided by a canard surface and lateral control is accomplished by off-on spoilers located outboard of the sustainer engines. No provision was made for directional control.

The purpose of this investigation was to determine whether or not the design of this drone was such that aerodynamic and control problems might be encountered through the speed range and to provide aerodynamic inputs to be used in making a complete dynamic-stability analysis of the drone through simulator studies. Two model configurations were investigated: the drone with boosters attached and the drone without boosters.

A brief summary of the data obtained at Mach numbers from 0.60 to 2.80 is presented in reference 1. It is the purpose of the present paper to supply the detailed results obtained at Mach numbers from 0.60 to 1.20.

SYMBOLS

The lift, drag, and pitching-moment coefficients presented in this paper are referred to the stability-axis system, whereas the rolling-moment, yawing-moment, and side-force coefficients are referred to the body-axis system. The moment reference center for the basic data was located on the center line of the drone body at a point 56.1 percent of the body length rearward of the nose, as shown in figure 1. The coefficients and symbols used herein are defined as follows:

A_b base area of body including sting and sting clearance, 0.02182 sq ft

A_i inlet area, 0.03221 sq ft

C_D drag coefficient, $\frac{\text{Drag}}{q_\infty S}$

$C_{D,b}$ base drag coefficient of body, $\frac{p - p_\alpha}{q_\infty S} A_b$

$C_{D,i}$ internal-drag coefficient, $\frac{\text{Internal drag}}{q_\infty S}$

C_L lift coefficient, $\frac{\text{Lift}}{q_\infty S}$

C_{L_α} lift-curve slope, $\frac{\partial C_L}{\partial \alpha}$, per deg

$C_{L,i}$ internal lift coefficient, $\frac{\text{Internal lift}}{q_\infty S}$

C_l	rolling-moment coefficient, $\frac{\text{Rolling moment}}{q_\infty S l}$
C_{l_β}	effective-dihedral derivative, $\frac{\Delta C_l}{\Delta \beta}$, per deg
C_m	pitching-moment coefficient, $\frac{\text{Pitching moment}}{q_\infty S c}$
$C_{m_{C_L}}$	longitudinal-stability derivative, $\frac{\partial C_m}{\partial C_L}$
$C_{m_{\delta_c}}$	canard effectiveness in pitch, $\frac{\partial C_m}{\partial \delta_c}$, per deg
C_n	yawing-moment coefficient, $\frac{\text{Yawing moment}}{q_\infty S l}$
C_{n_β}	directional-stability derivative, $\frac{\Delta C_n}{\Delta \beta}$, per deg
C_Y	side-force coefficient, $\frac{\text{Side force}}{q_\infty S}$
C_{Y_β}	side-force derivative, $\frac{\Delta C_Y}{\Delta \beta}$, per deg
c	reference chord, 7.52 in.
l	reference length, 7.52 in.
M	free-stream Mach number
p	static pressure, lb/sq ft
p_t	stagnation pressure, atm
q_∞	free-stream dynamic pressure, lb/sq ft
R	Reynolds number per foot
S	reference area of wing, 0.4106 sq ft
w	mass rate of air flow, slugs/sec
w/w_∞	mass-flow ratio based on inlet area
α	angle of attack referred to drone body reference line, deg

β angle of sideslip referred to plane of symmetry, deg

δ_c canard deflection referred to drone body reference line, deg

Subscript:

∞ free stream

APPARATUS AND PROCEDURES

Tunnel

The investigation was conducted in the Langley 8-foot transonic pressure tunnel, which is a single-return tunnel with a rectangular slotted test section that permits continuous operation through the transonic speed range. During the tests a constant stagnation temperature of 120° F was maintained by automatic temperature controls. The tunnel air was dried sufficiently to avoid condensation effects.

Model

A two-view drawing of the 1/9-scale model of the target drone with boosters attached is presented in figure 1, and photographs of the model with and without boosters are presented in figure 2.

The drone body was basically circular in cross section with a fineness ratio of approximately 19.5. A canard surface, which could be manually adjusted for a deflection range of ±10° in 5° increments, was located along the body center line near the nose of the model to provide pitch control. Lateral control was accomplished by a pair of off-on spoilers attached to the trailing edge of supplemental surfaces mounted outboard of the ramjet sustainer engines, as shown in figure 1. These spoilers could be manually set from an "off" position to a full "on" position by differentially extending them vertically, above and below the wing chord plane, to produce positive roll.

During a portion of the investigation, twin simulated booster rockets were attached below the forward portion of the drone body to simulate the boost phase of the target drone flight.

Tests

The wind-tunnel tests on the model with boosters were conducted at Mach numbers from 0.60 to 1.20, whereas those on the model without boosters were conducted at Mach numbers from 0.75 to 1.20. The model configurations were tested over an angle-of-attack range from -10° to 13°, at angles of sideslip of 0° and 5°. Lateral stability characteristics were determined over an angle-of-sideslip range from -2° to 6°, at angles of attack of -5°, 0°, and 10°. The free-stream

stagnation pressure was varied from 0.43 to 0.50 atmosphere and the Reynolds number per foot, shown in figure 3, varied from 1.35×10^6 to 2.11×10^6 over the Mach number range.

Measurements

Six-component static aerodynamic force and moment measurements were obtained by means of an electrical strain-gage balance sting-mounted within the drone body. The angles of attack and sideslip were determined by means of a gear-driven counter located at the base of the wind-tunnel sting-support system.

Flow measurements within the engine nacelle ducts were obtained for the model without boosters by means of pressure survey rakes, consisting of eight total-pressure and two static-pressure probes, located just inside each nacelle duct exit. The average measured variation of the mass-flow ratio, based on the model inlet area, is presented in figure 4. The internal lift and drag increments due to the change in the components of momentum of the flow through the nacelles were computed from the pressure measurements, and the results are presented in figure 5.

Base-pressure measurements were obtained from pressure probes located at the base of the drone body and the engine nacelle rims. The base drag of the drone body is presented for the model configuration with and without boosters in figures 6(a) and 6(b), respectively.

Corrections

Corrections for internal flow through the engine nacelle ducts have been applied to all lift, drag, and pitching-moment coefficients. The drag data have also been adjusted to the condition of free-stream static pressure acting at the drone-body base and the engine-nacelle exit rims.

The measured angles of attack and sideslip have been corrected for model support sting and balance deflections occurring upstream of the angle-measurement device as the result of aerodynamic loads on the model.

The static longitudinal-stability derivative $C_{m_{C_L}}$ and the static directional-stability derivative C_{n_β} were obtained by transferring the basic data to the proper center-of-gravity location of each configuration. These locations are as follows:

	Model station, in.
Model with boosters	20.3
Model without boosters	24.8

No corrections for wind-tunnel boundary-reflected disturbances were considered necessary for the Mach numbers at which the tests were conducted.

Accuracies

The accuracy of the data presented for this investigation at a Mach number of 0.90 is estimated to be as follows:

C_L	±0.010
C_D	±0.002
C_m	±0.004
C_l	±0.001
C_n	±0.004
C_Y	±0.010
M	±0.002

The angles of attack and sideslip are estimated to be correct to within ±0.1°.

PRESENTATION OF RESULTS

The results of this investigation are presented in the following figures:

DISCUSSION

Longitudinal Stability and Control

The values of the static longitudinal-stability derivative, shown in figure 23, were obtained by transferring the basic data to the proper center-of-gravity location for each configuration. The data indicate that both configurations are statically stable for the transonic Mach numbers at which they are expected to operate. There is, however, a substantial difference between the stability levels of the two configurations at a Mach number of 1.20, and the supersonic data of reference 1 indicate that at the point of booster separation ($M \approx 1.60$) this stability-level difference still persists.

The effectiveness of the canard in providing pitch control is shown in figure 24, for the model with and without boosters, at $C_L = 0$ and 0.40. The data indicate that the pitch-control effectiveness for the model with boosters was substantially less than that for the model without boosters at the higher Mach numbers because of interference effects caused by the boosters being located near the canard. It can also be seen that at $C_L = 0.40$ the pitch-control effectiveness for the model without boosters is considerably less at the subsonic Mach numbers than at the supersonic Mach numbers. The basic pitching-moment characteristics for this configuration, shown in figure 8, indicate that for Mach numbers of 0.75 and 0.90, increasing the canard incidence from 5° to 10° results in little or no change in pitching moment for lift coefficients above about 0.20. It is probable that the loss in pitch effectiveness is caused by separation of the flow over the sharp leading edge of the canard at the lower Mach numbers.

Lateral Stability and Control

The variation of the effective-dihedral derivative C_{l_β} with angle of attack is presented in figure 25(a) for the model with and without boosters. Both model configurations had positive effective dihedral $\left(-C_{l_\beta}\right)$ at angles of attack greater than about 2° throughout the Mach number range of the tests, and the values indicated at Mach numbers of 1.00 and 1.20 are nearly the same for the two configurations.

The variation of the directional-stability derivative C_{n_β} with angle of attack is shown for the model with and without boosters in figure 25(b). The

values of C_{n_β} presented in this figure were obtained by transferring the basic data to the proper center-of-gravity location of each configuration. In general, the results indicate that both model configurations demonstrated positive directional stability throughout the Mach number and angle-of-attack ranges of the test. It should be noted, however, that C_{n_β} decreases rapidly with both positive and negative increases in angle of attack for the model configuration with boosters. The limited data for the model configuration without boosters indicate a less rapid decrease in C_{n_β} with angle of attack because of the increased effectiveness of the lower vertical tail at the higher angles of attack.

The side-force derivative C_{Y_β} for both model configurations was only slightly affected by changes in Mach number and angle of attack, as shown in figure 25(c), and the values were about the same for the two configurations.

The spoilers were differentially extended, on both model configurations, to produce positive roll in order to investigate the lateral-control effectiveness. The data are presented for the model with and without boosters at zero sideslip in figures 9 and 10, respectively. Positive lateral-control effectiveness is indicated for both configurations, and the value remained nearly constant through an angle-of-attack range of about $\pm 5^\circ$. Positive or negative increases in angle of attack beyond this range resulted in substantial reductions in the lateral-control effectiveness. Although differentially extending the spoilers produced favorable rolling moments for both configurations, the resulting yawing moments were adverse for the configuration without boosters at positive angles of attack, as shown in figure 10. Data included in reference 1 indicate that this adverse yaw due to the spoilers occurs for both configurations at the Mach number of booster separation ($M \approx 1.60$). The effect of the spoilers on the aerodynamic characteristics in sideslip for the model with boosters at $\alpha \approx -6^\circ$ and without boosters at $\alpha \approx 11^\circ$ are shown in figures 21 and 22, respectively. The data indicate that, at the higher Mach numbers, rolling moments cannot be trimmed for sideslip angles greater than about $\pm 2^\circ$. Although flight under conditions of sideslip is not anticipated, such conditions might occur as the result of booster separation or asymmetric thrust from the booster or sustainer engines.

CONCLUDING REMARKS

An investigation has been conducted in the Langley 8-foot transonic pressure tunnel to determine the static longitudinal and lateral stability and control characteristics of a 1/9-scale model of a canard target drone powered by twin ramjet engines. The model was tested with and without twin simulated booster rockets, at Mach numbers from 0.60 to 1.20, over a range of angles of attack and sideslip.

Both model configurations demonstrate positive static longitudinal and lateral stability and control for the transonic Mach numbers at which they are expected to operate. A substantial difference between the stability levels of the two configurations was noted; this difference might cause some stability and trim problems if it exists at booster separation (Mach number of about 1.60).

Differentially extending a pair of off-on spoilers provided adequate roll control at small angles of attack, although adverse yawing moments occurred for the configuration without boosters at positive angles of attack. Reductions in the lateral control effectiveness at high positive and negative angles of attack cause the sideslip angles for which the rolling moments can be trimmed to become very small in some instances. Thus trim problems might be presented if flight should occur under conditions of sideslip.

Langley Research Center,
National Aeronautics and Space Administration,
Langley Station, Hampton, Va., January 23, 1963.

REFERENCE

1. Spearman, M. Leroy: Longitudinal and Lateral Stability and Control Characteristics of a 1/9-Scale Model of a Twin-Ramjet Canard Target Drone at Mach Numbers From 0.60 to 2.80. NASA TM SX-732, 1962.

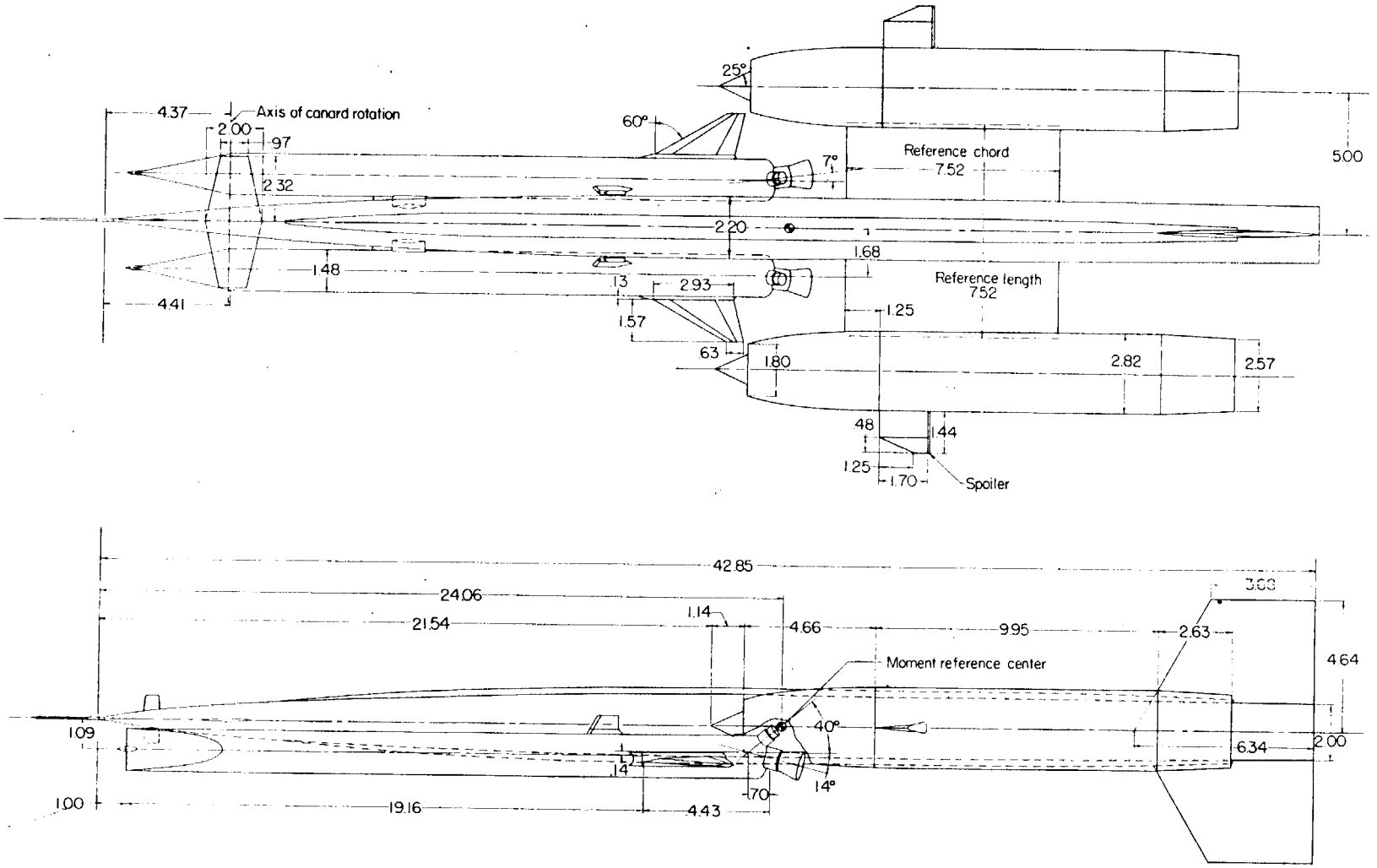

Figure 1.- Two-view drawing of model with boosters attached. All linear dimensions are in inches unless otherwise specified.

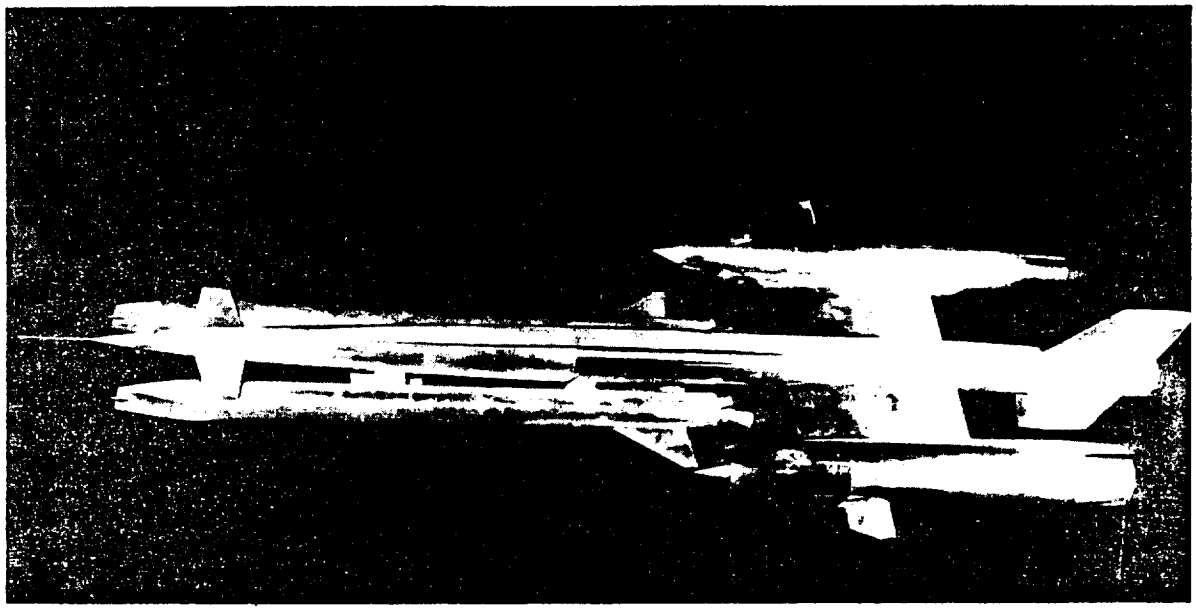

Three-quarter front view L-61-8092

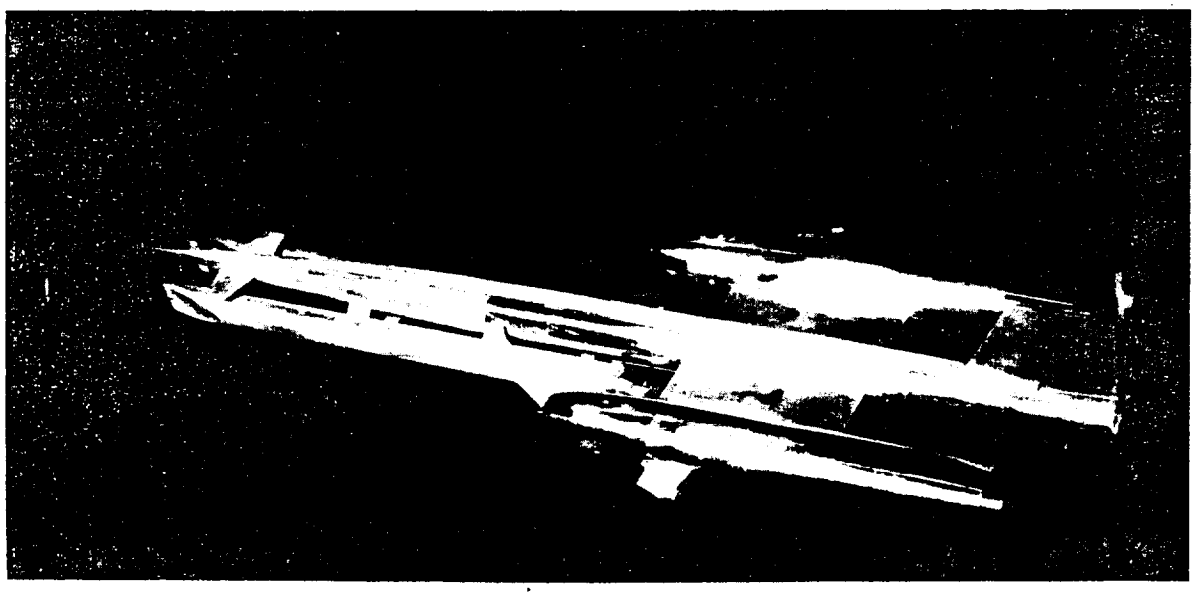

Three-quarter rear view L-61-8091

(a) Model with boosters.

Figure 2.- Photographs of model.

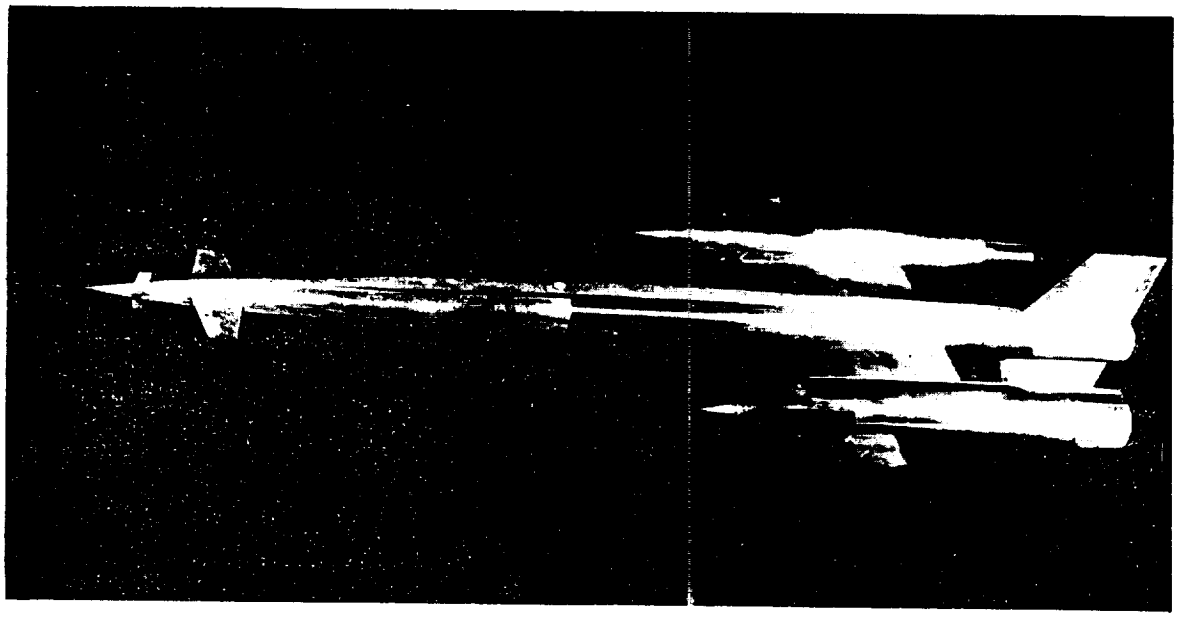

Three-quarter front view L-61-8090

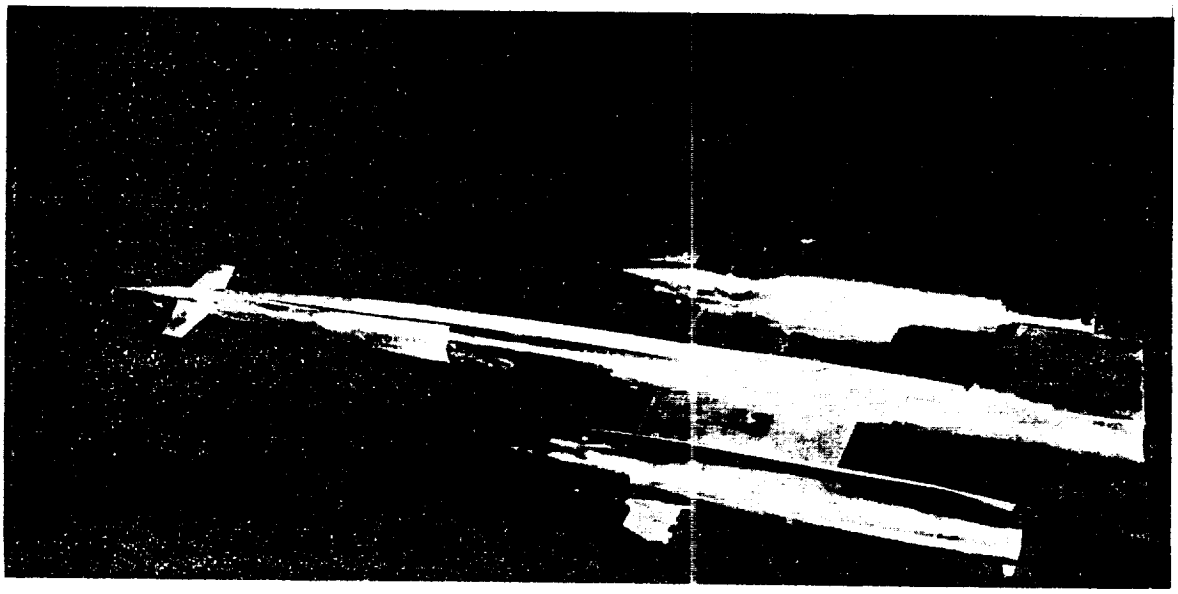

Three-quarter rear view L-61-8089

(b) Model without boosters.

Figure 2.- Concluded.

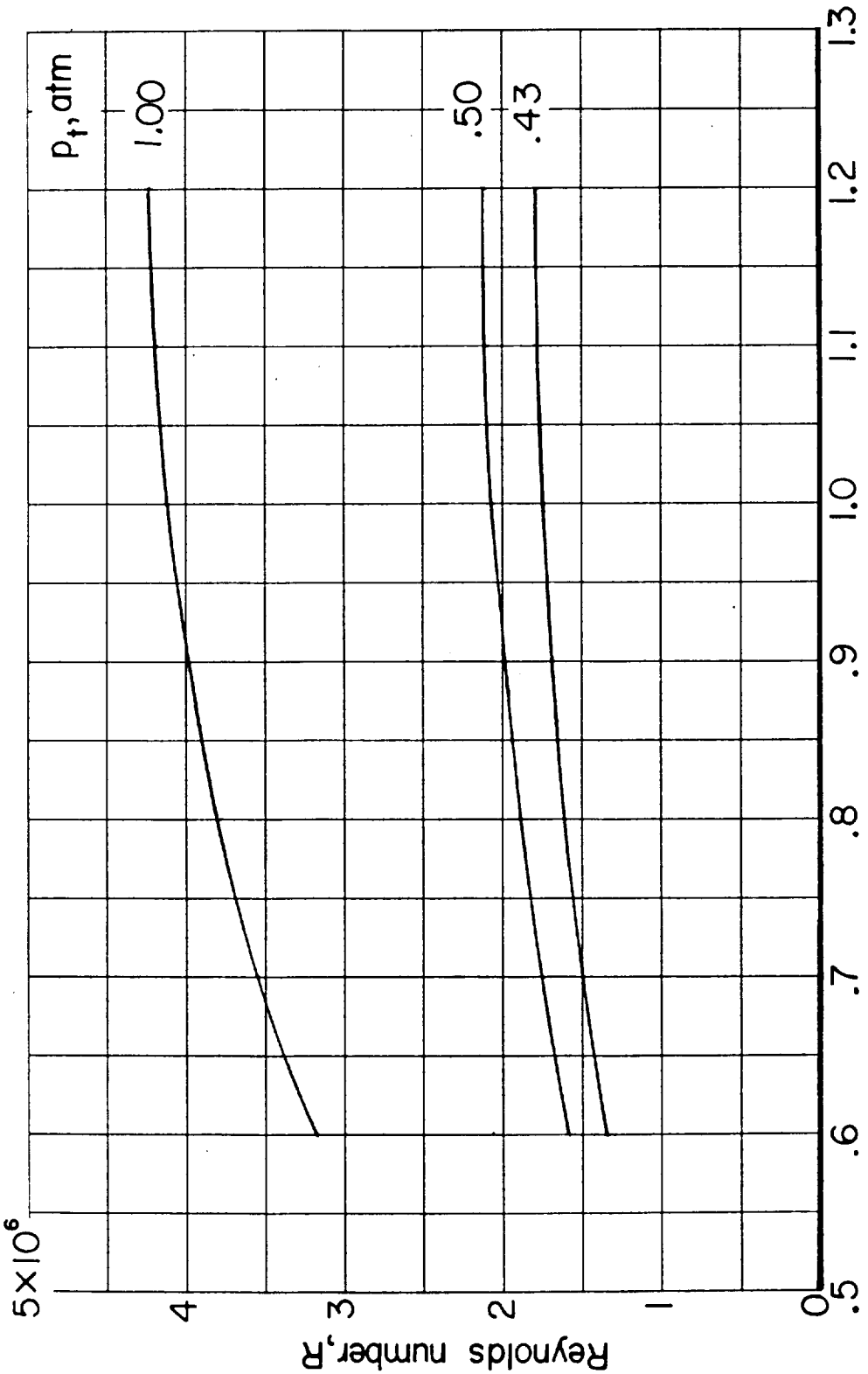

Figure 3.- Variation with Mach number of Reynolds number per foot for tests in the Langley 8-foot transonic pressure tunnel.

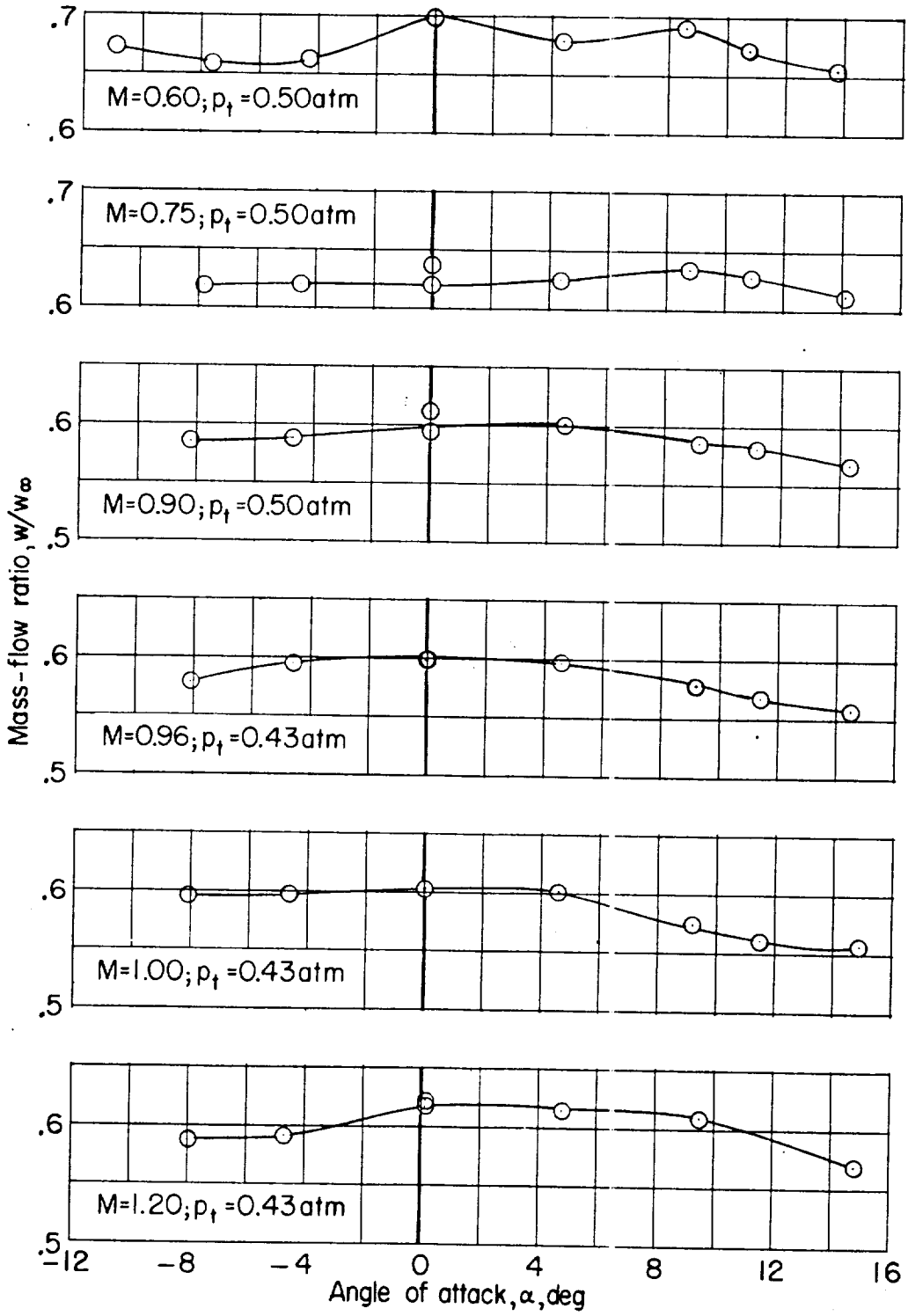

Figure 4.- Variation of mass-flow ratio (based on inlet area) with angle of attack for model without boosters.

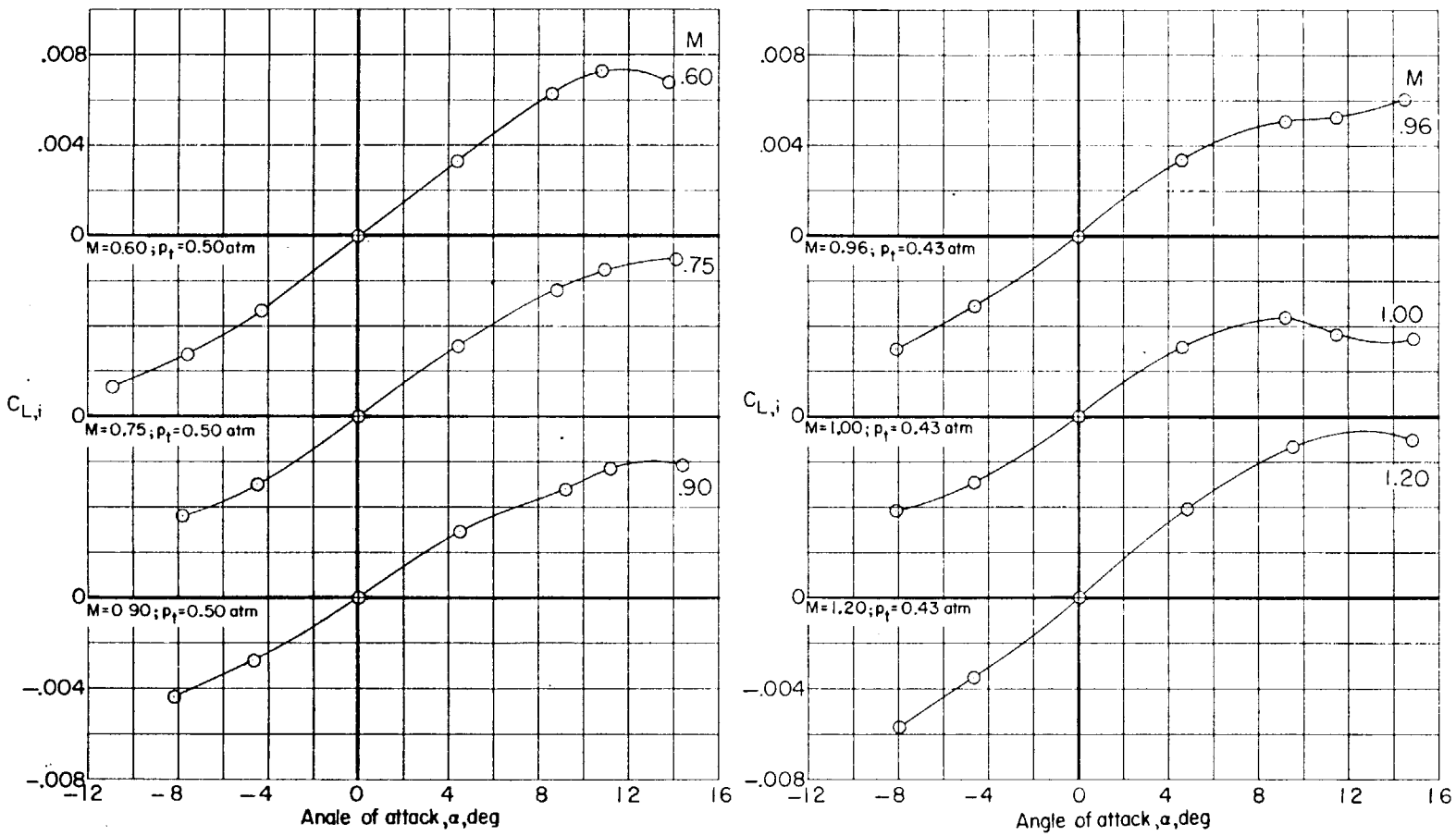

(a) Internal-lift coefficient.

Figure 5.- Variation of internal-force coefficients with angle of attack for model without boosters.

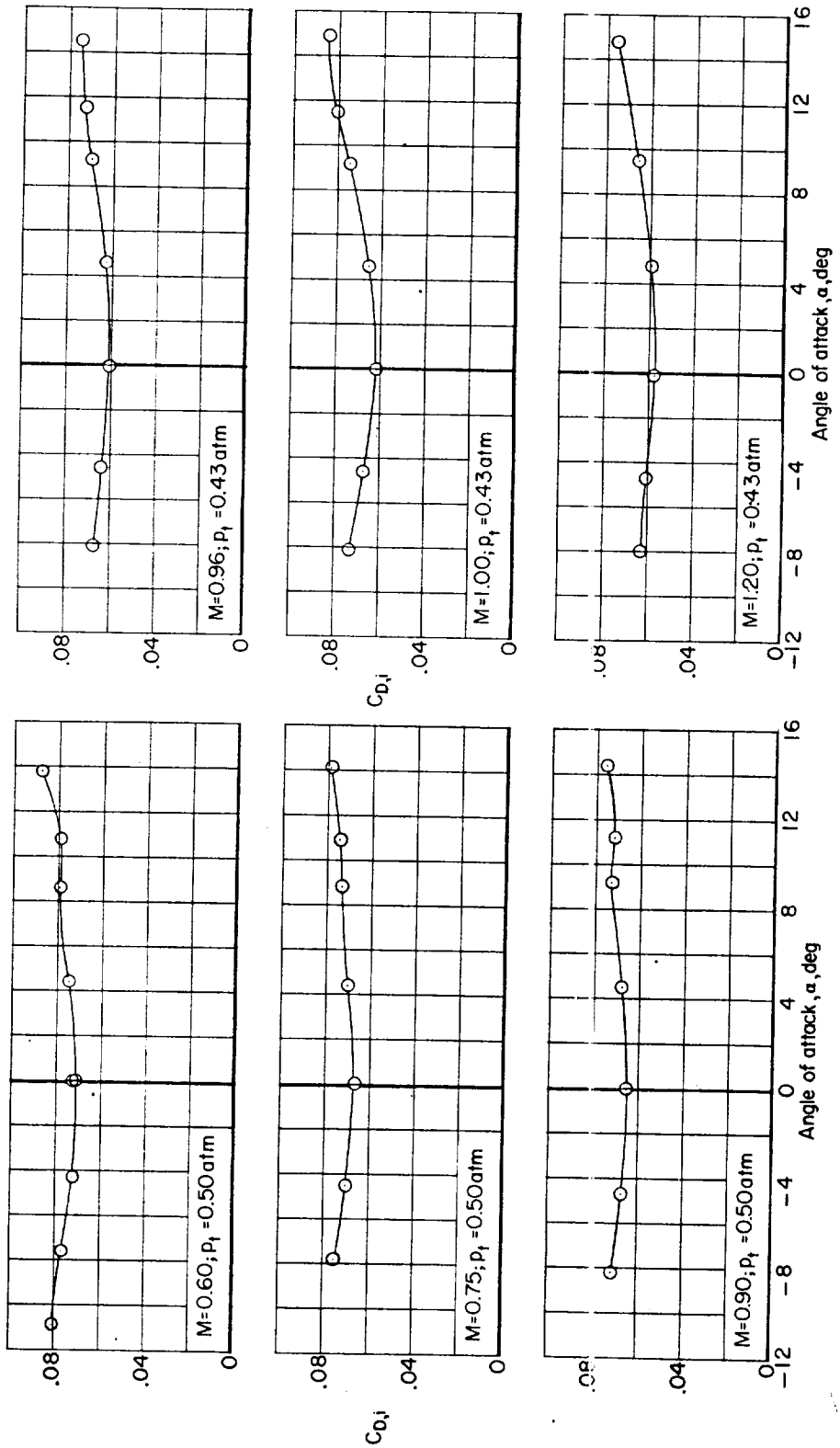

(b) Internal-drag coefficient.

Figure 5.- Concluded.

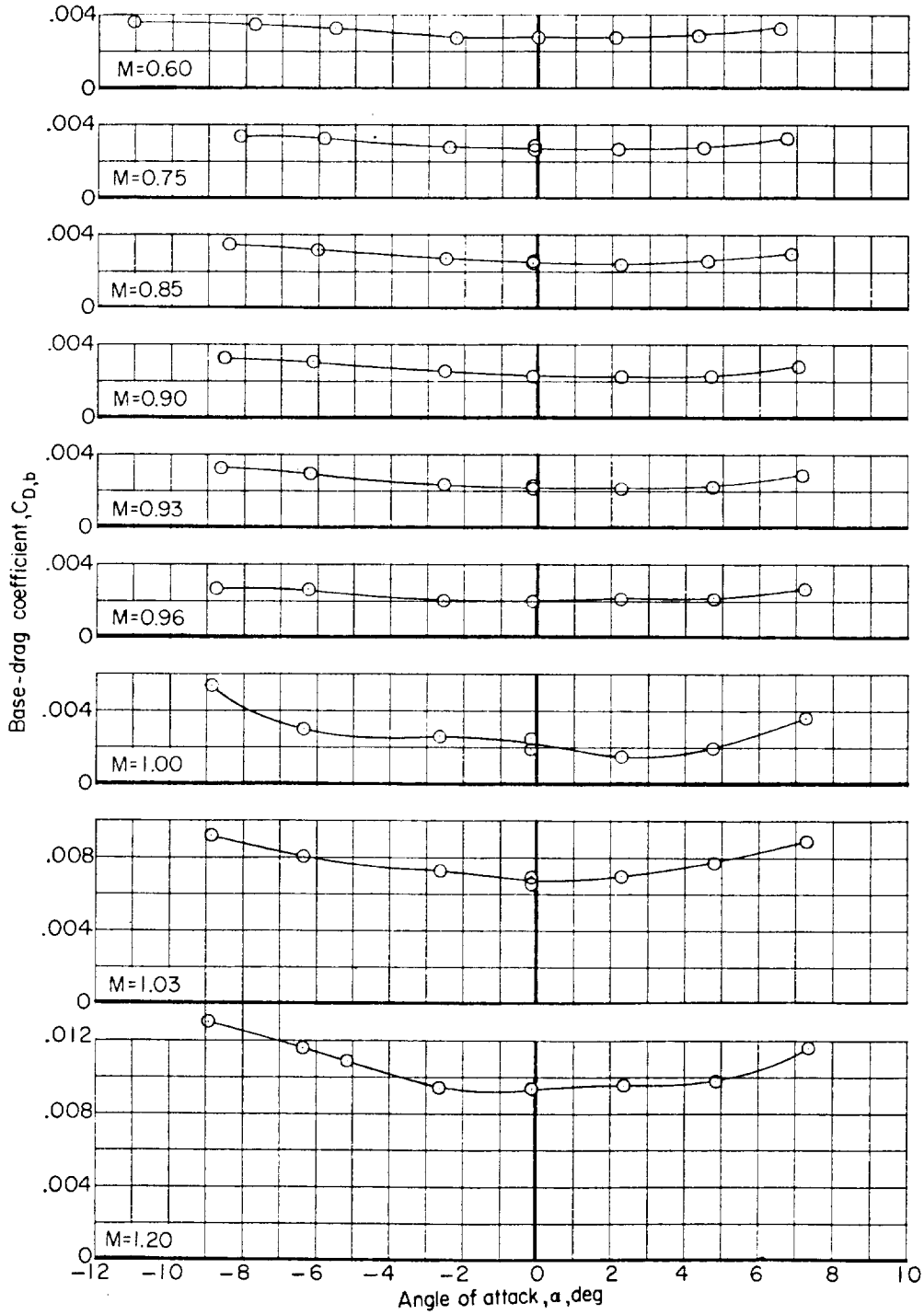

(a) Model with boosters. p_t = 0.50 atm.

Figure 6.- Variation of base-drag coefficient with angle of attack.

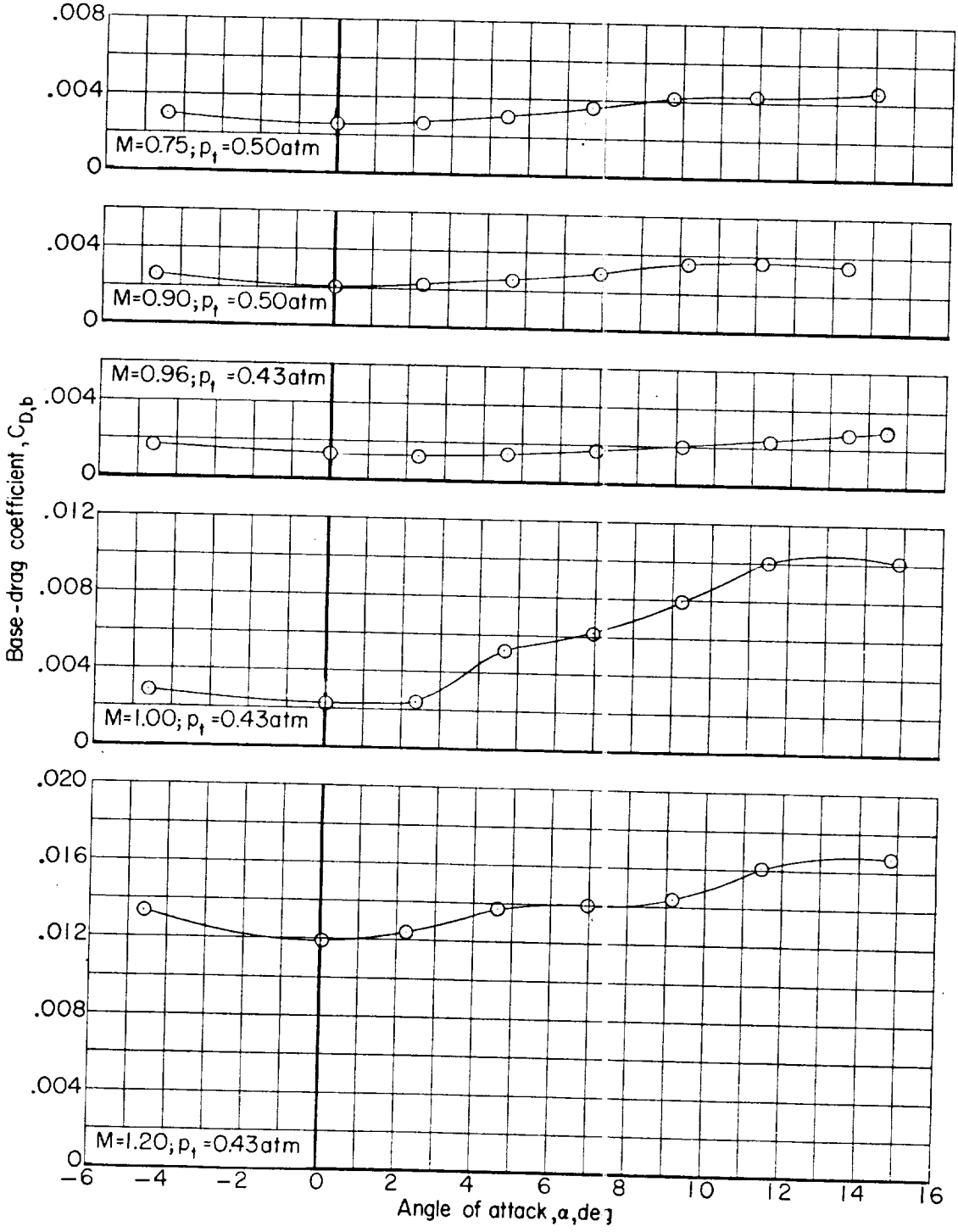

(b) Model without boosters.

Figure 6.- Concluded.

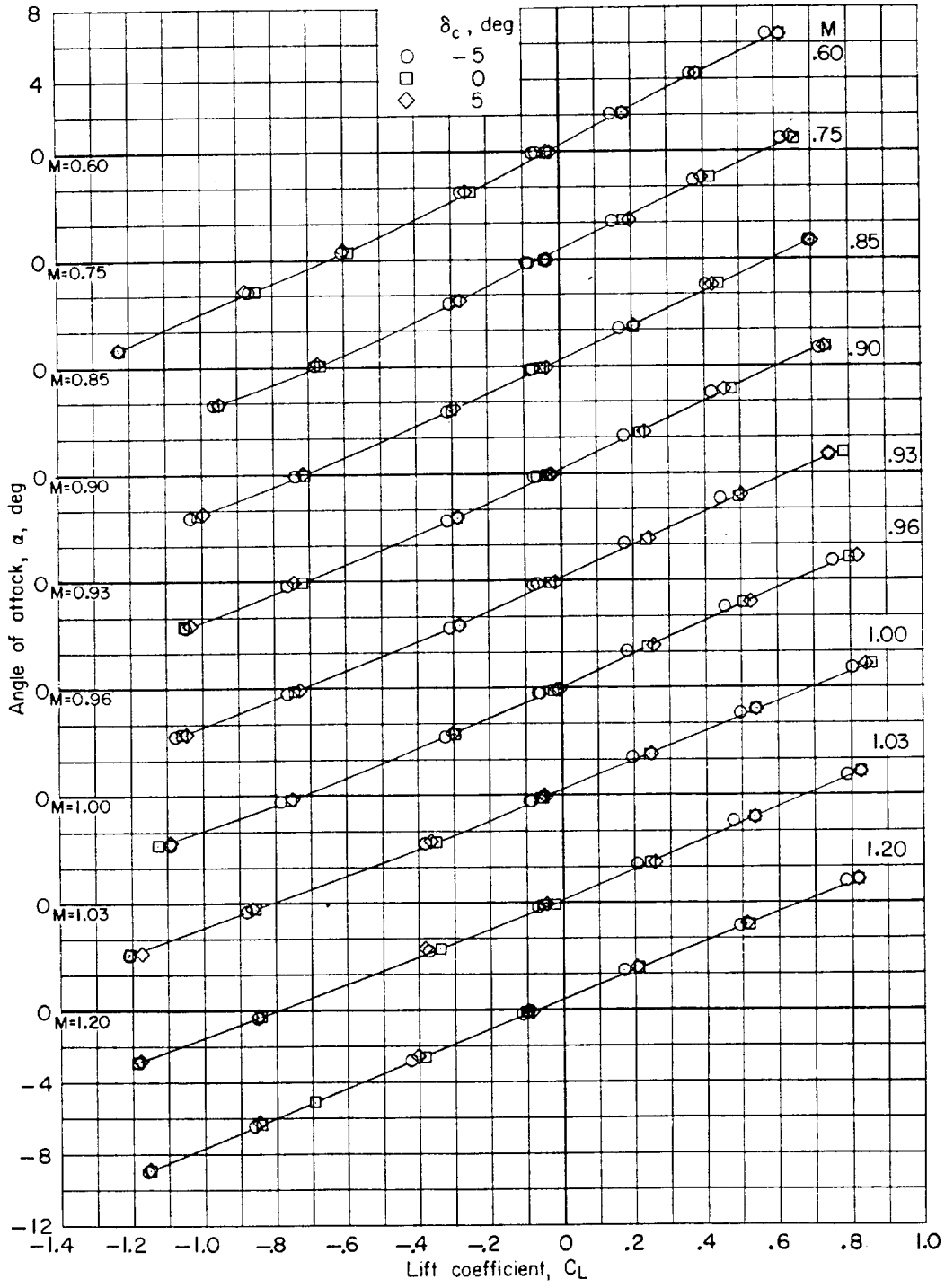

(a) Angle of attack.

Figure 7.- Effect of canard deflection on the basic aerodynamic characteristics for model with boosters. $\beta = 0^\circ$; $p_t = 0.50$ atm.

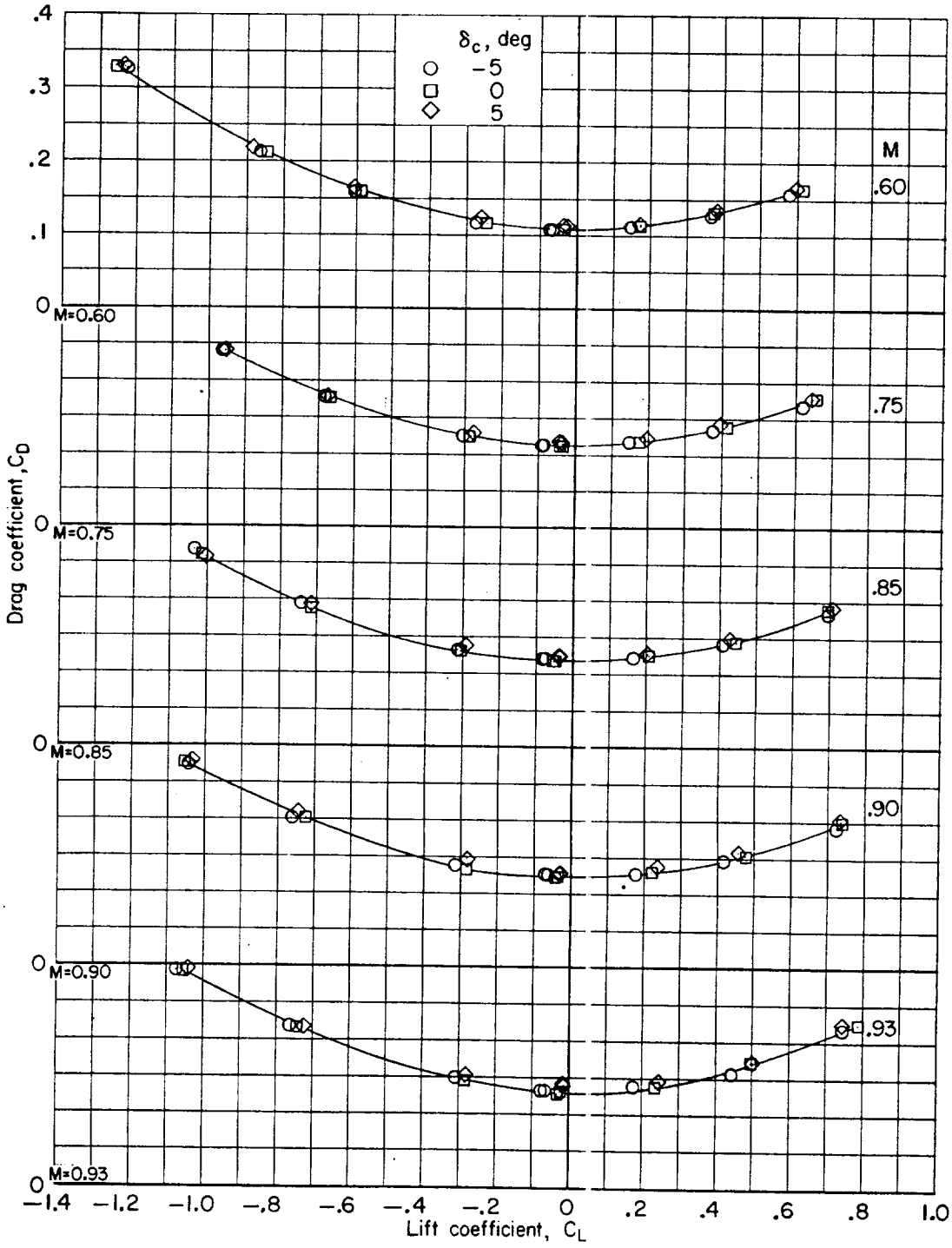

(b) Drag coefficient.

Figure 7.- Continued.

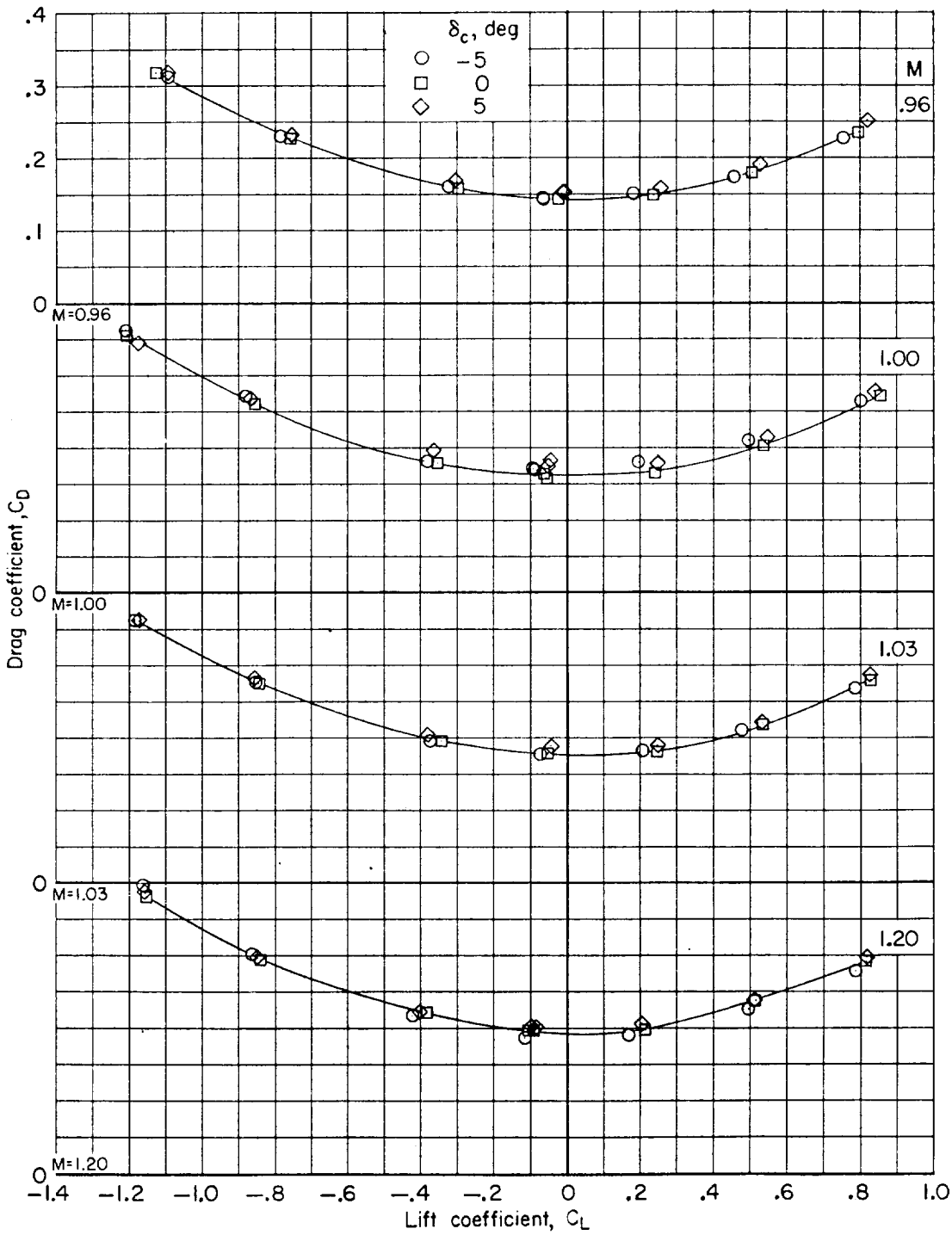

(b) Drag coefficient. Concluded.

Figure 7.- Continued.

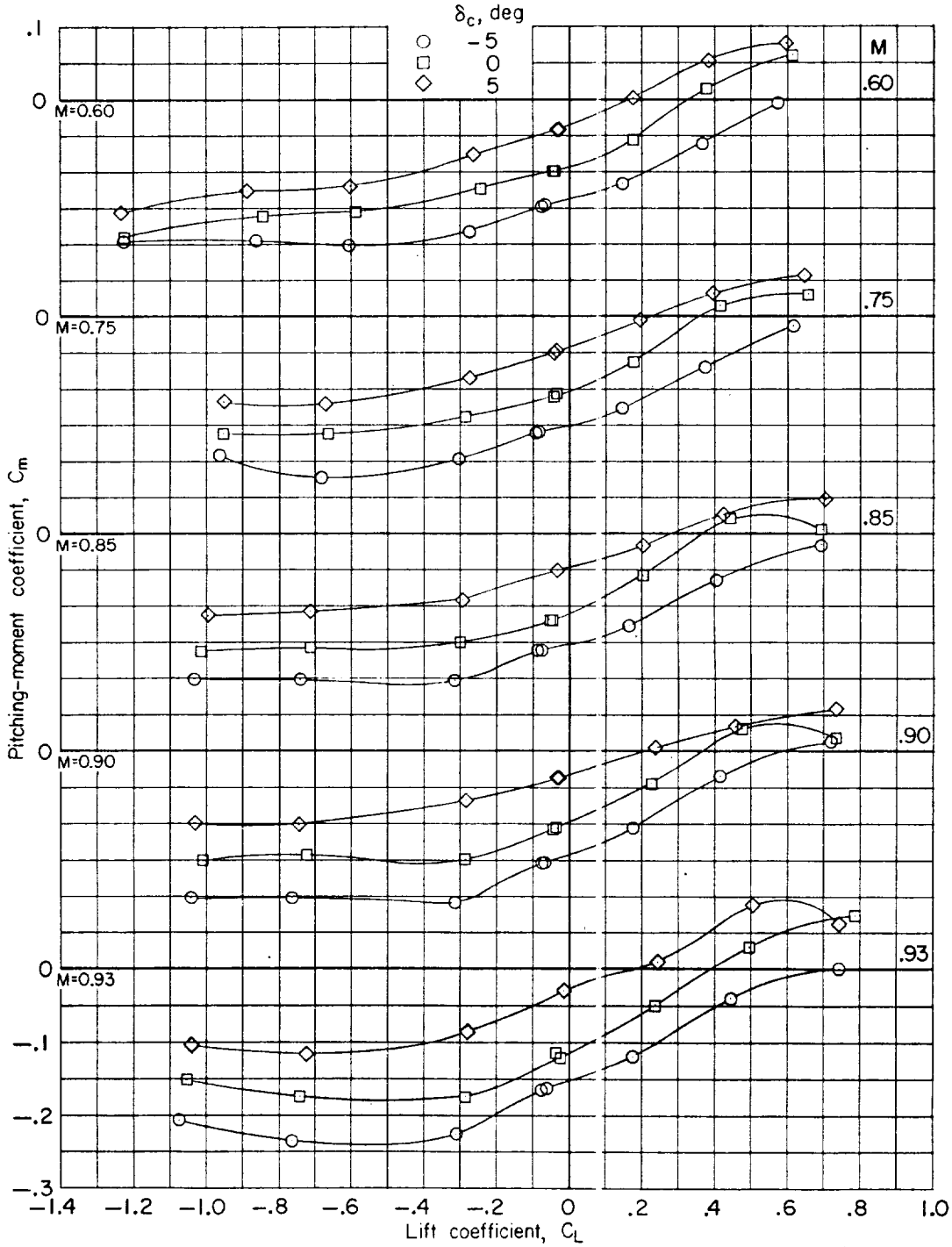

(c) Pitching-moment coefficient.

Figure 7.- Continued.

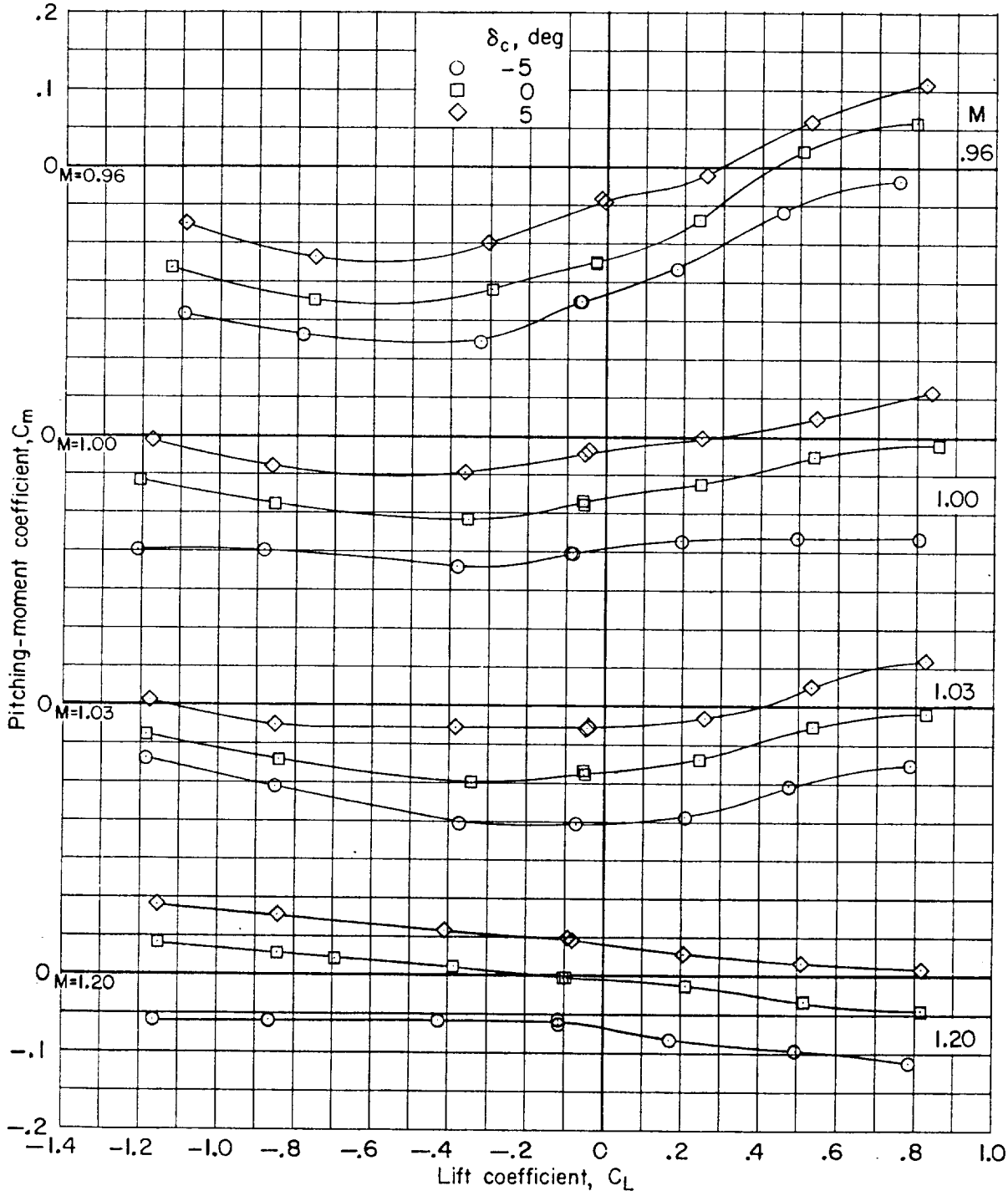

(c) Pitching-moment coefficient. Concluded.

Figure 7.- Concluded.

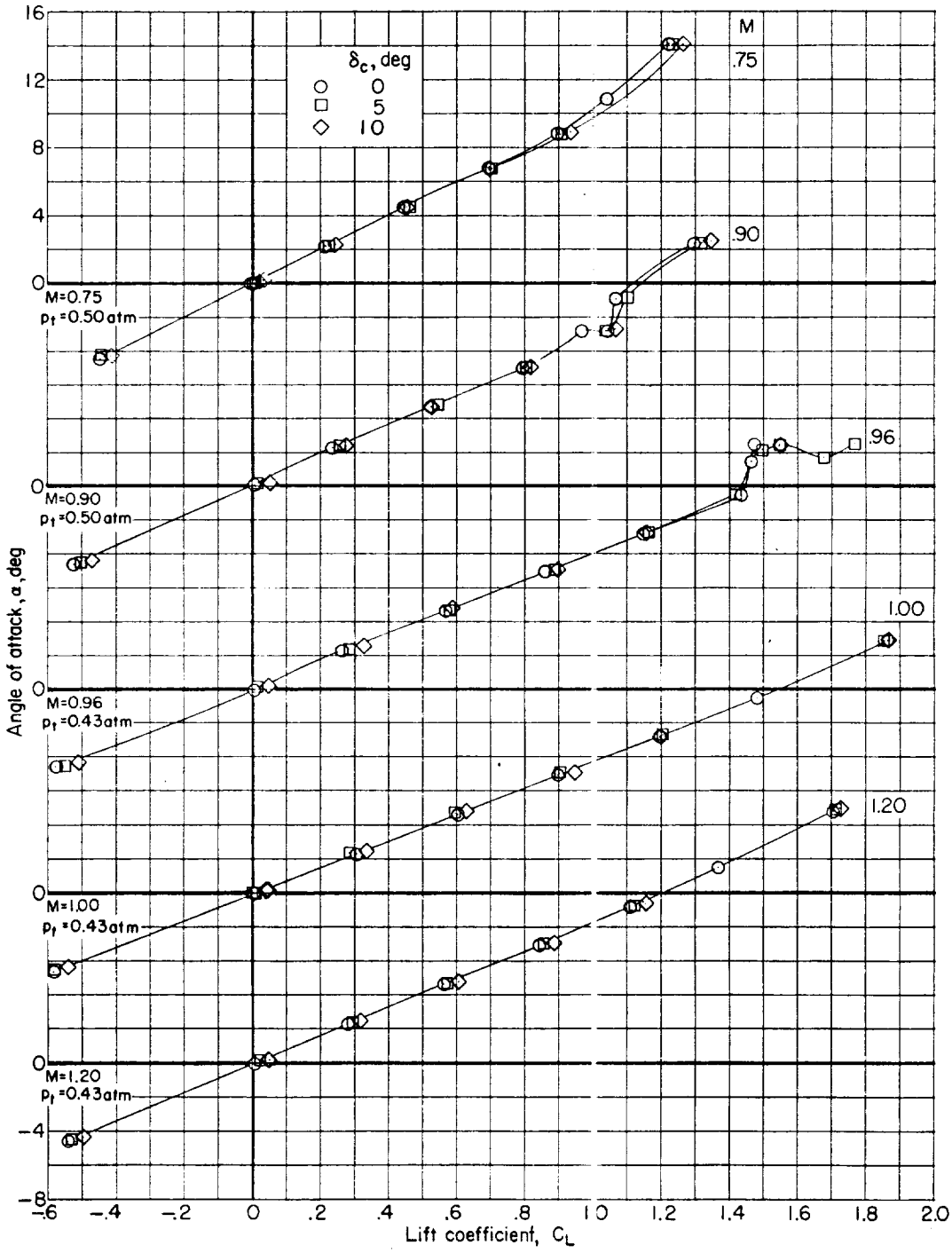

(a) Angle of attack

Figure 8.- Effect of canard deflection on the basic aerodynamic characteristics for model without boosters. $\beta = 0^\circ$.

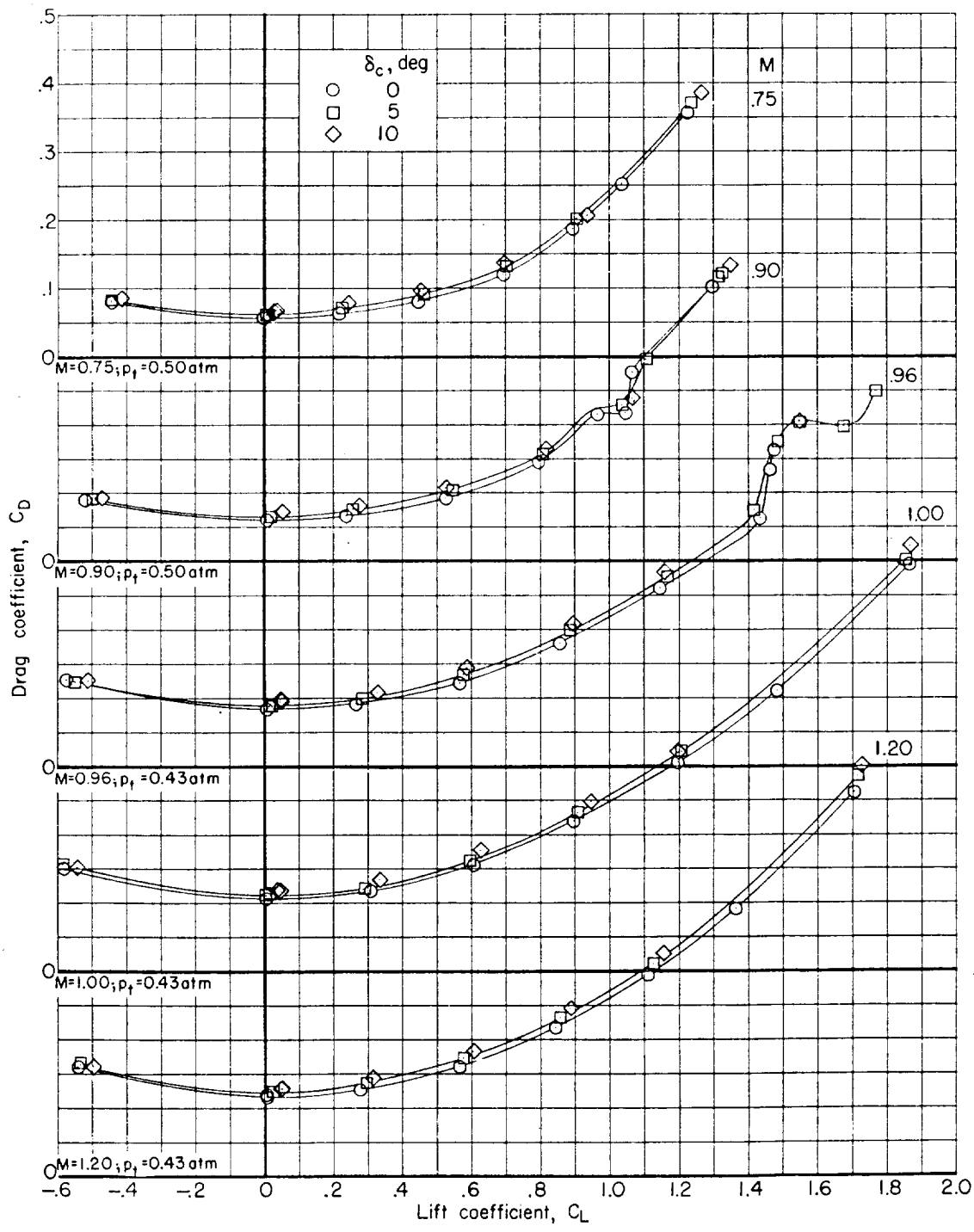

(b) Drag coefficient.

Figure 8.- Continued.

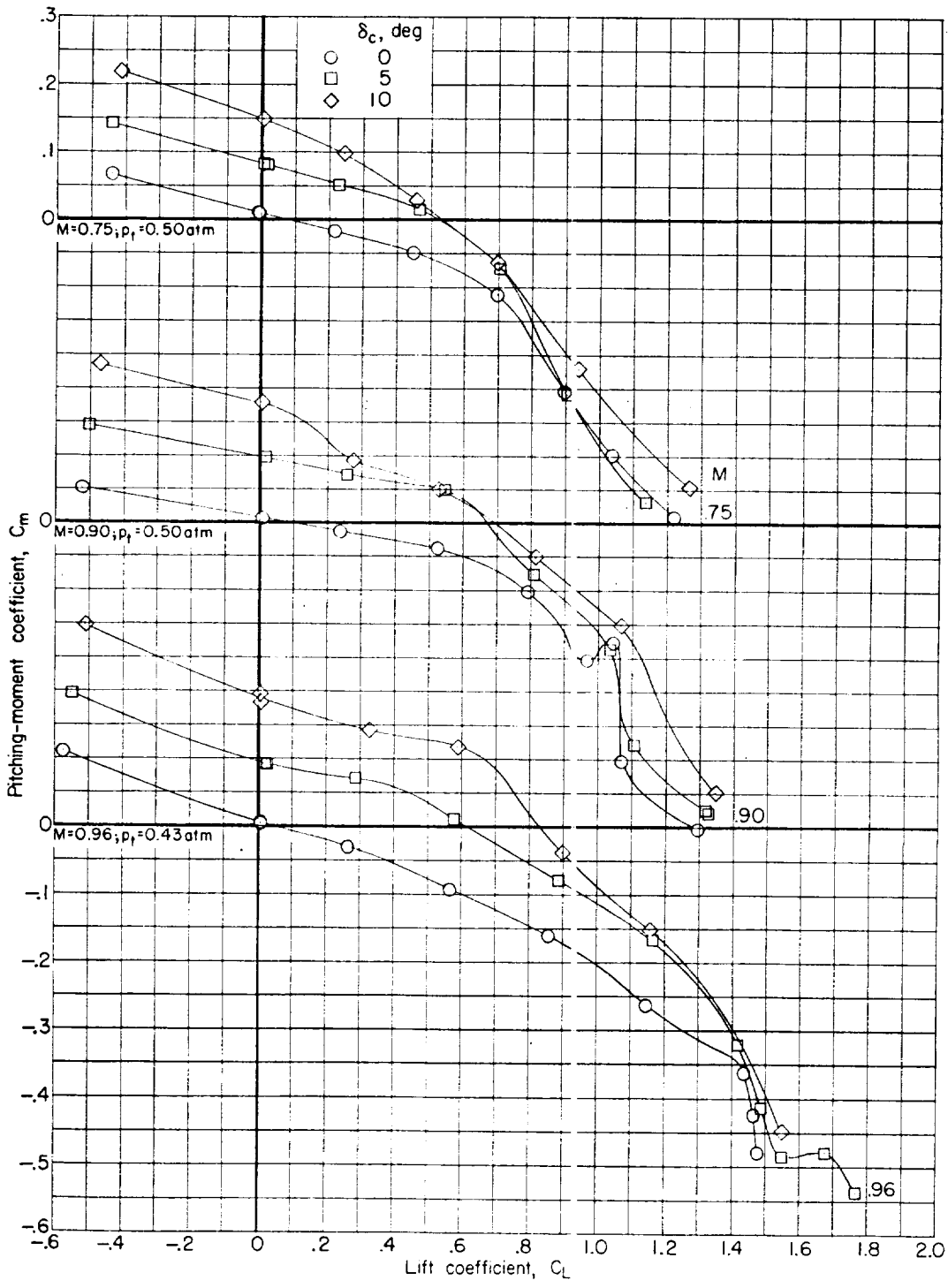

(c) Pitching-moment coefficient.

Figure 8.- Continued.

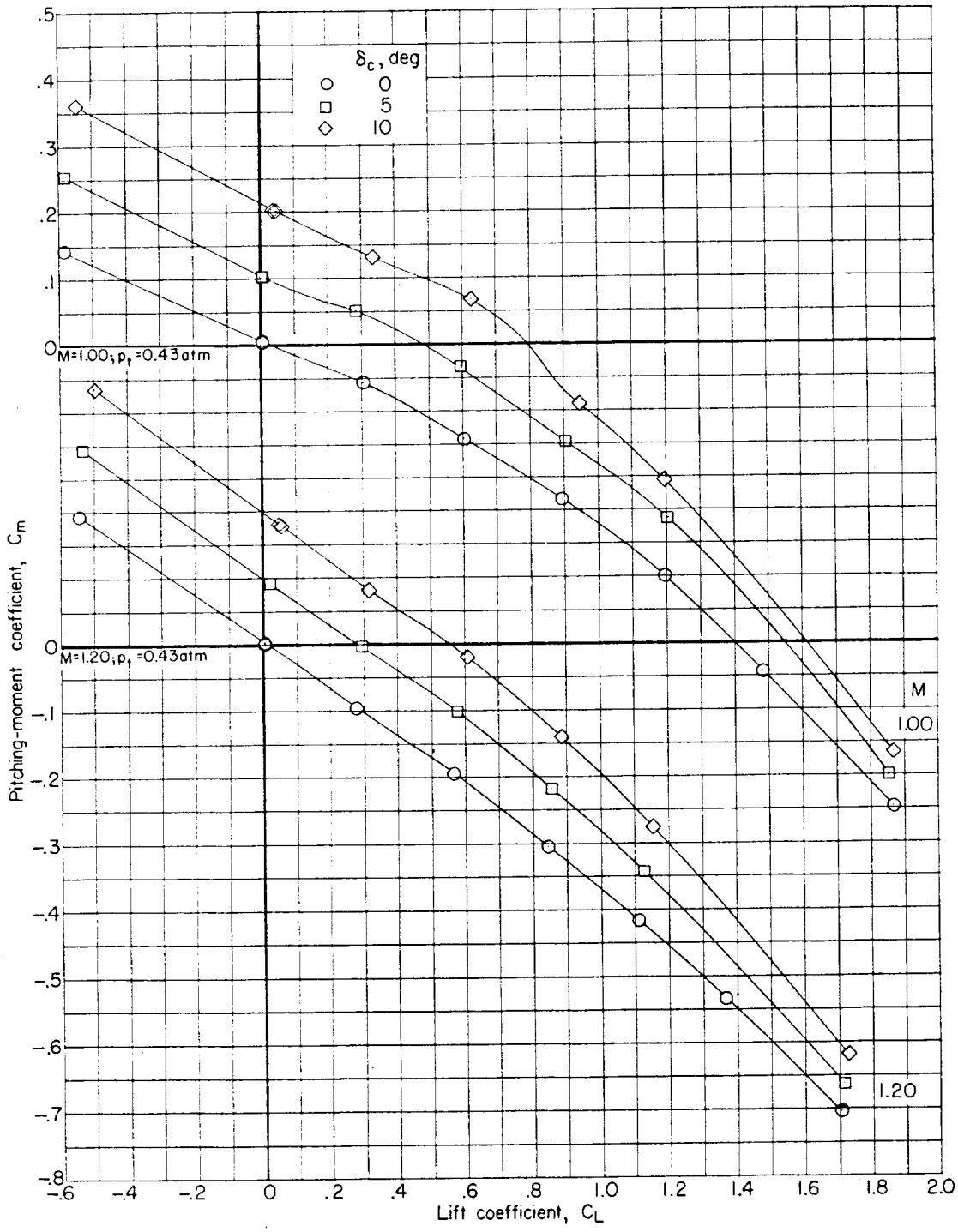

(c) Pitching-moment coefficient. Concluded.

Figure 8.- Concluded.

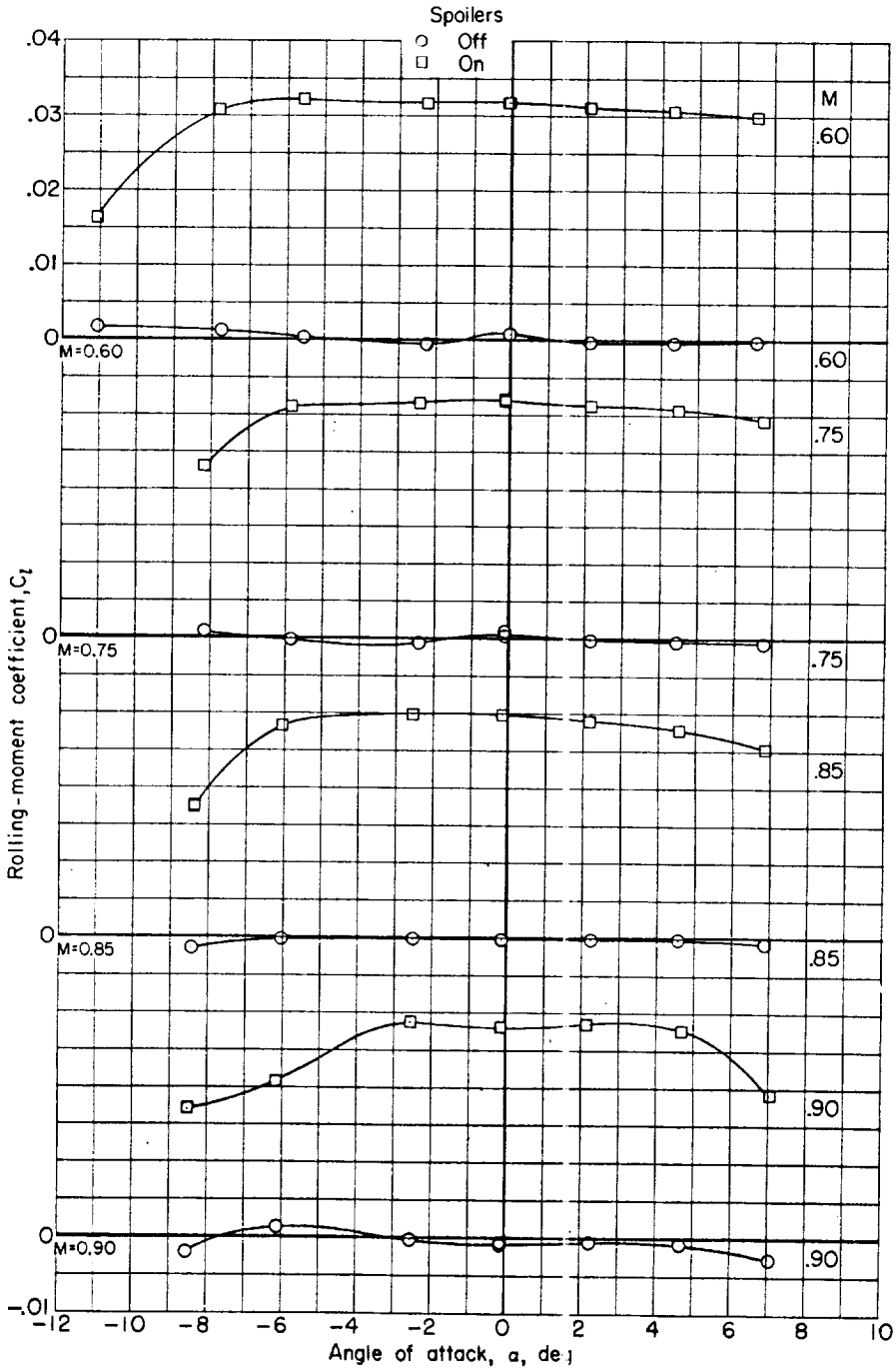

(a) Rolling-moment coefficient.

Figure 9.- Effect of spoilers on the aerodynamic characteristics for model with boosters. $\beta = 0°$; $p_t = 0.50$ atm.

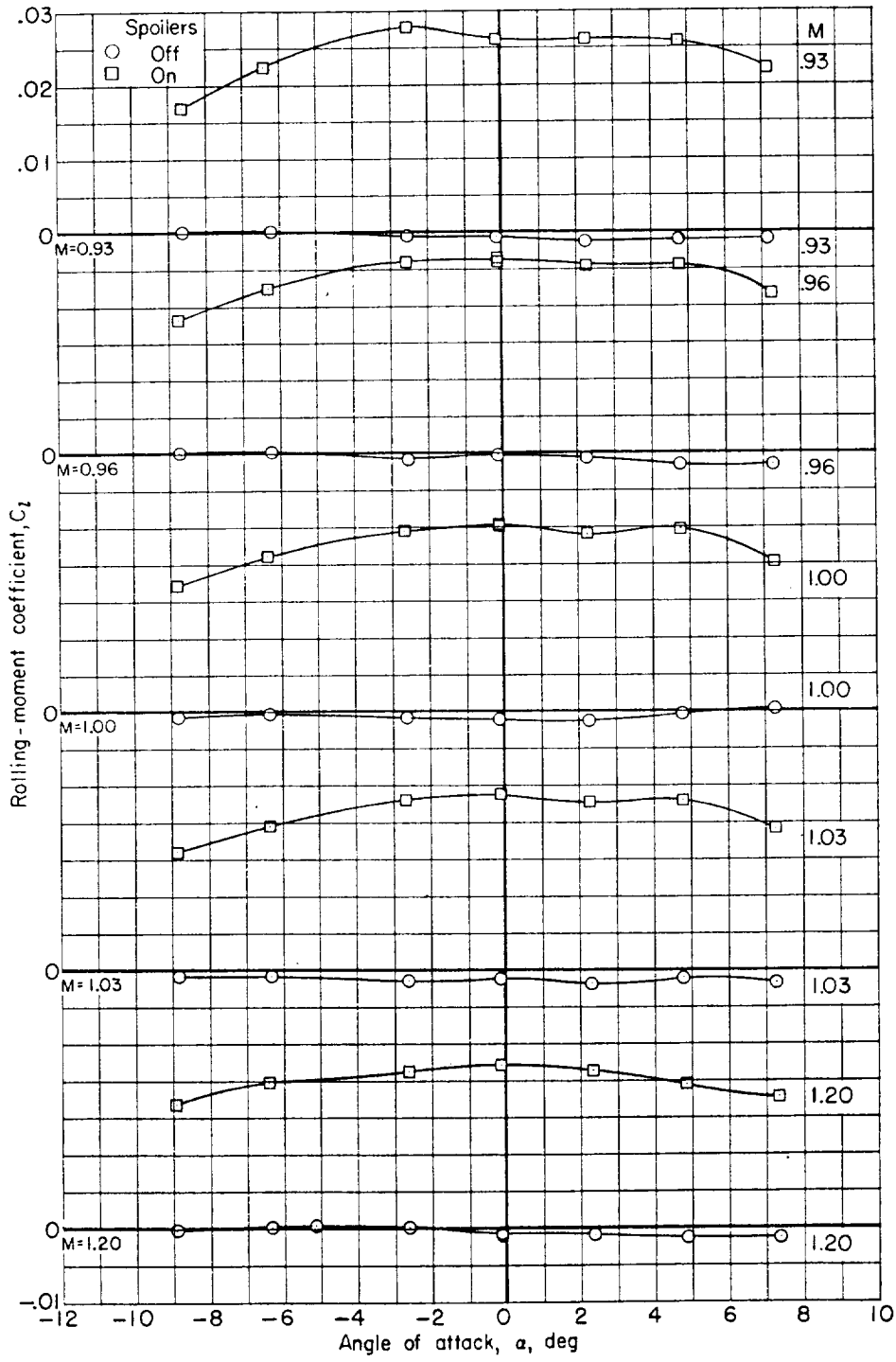

(a) Rolling-moment coefficient. Concluded.

Figure 9.- Continued.

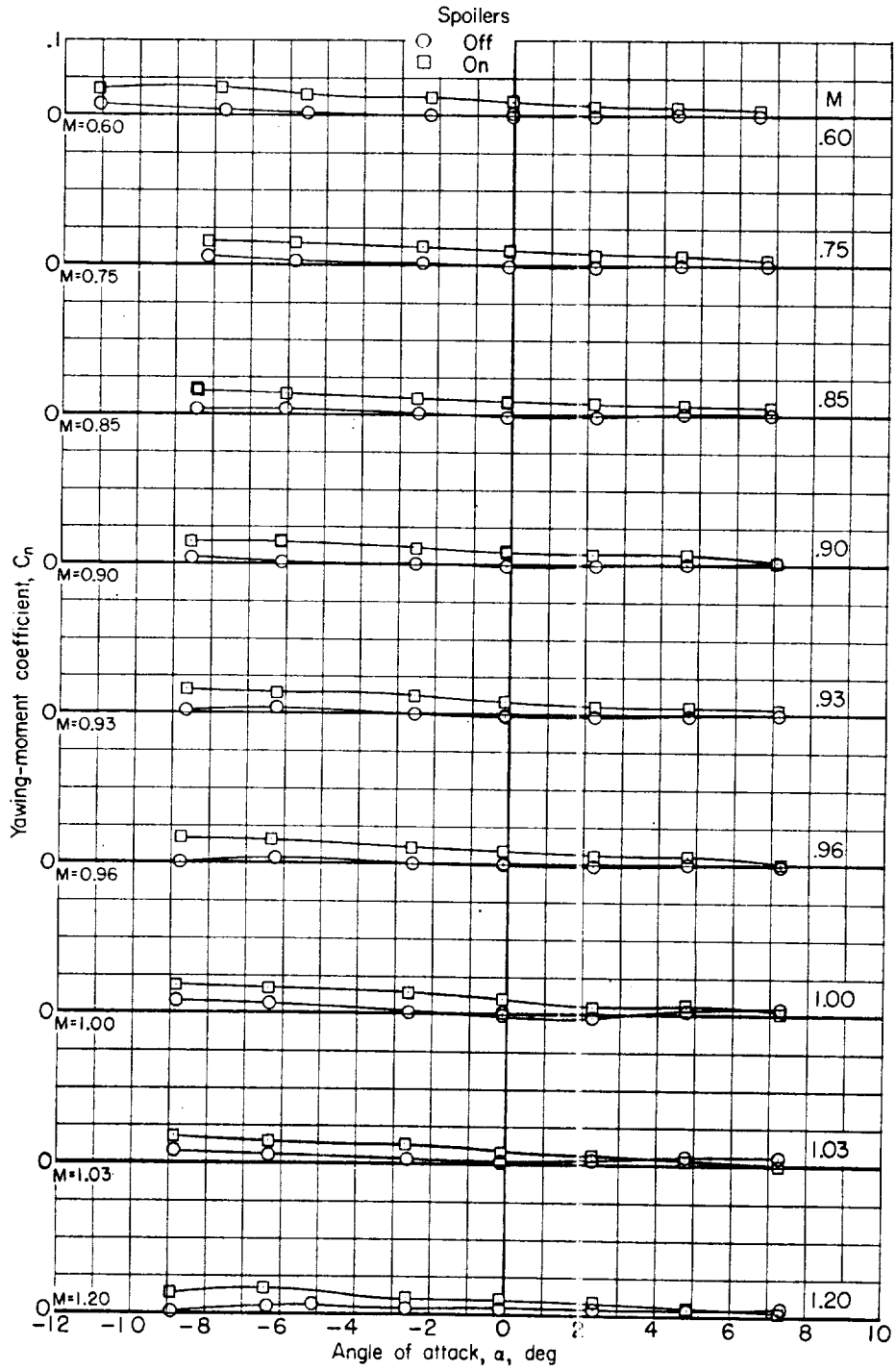

(b) Yawing-moment coefficient.

Figure 9.- Continued.

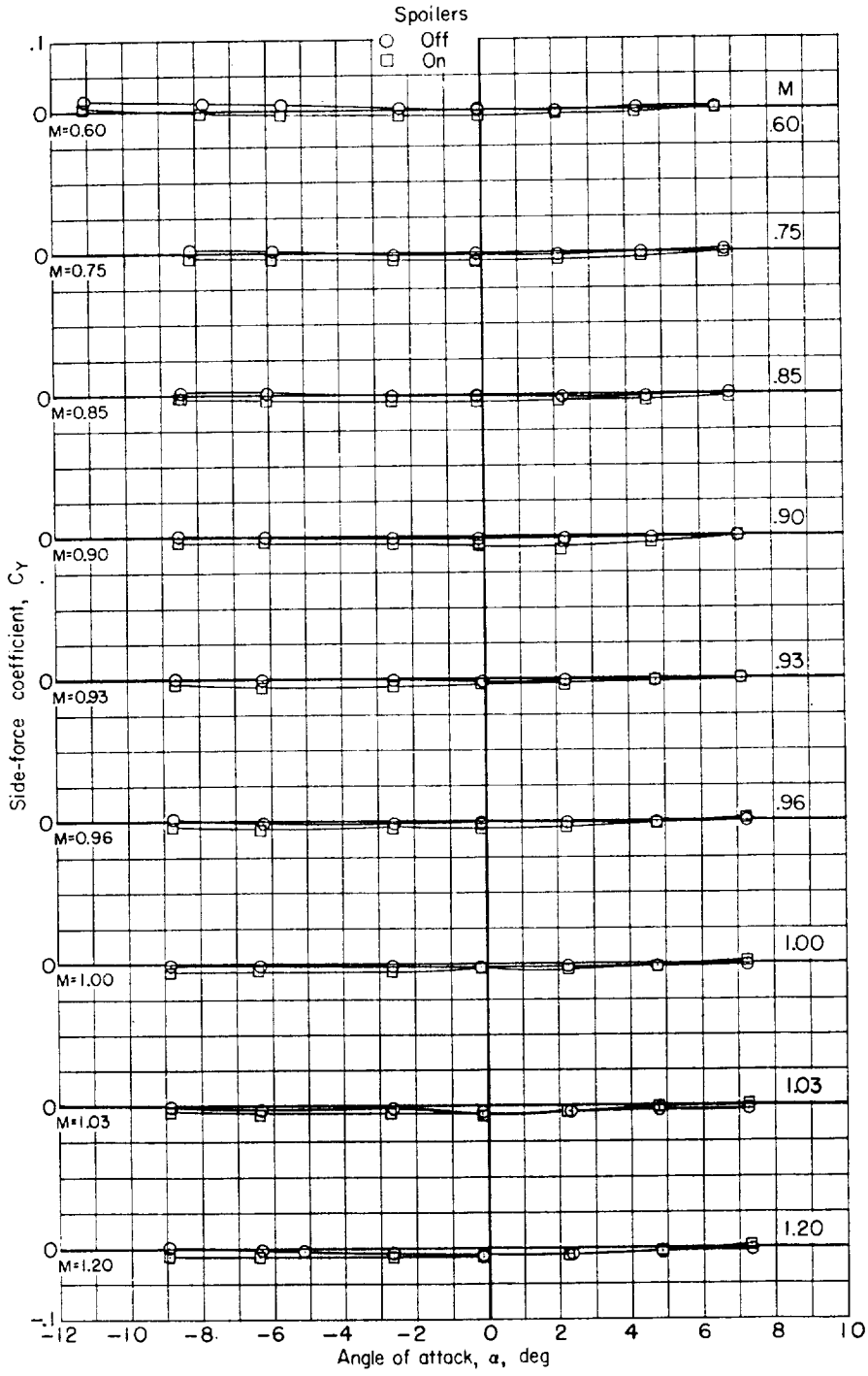

(c) Side-force coefficient.

Figure 9.- Concluded.

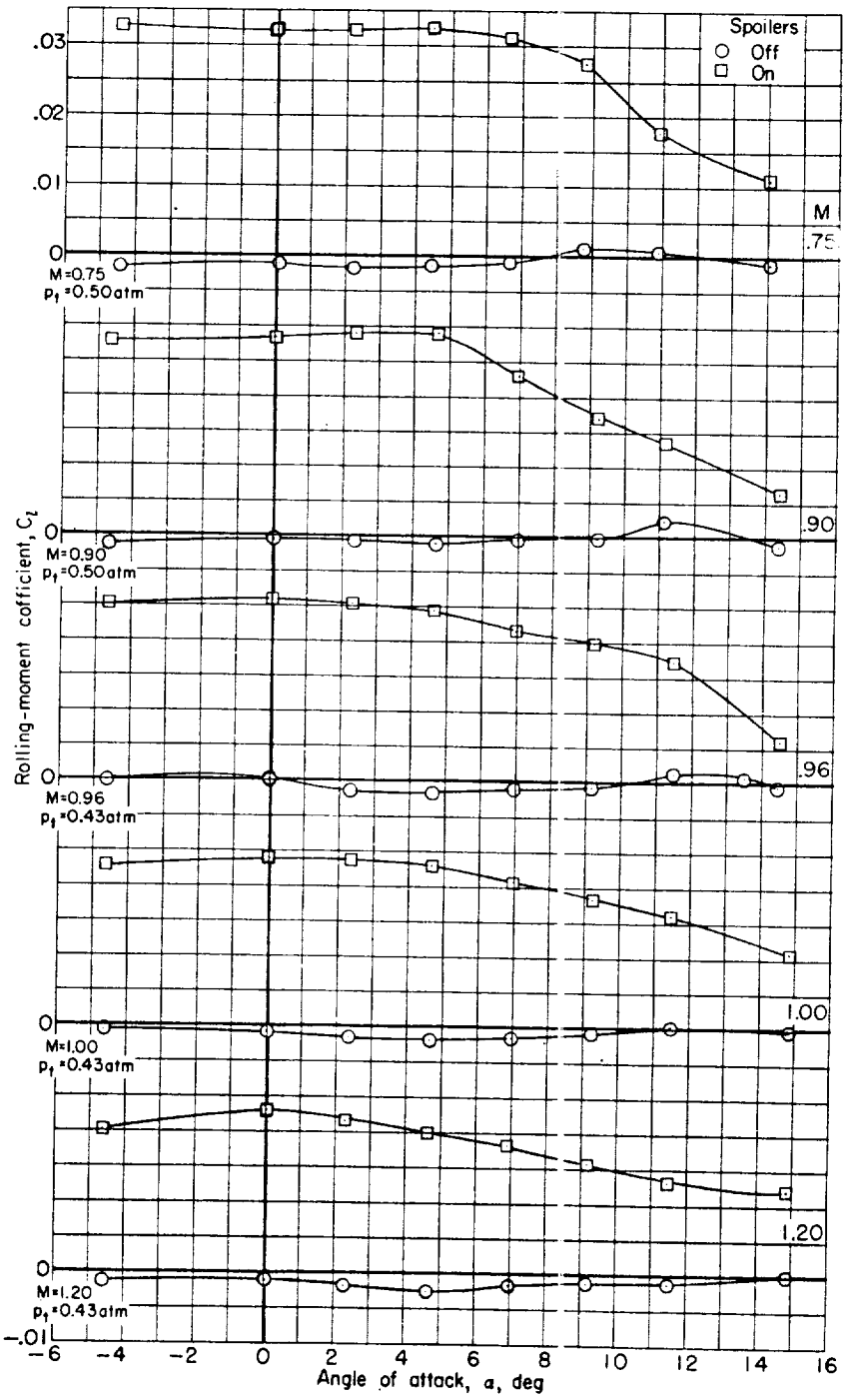

(a) Rolling-moment coefficient.

Figure 10.- Effect of spoilers on the aerodynamic characteristics for model without boosters. $\beta = 0^{\circ}$.

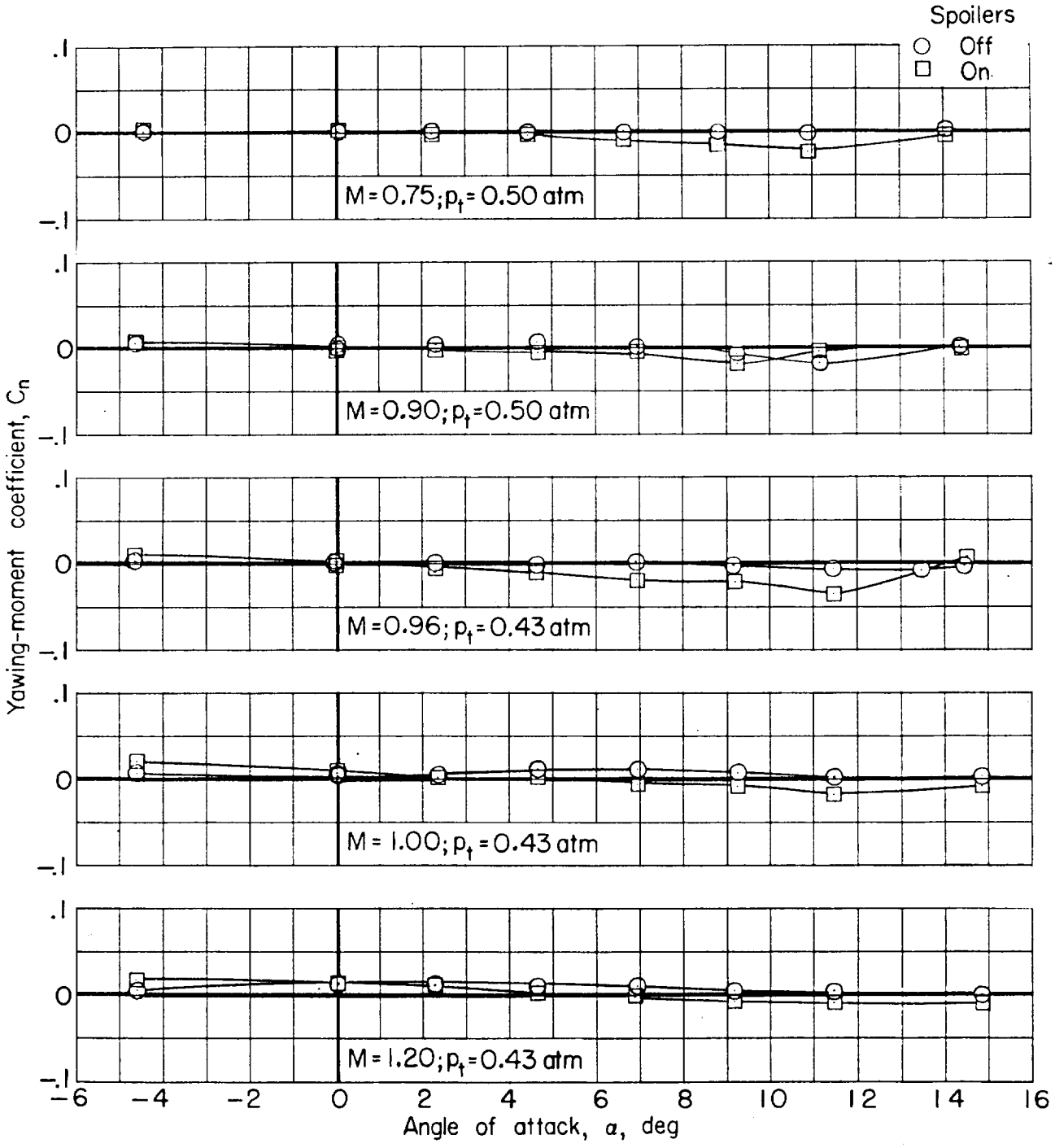

(b) Yawing-moment coefficient.

Figure 10.- Continued.

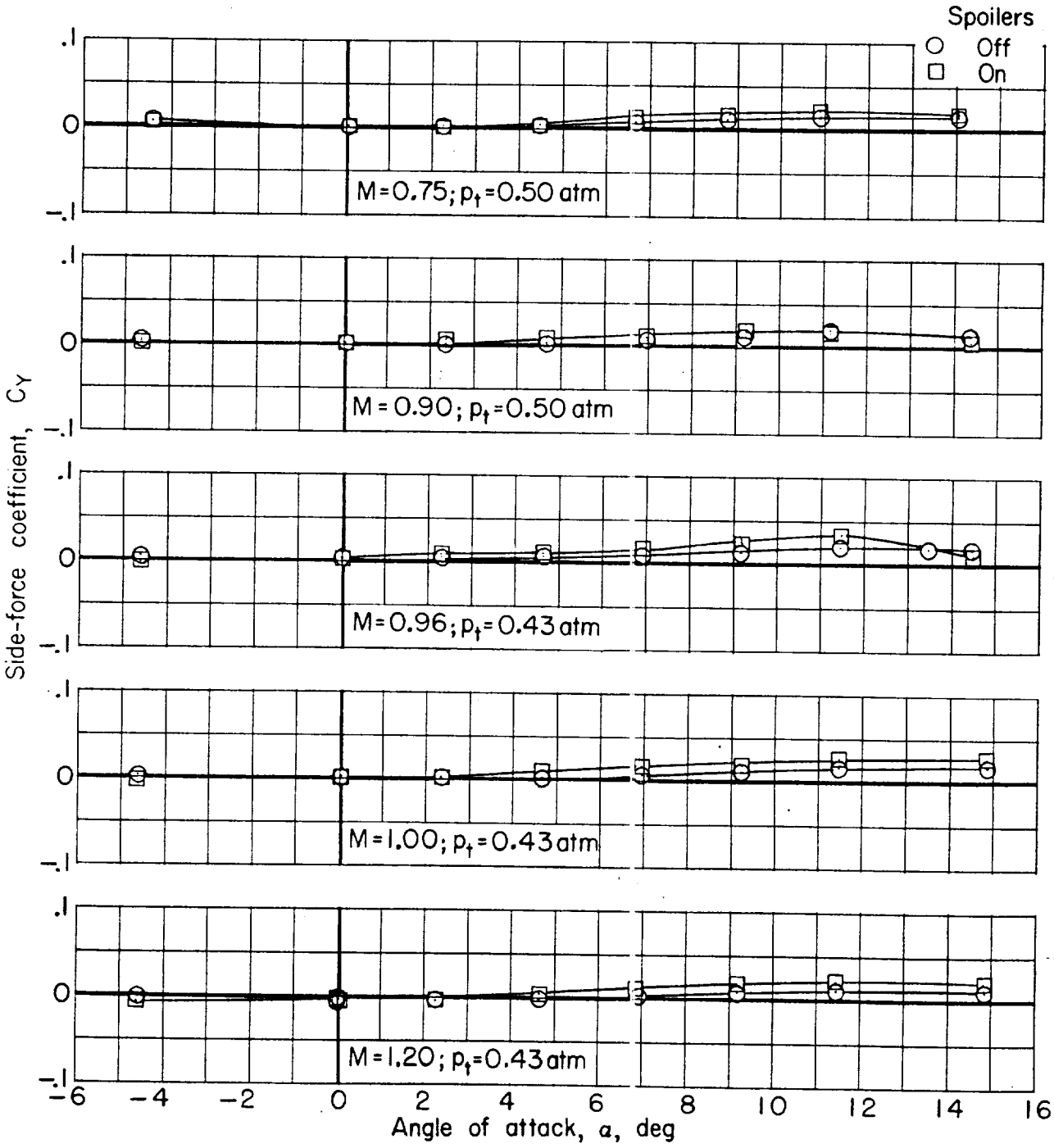

(c) Side-force coefficient.

Figure 10.- Concluded.

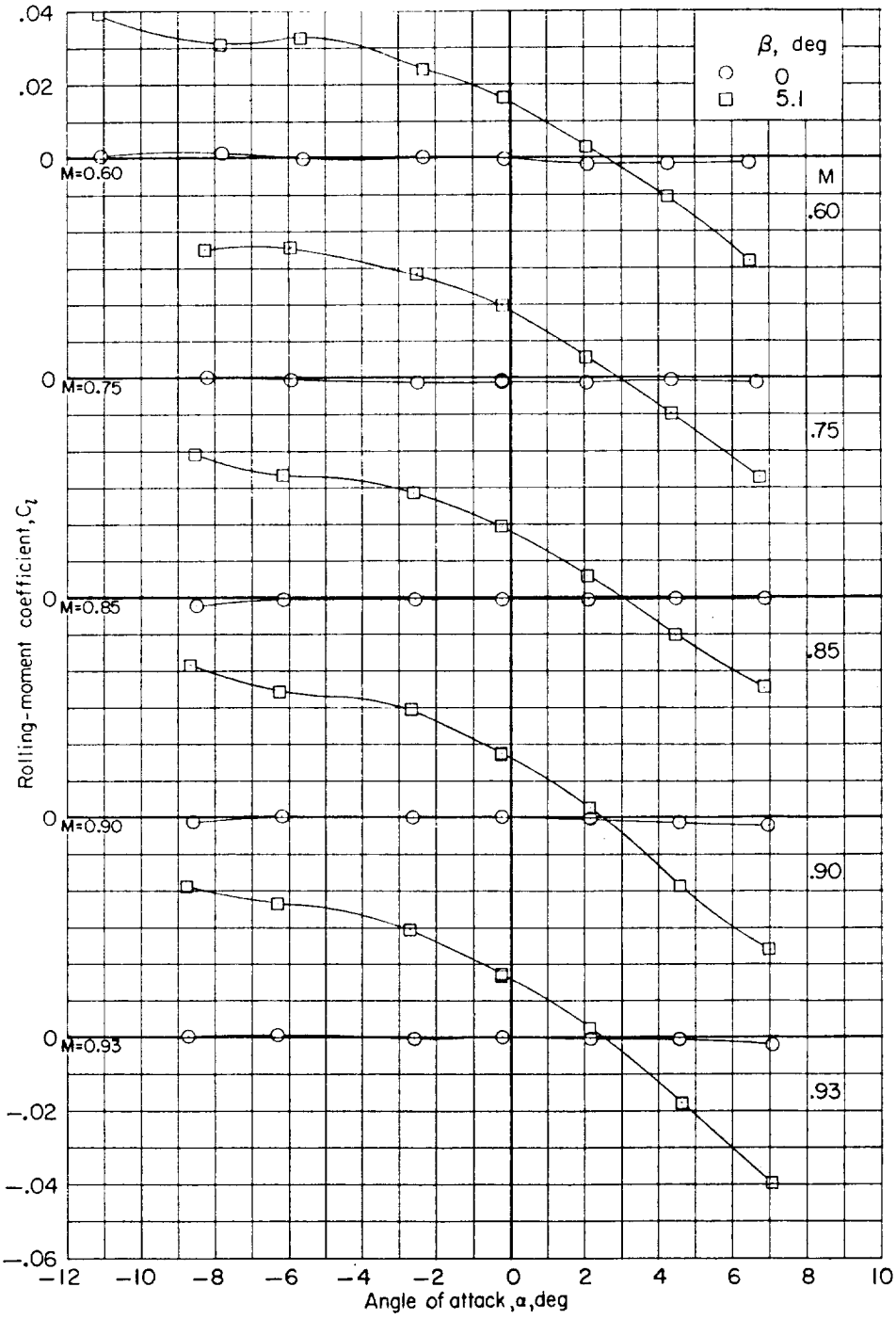

(a) Rolling-moment coefficient.

Figure 11.- Effect of sideslip angle on the aerodynamic characteristics for model with boosters. $\delta_c = -5^\circ$; spoilers off; $p_t = 0.50$ atm.

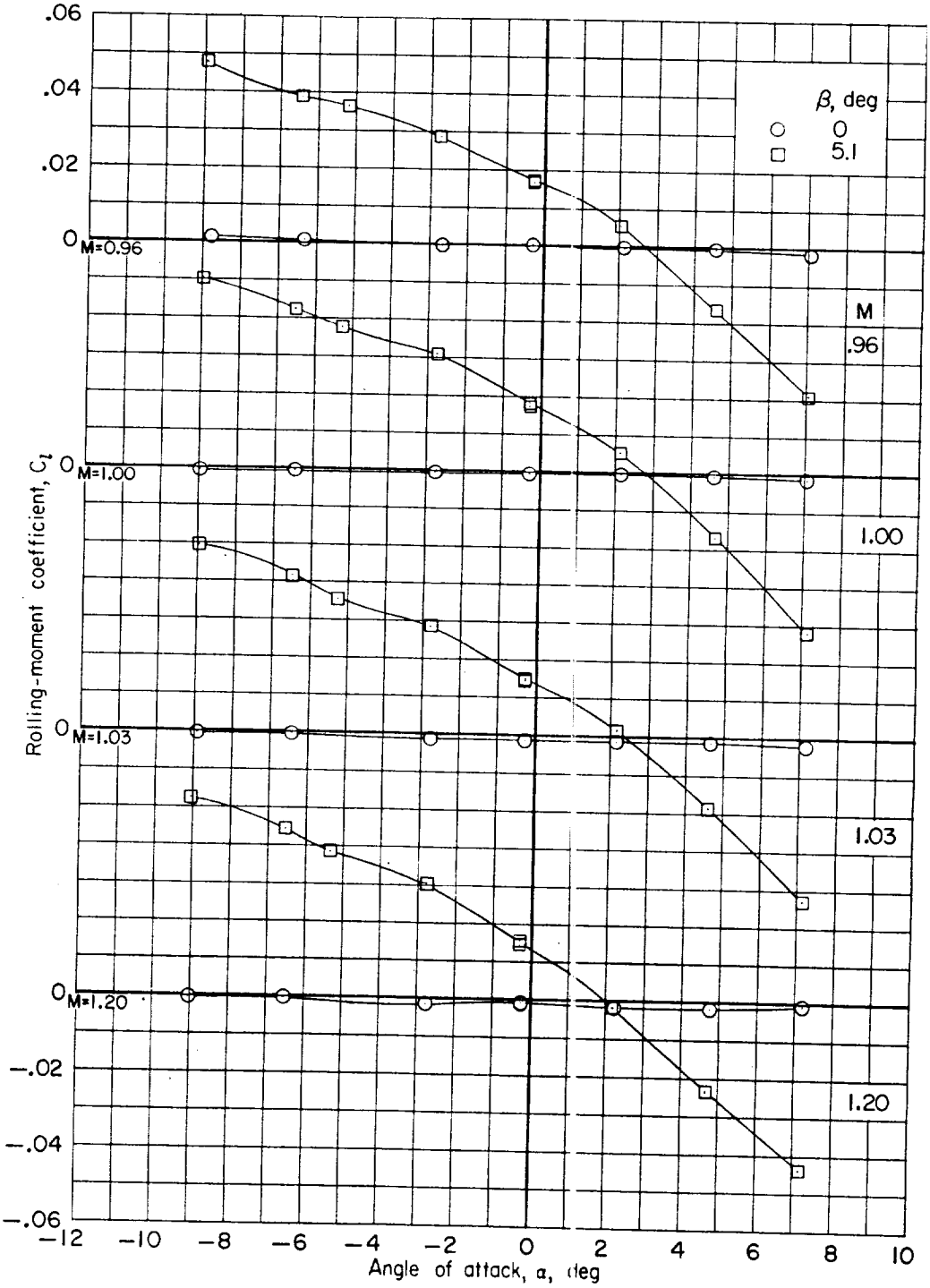

(a) Rolling-moment coefficient. Concluded.

Figure 11.- Continued.

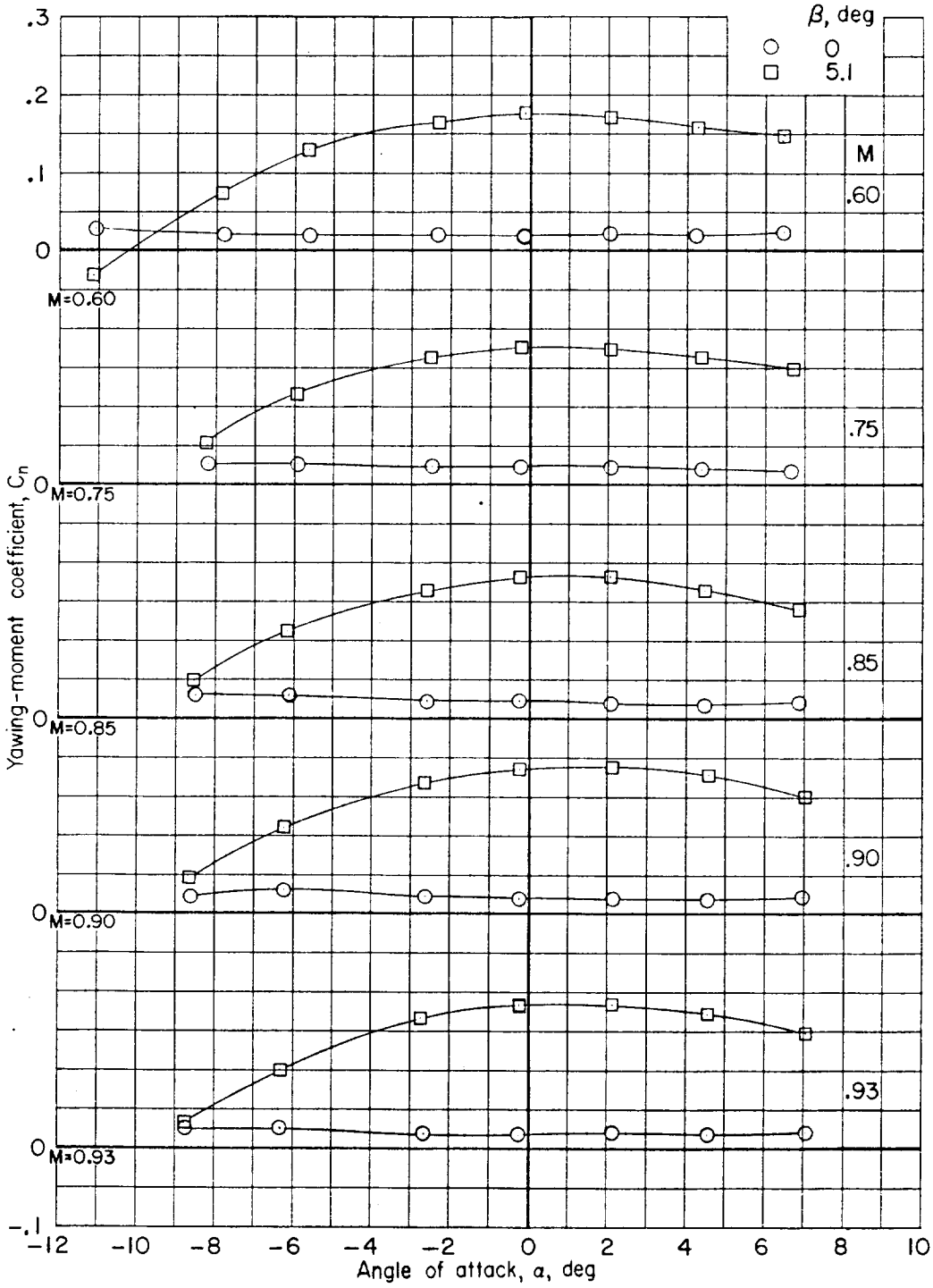

(b) Yawing-moment coefficient.

Figure 11.- Continued.

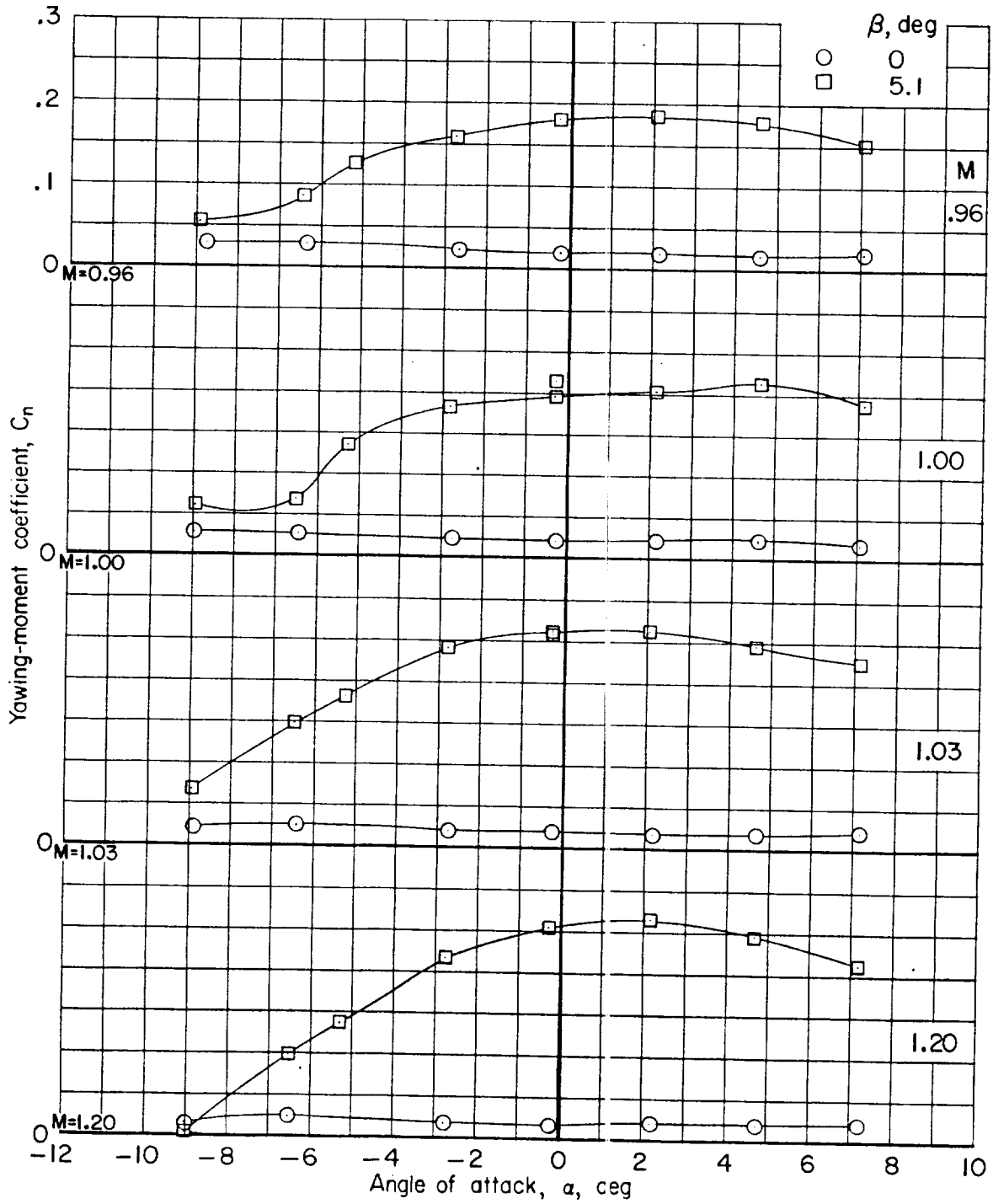

(b) Yawing-moment coefficient. Concluded.

Figure 11.- Continued.

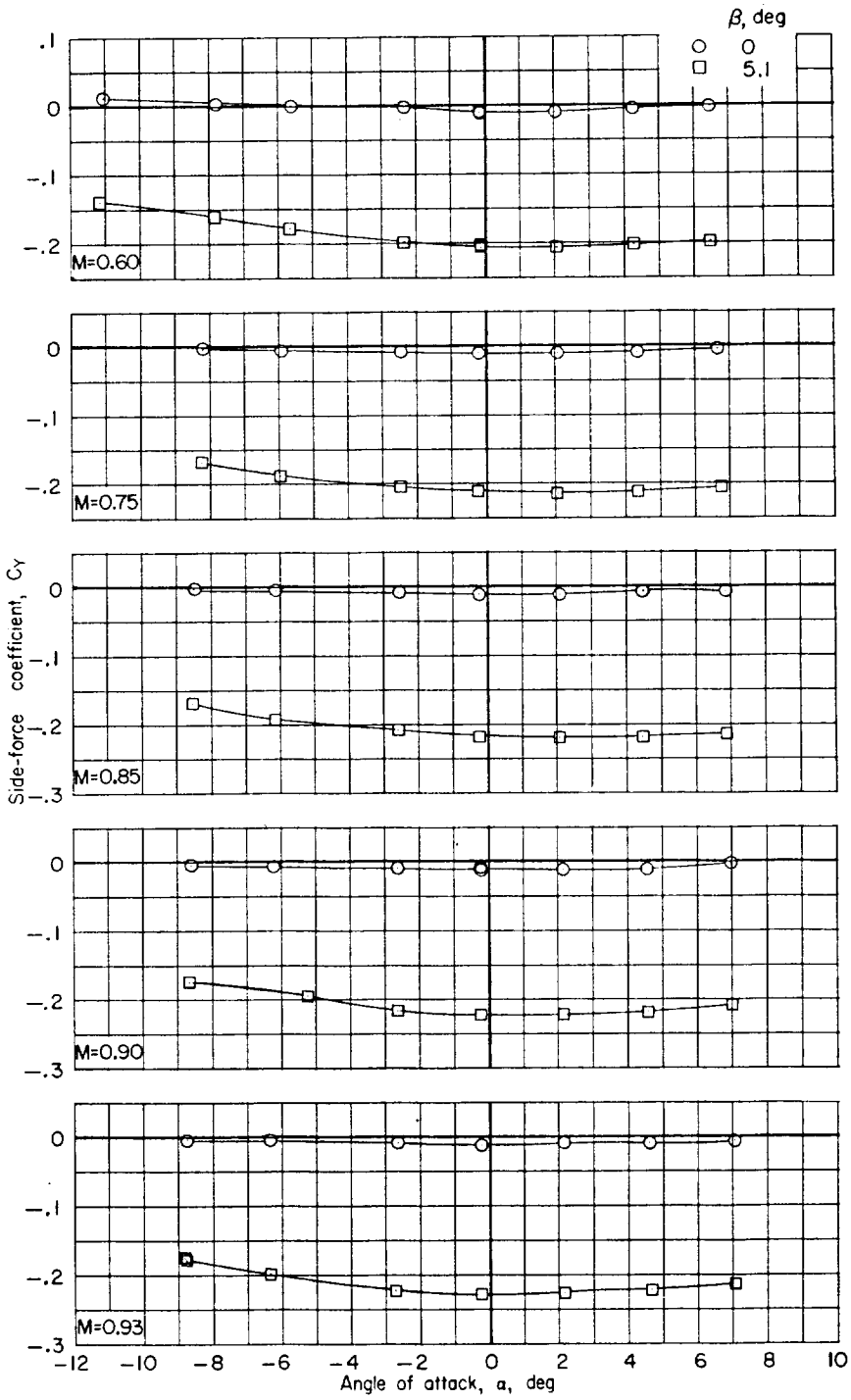

(c) Side-force coefficient.

Figure 11.- Continued.

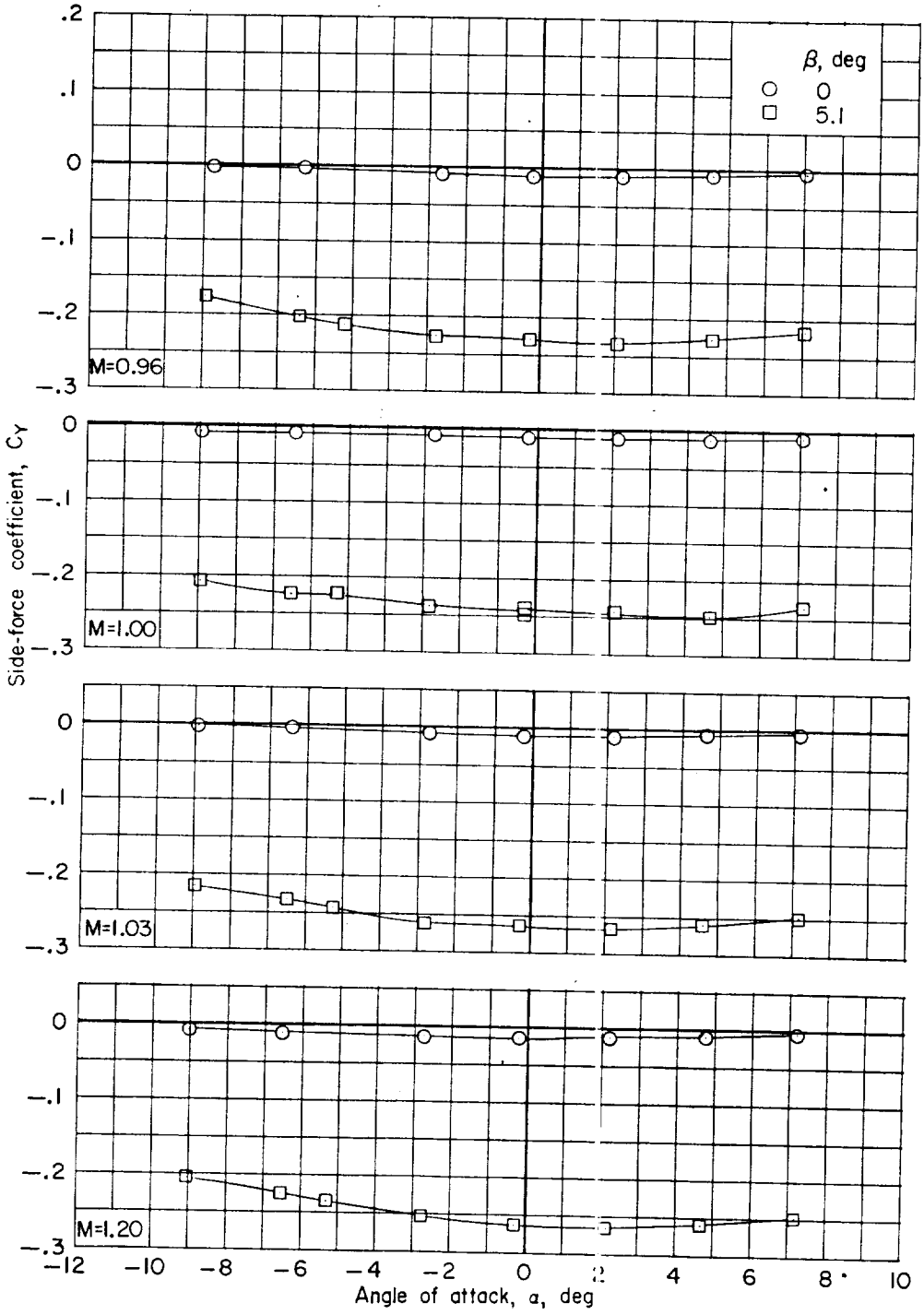

(c) Side-force coefficient. Concluded.

Figure 11.- Concluded.

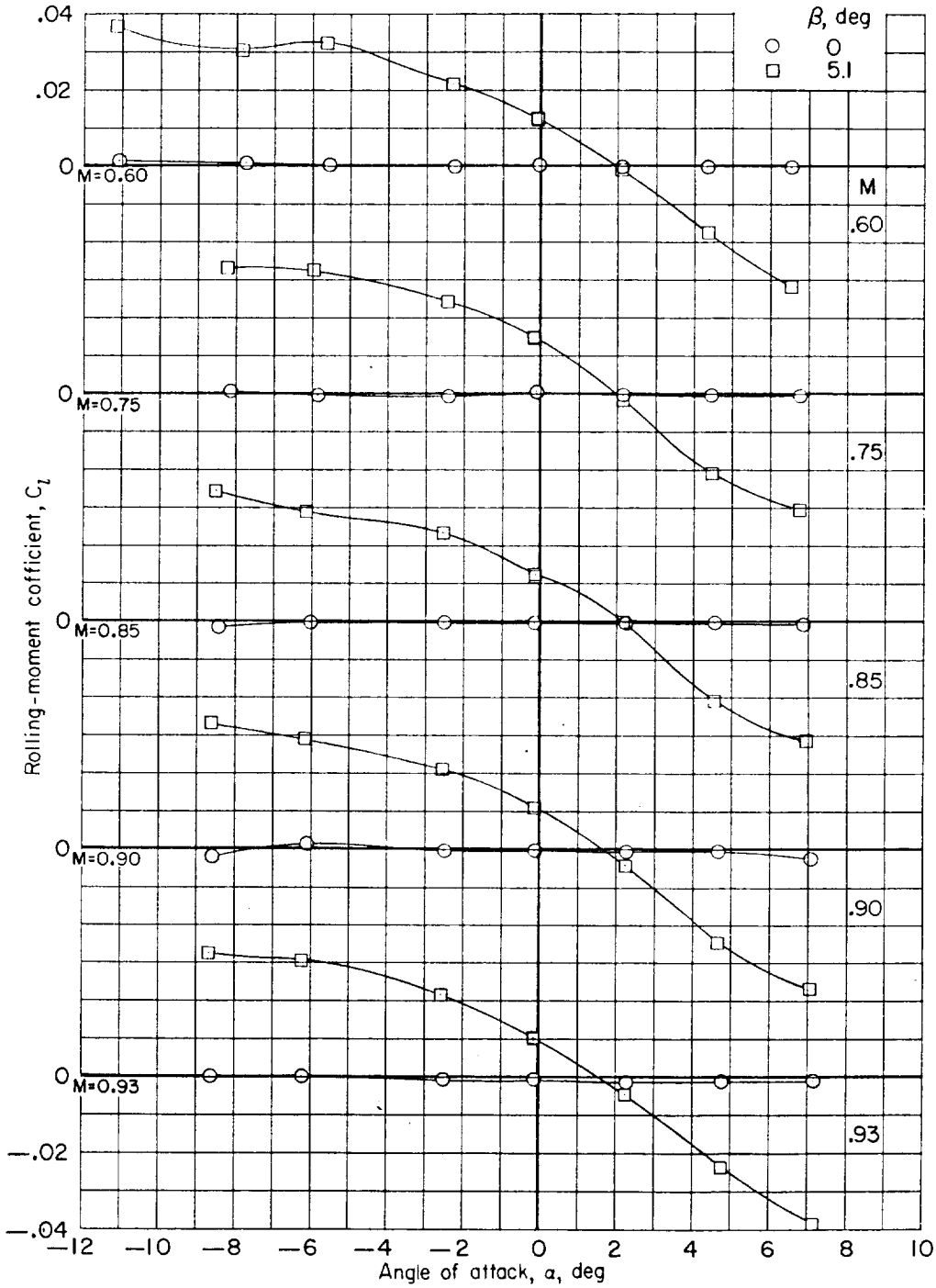

(a) Rolling-moment coefficient.

Figure 12.- Effect of sideslip angle on the aerodynamic characteristics for model with boosters. $\delta_c = 0°$; spoilers off; $p_t = 0.50$ atm.

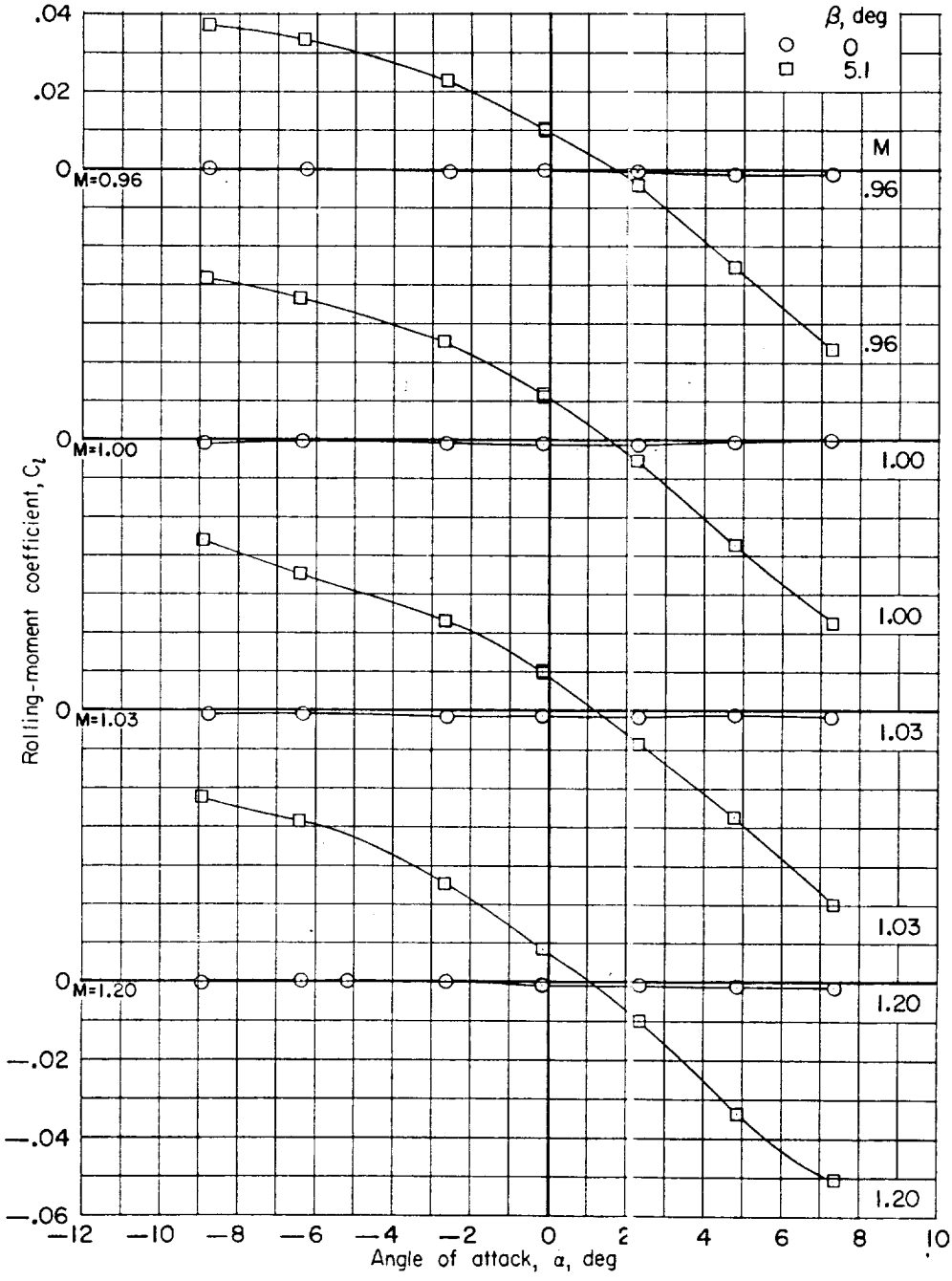

(a) Rolling-moment coefficient. Concluded.

Figure 12.- Continued.

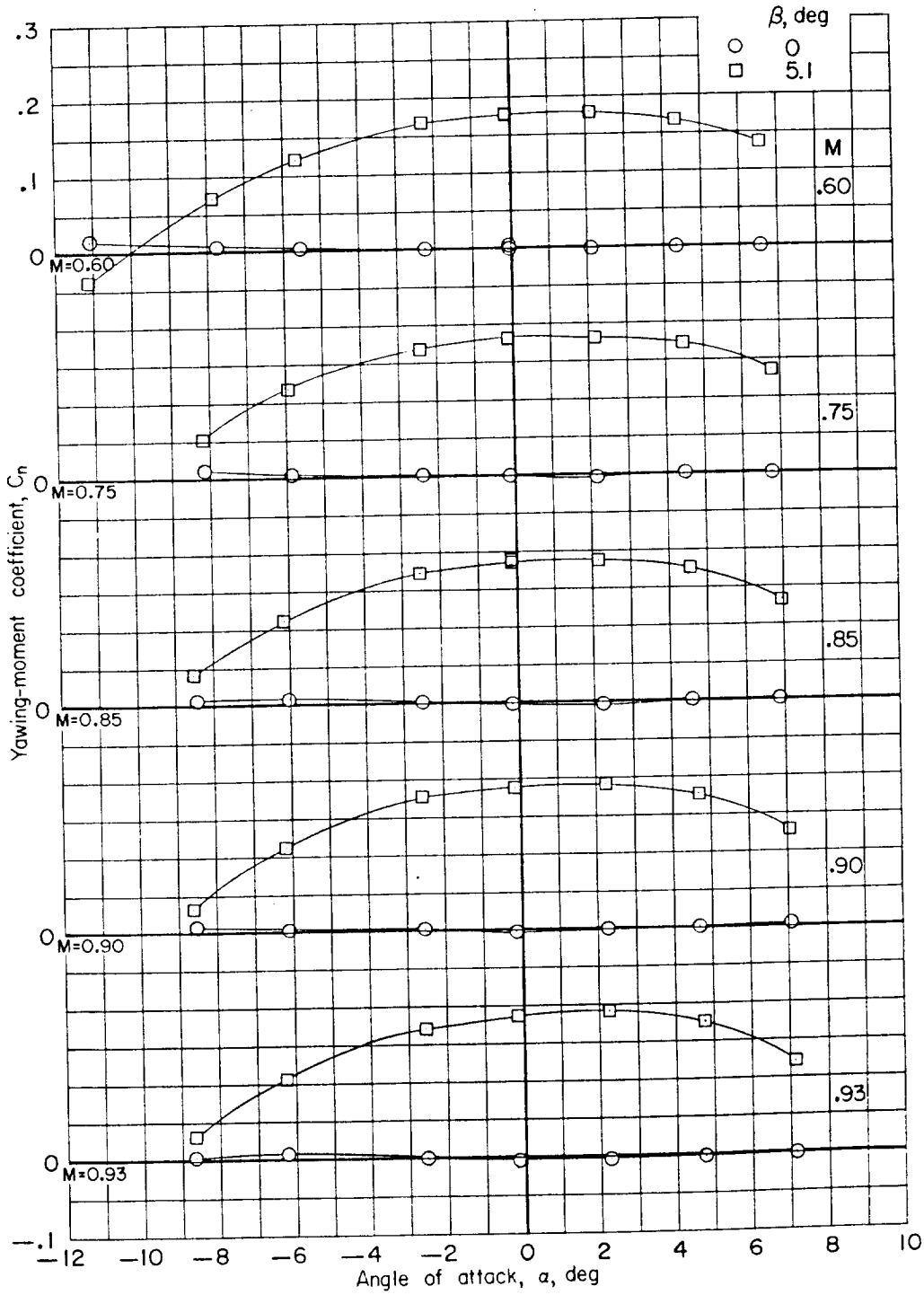

(b) Yawing-moment coefficient.

Figure 12.- Continued.

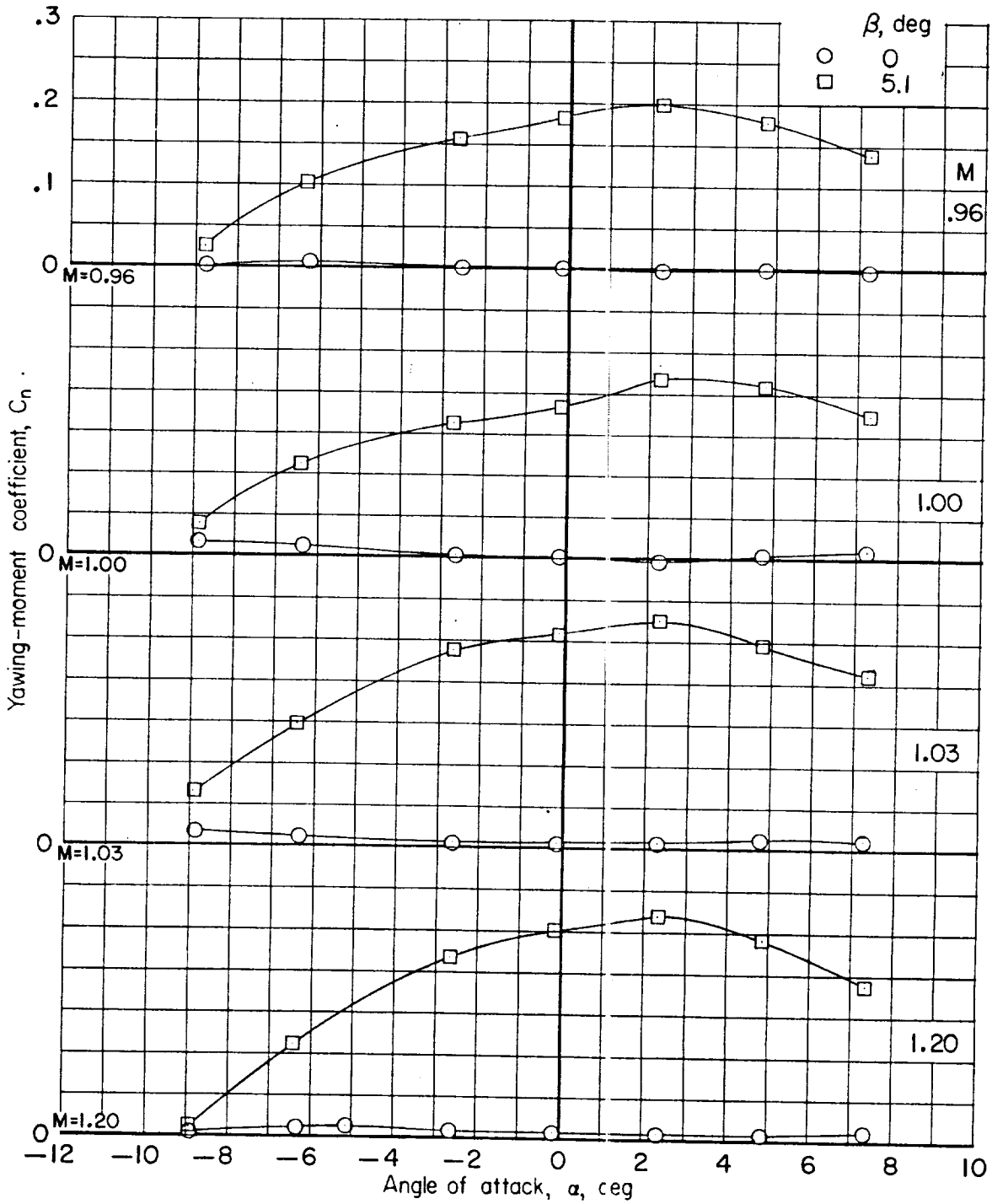

(b) Yawing-moment coefficient. Concluded.

Figure 12.- Continued.

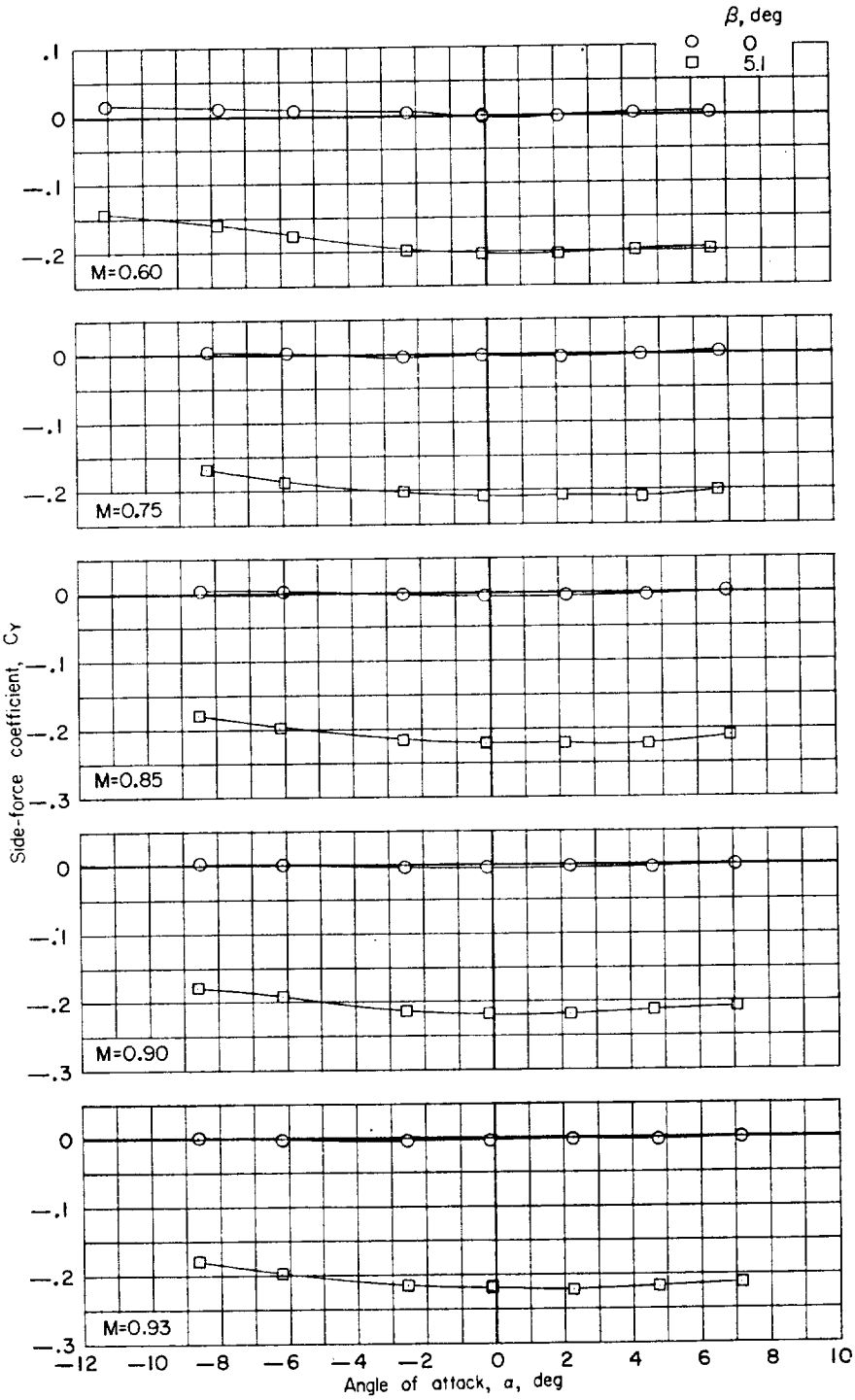

(c) Side-force coefficient.

Figure 12.- Continued.

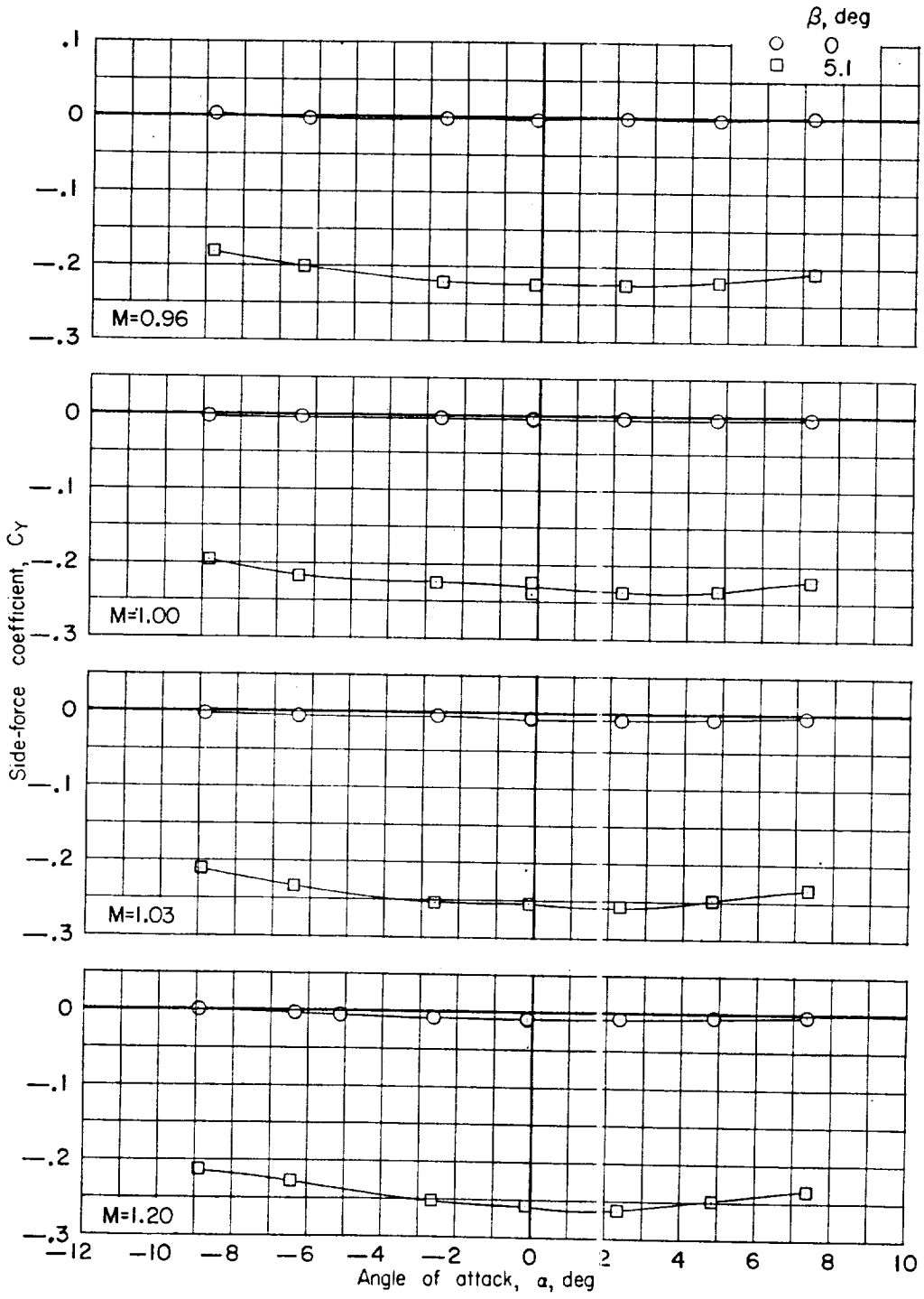

(c) Side-force coefficient. Concluded.

Figure 12.- Concluded.

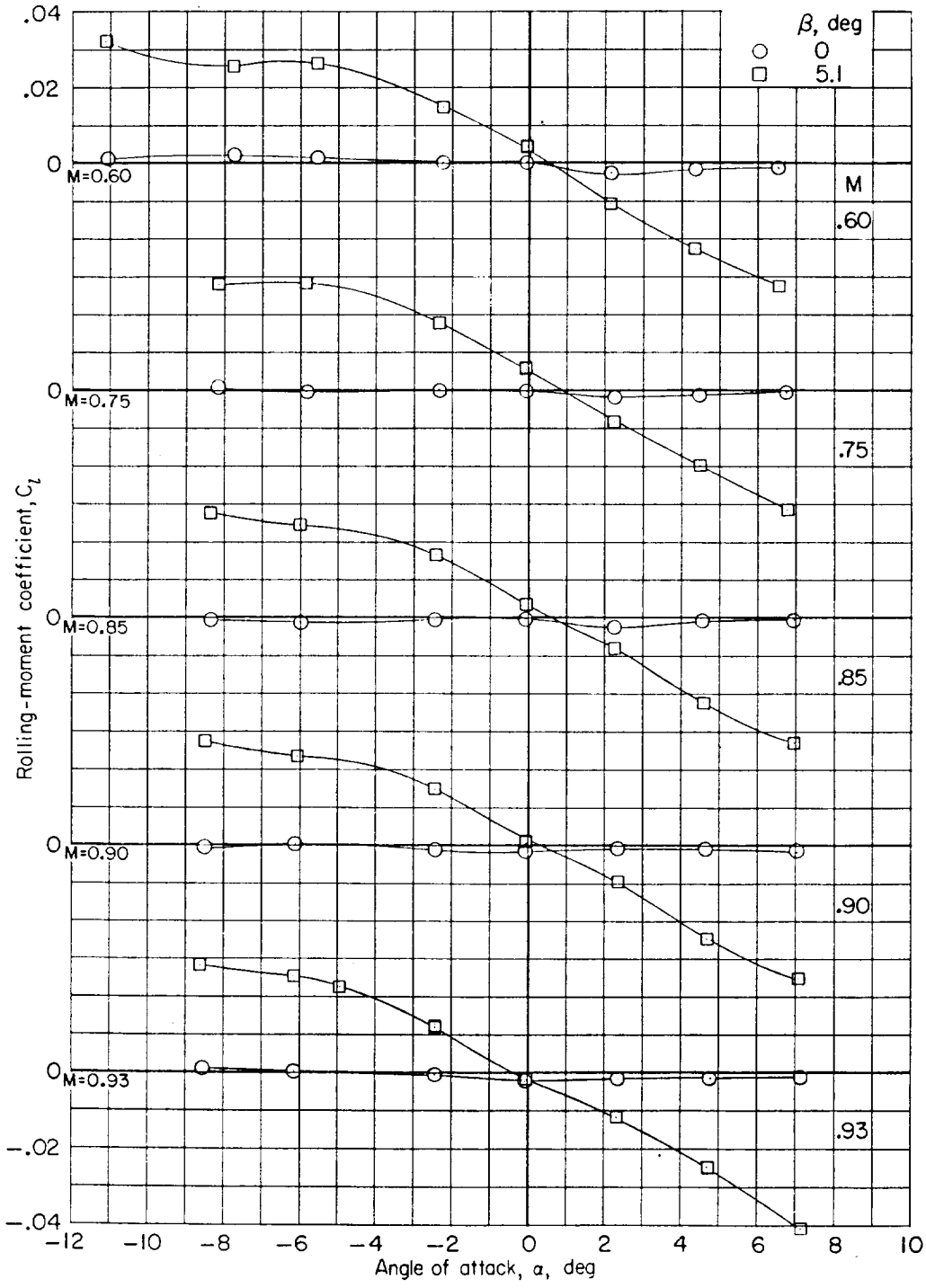

(a) Rolling-moment coefficient.

Figure 13.- Effect of sideslip angle on the aerodynamic characteristics for model with boosters. $\delta_c = 5^\circ$; spoilers off; $p_t = 0.50$ atm.

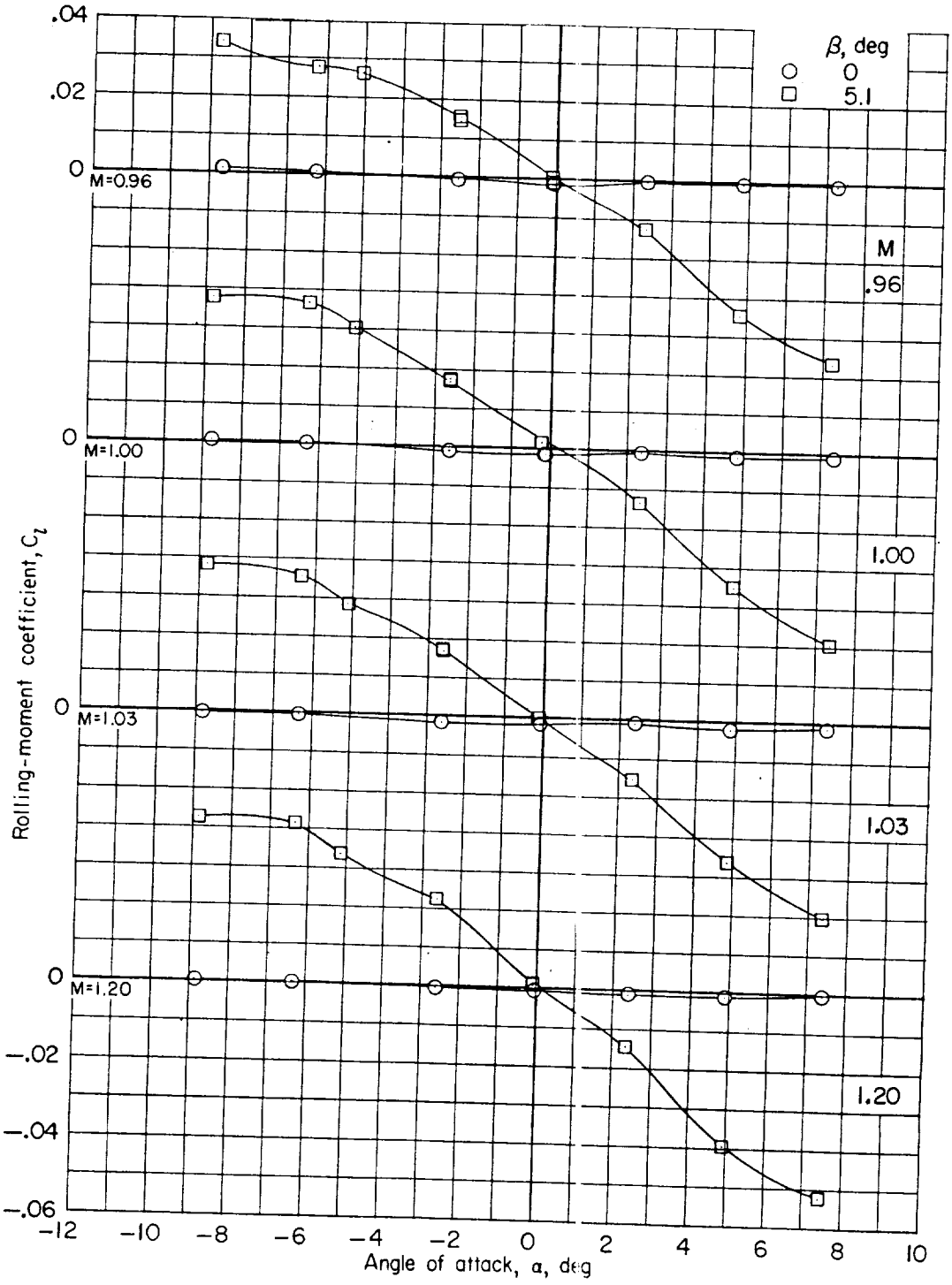

(a) Rolling-moment coefficient. Concluded.

Figure 13.- Continued.

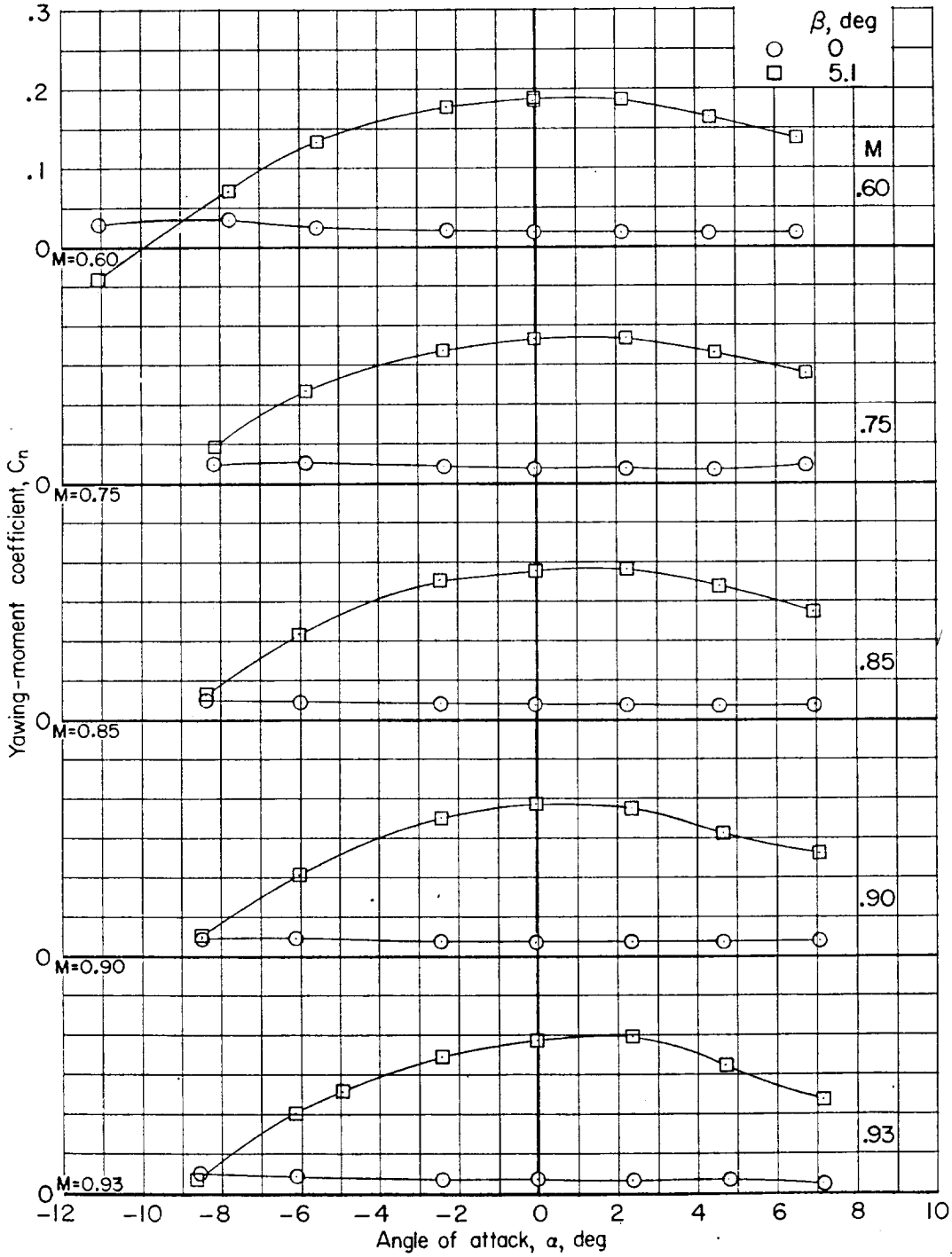

(b) Yawing-moment coefficient.

Figure 13.- Continued.

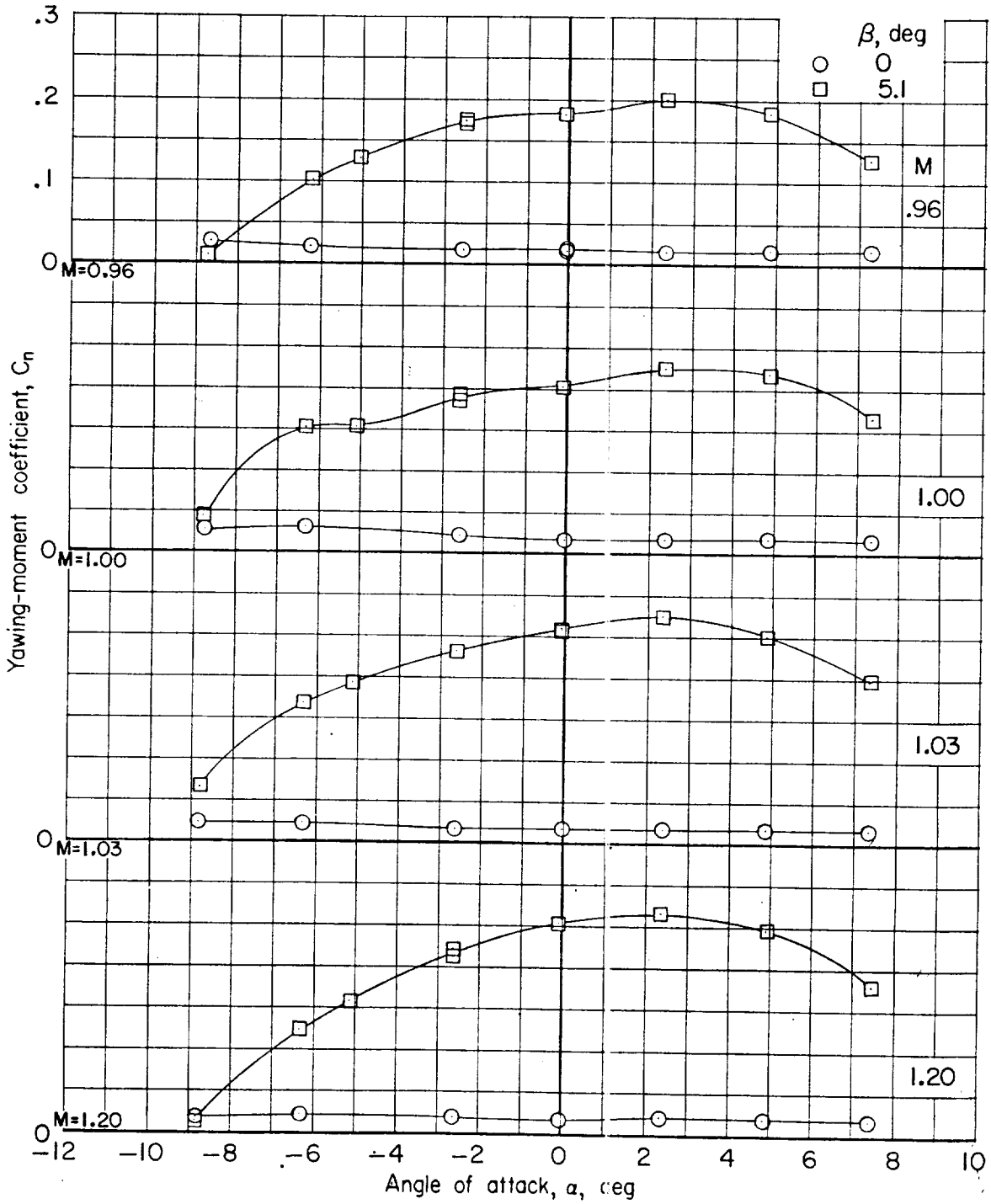

(b) Yawing-moment coefficient Concluded.

Figure 13.- Continued.

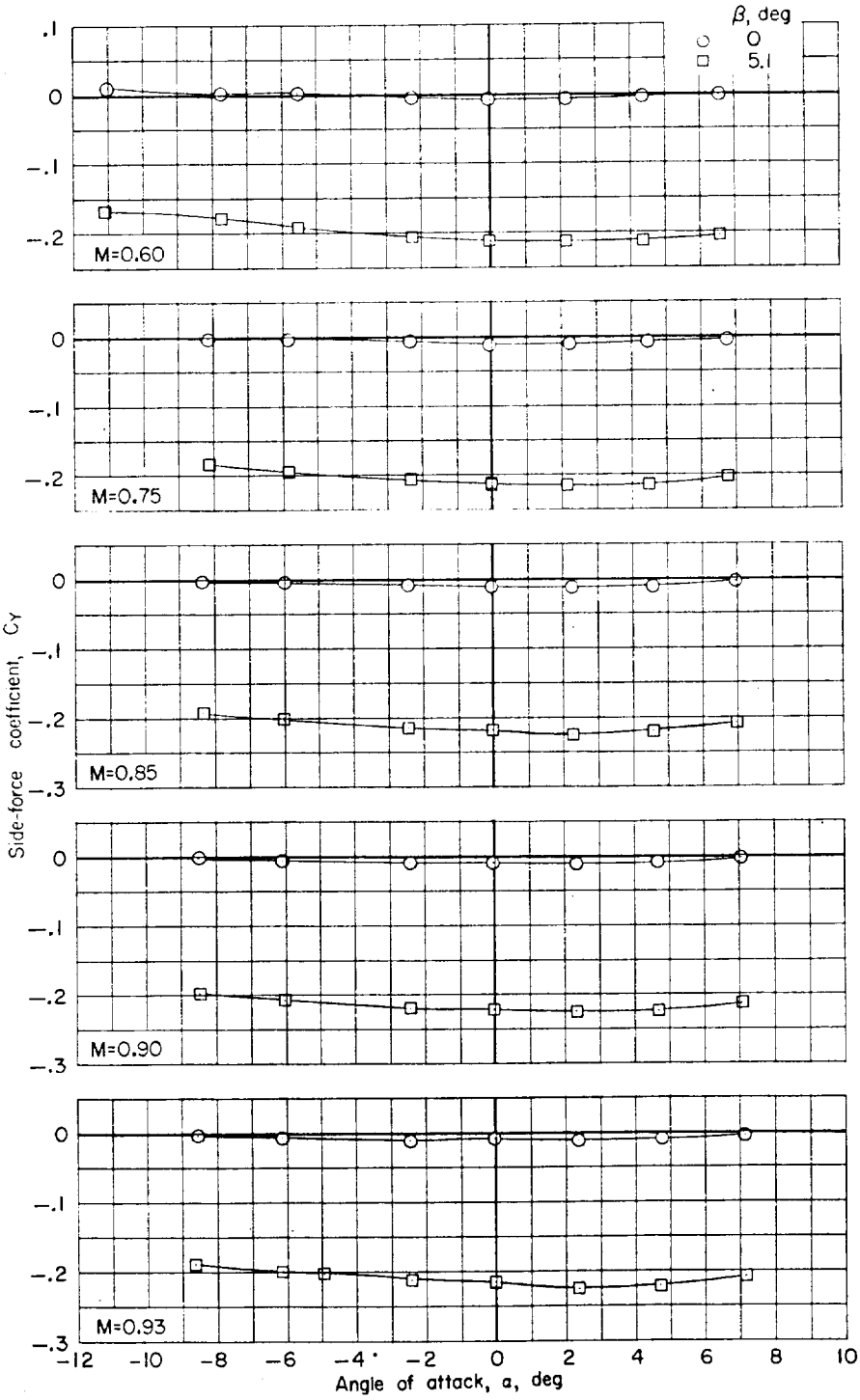

(c) Side-force coefficient.

Figure 13.- Continued.

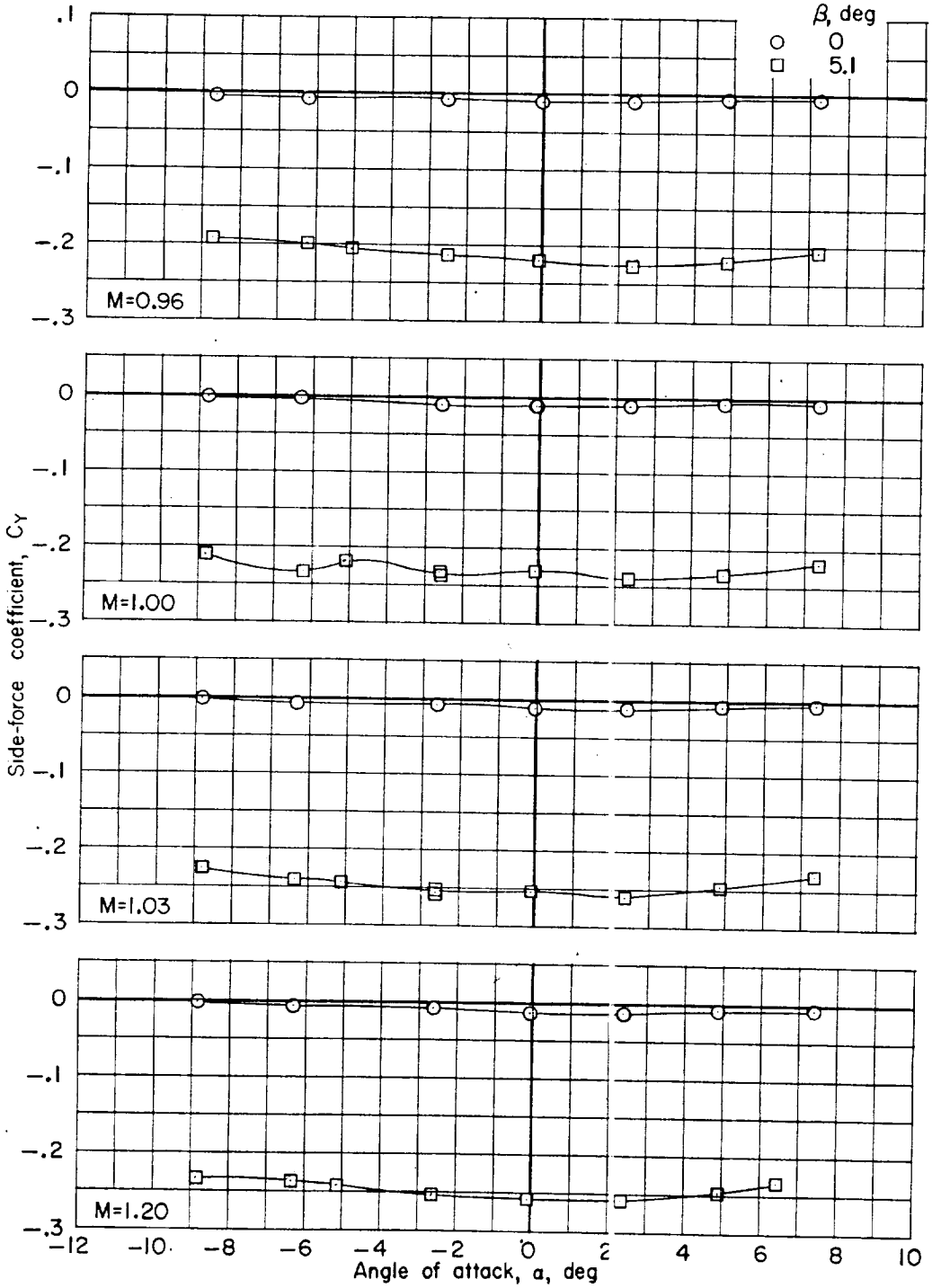

(c) Side-force coefficient. Concluded.

Figure 13.- Concluded.

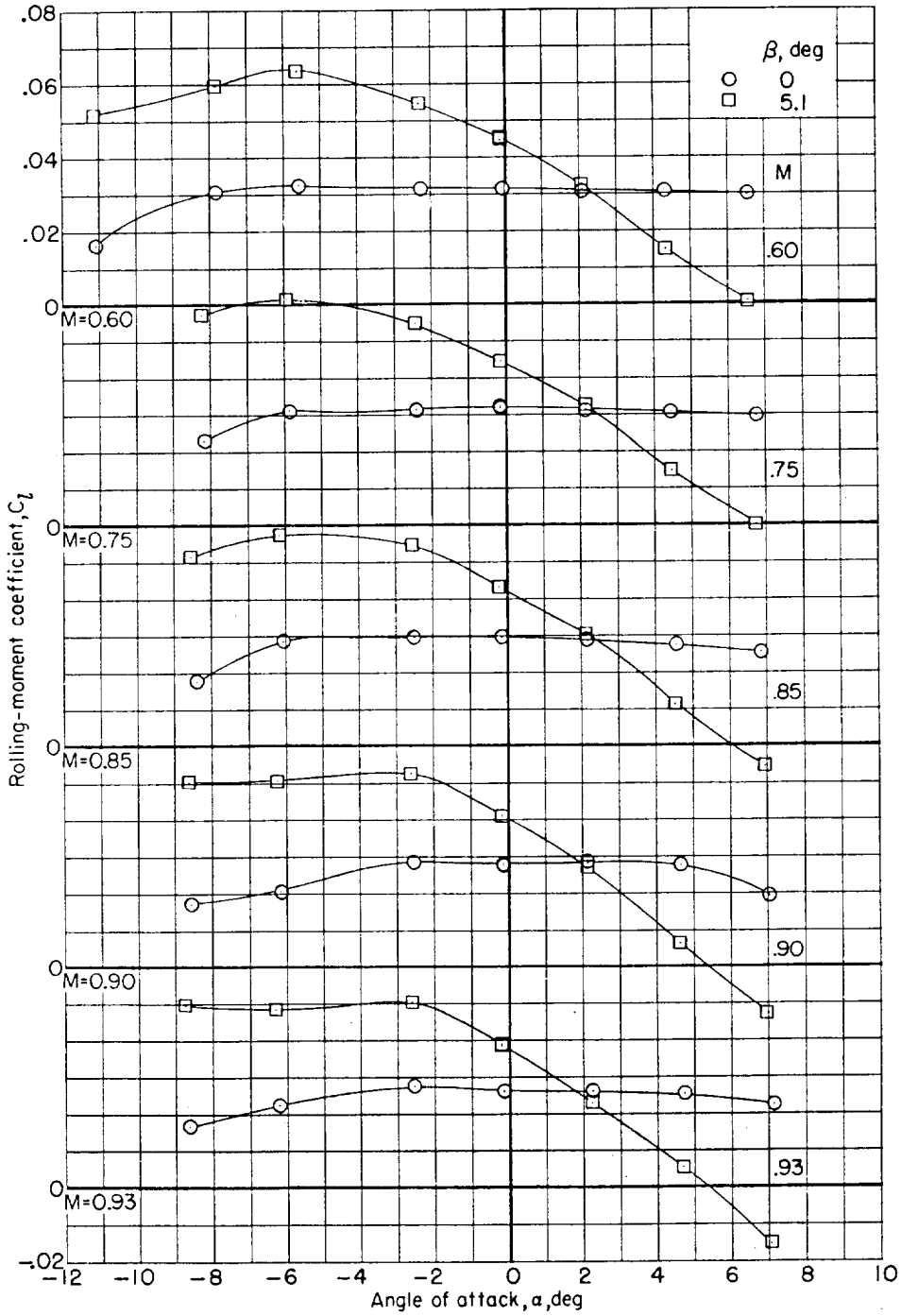

(a) Rolling-moment coefficient.

Figure 14.- Effect of sideslip angle on the aerodynamic characteristics for model with boosters. $\delta_c = 0^\circ$; spoilers on; $p_t = 0.50$ atm.

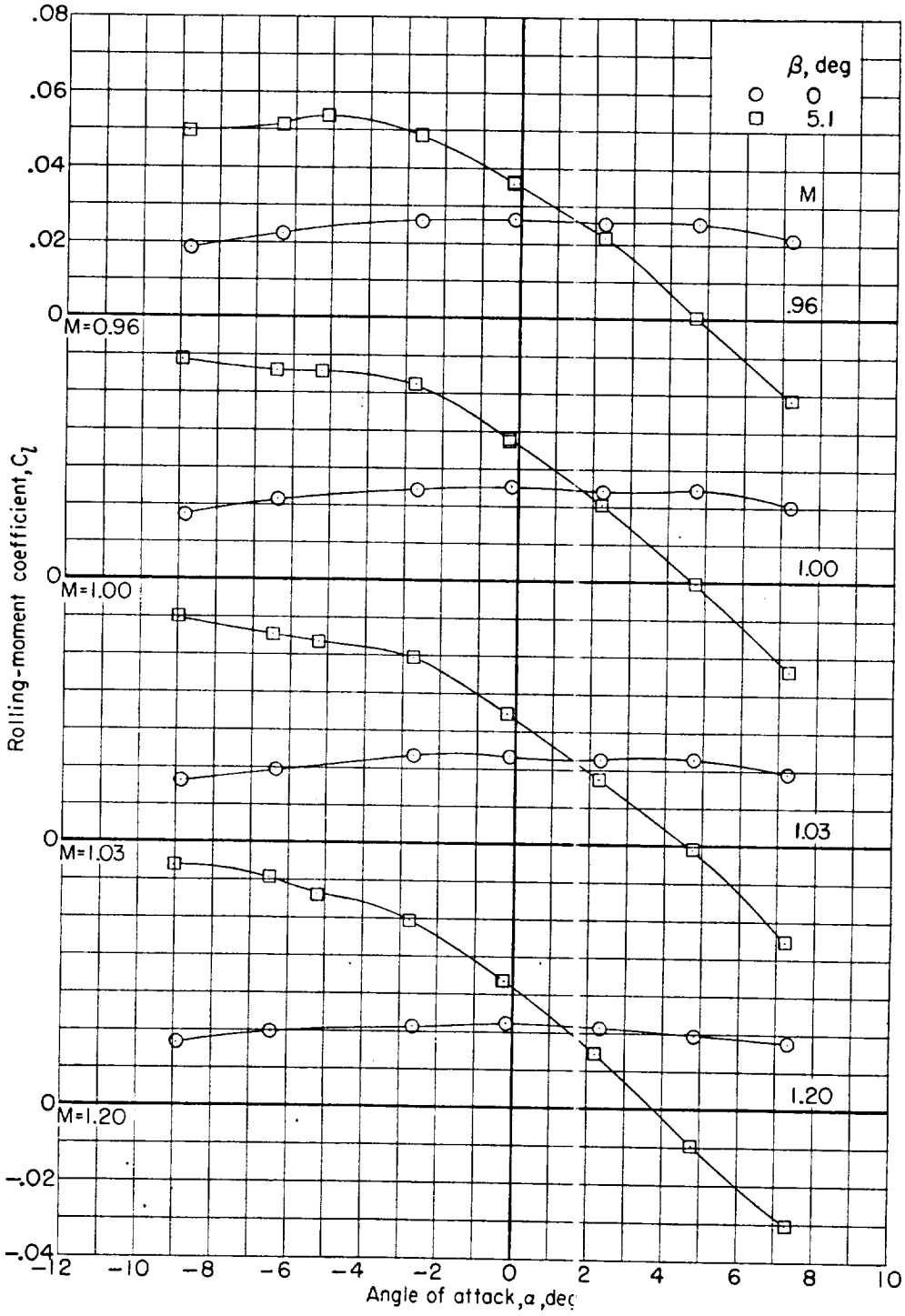

(a) Rolling-moment coefficient. Concluded.

Figure 14.- Continued.

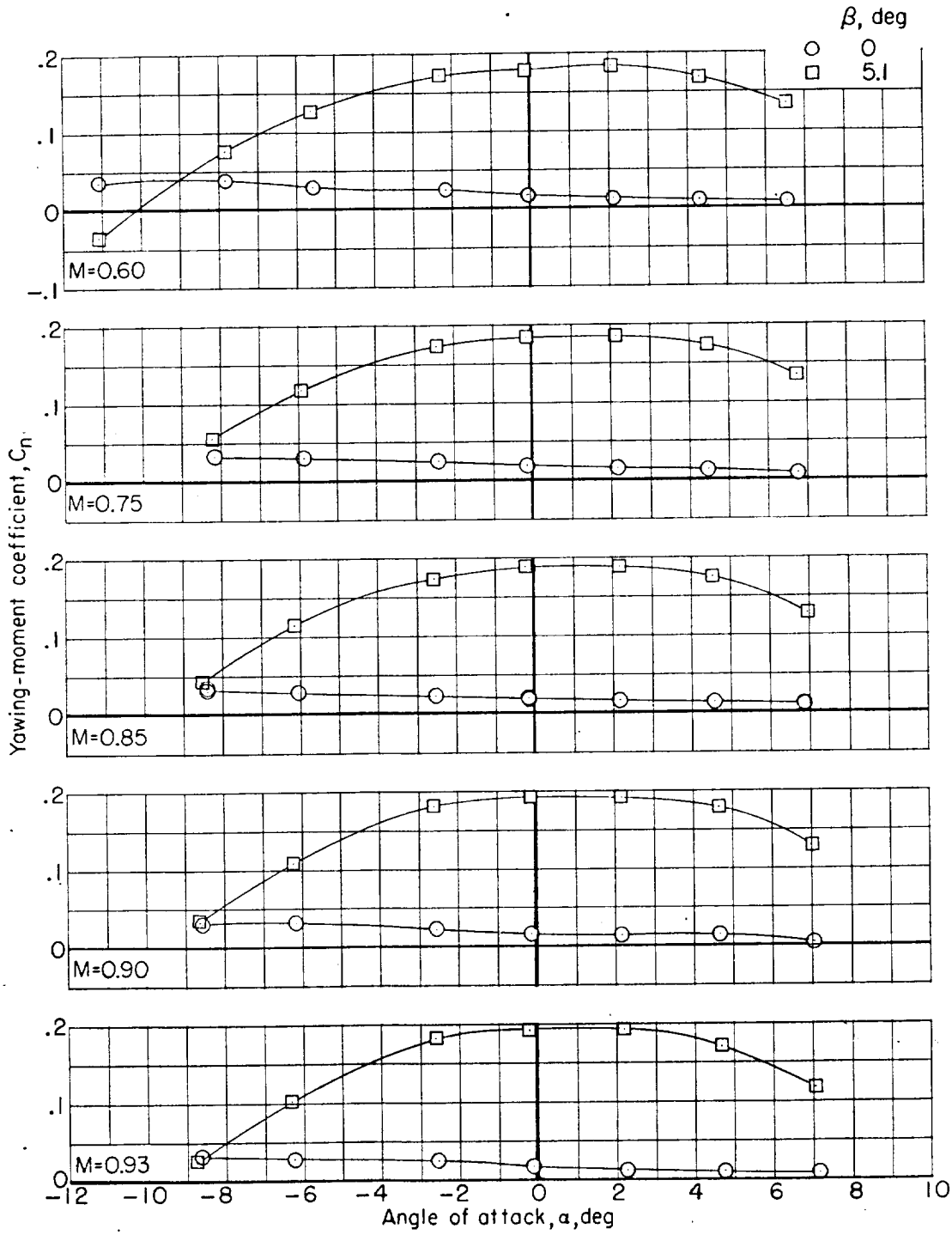

(b) Yawing-moment coefficient.

Figure 14.- Continued.

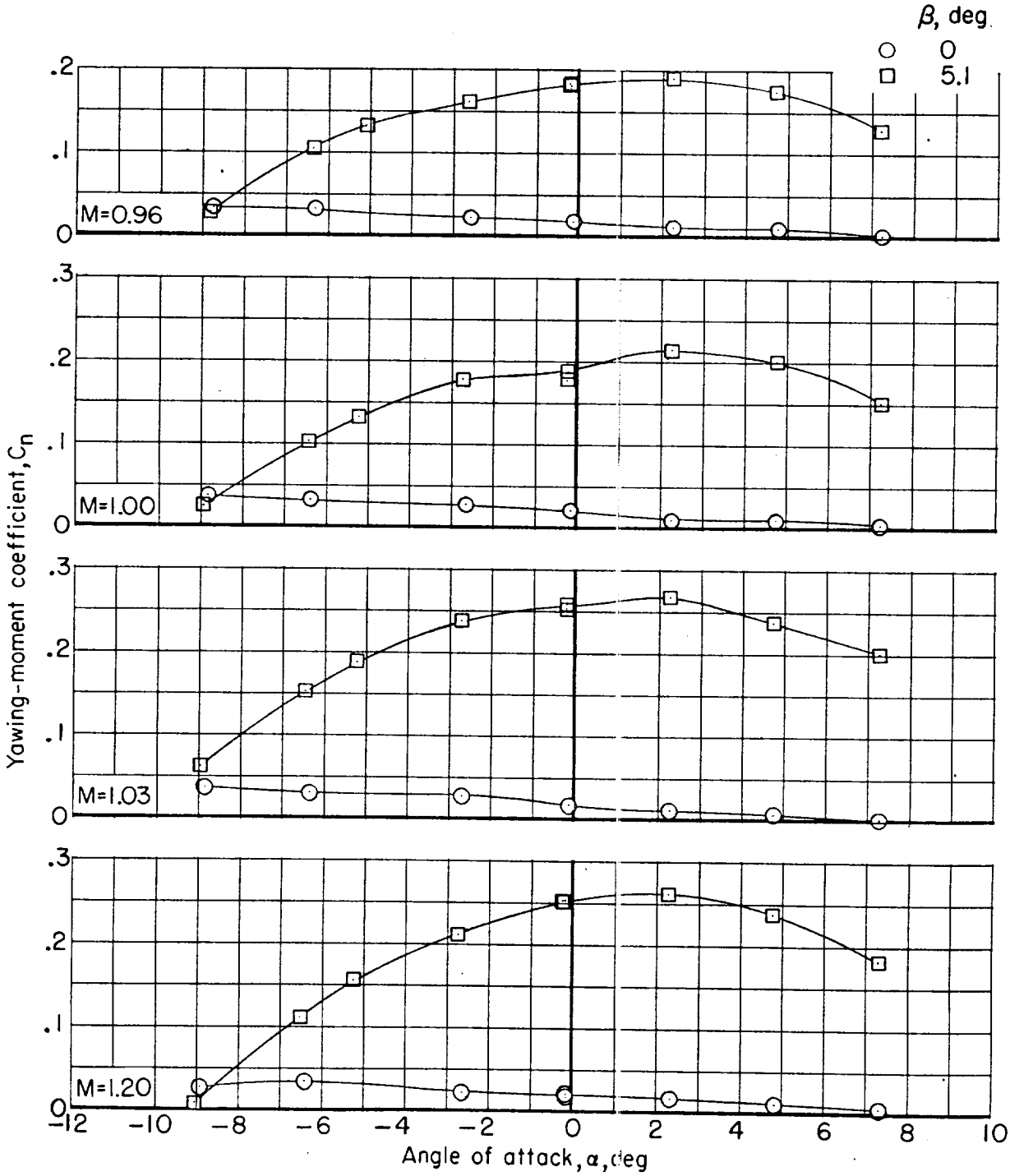

(b) Yawing-moment coefficient. Concluded.

Figure 14.- Continued.

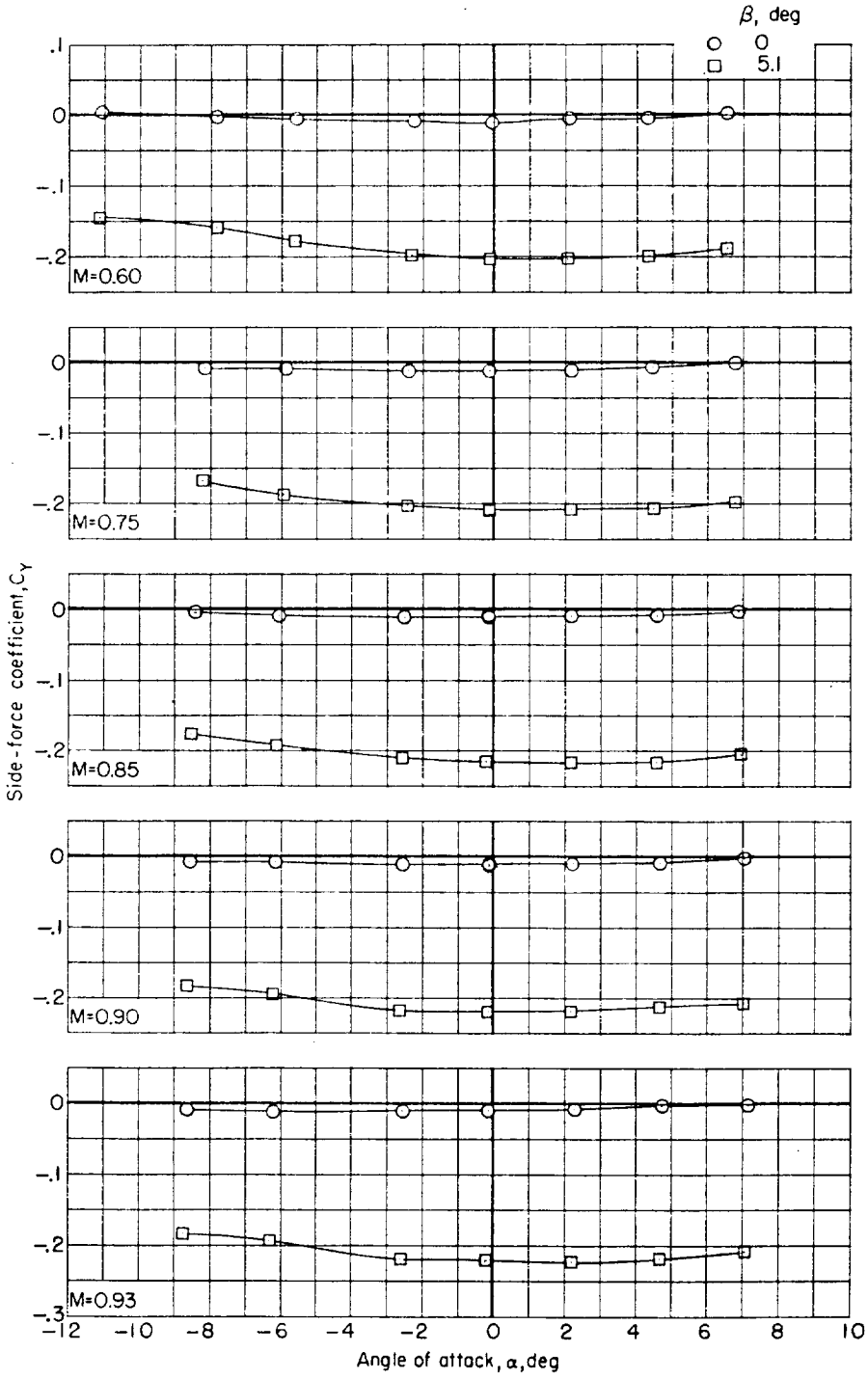

(c) Side-force coefficient.

Figure 14.- Continued.

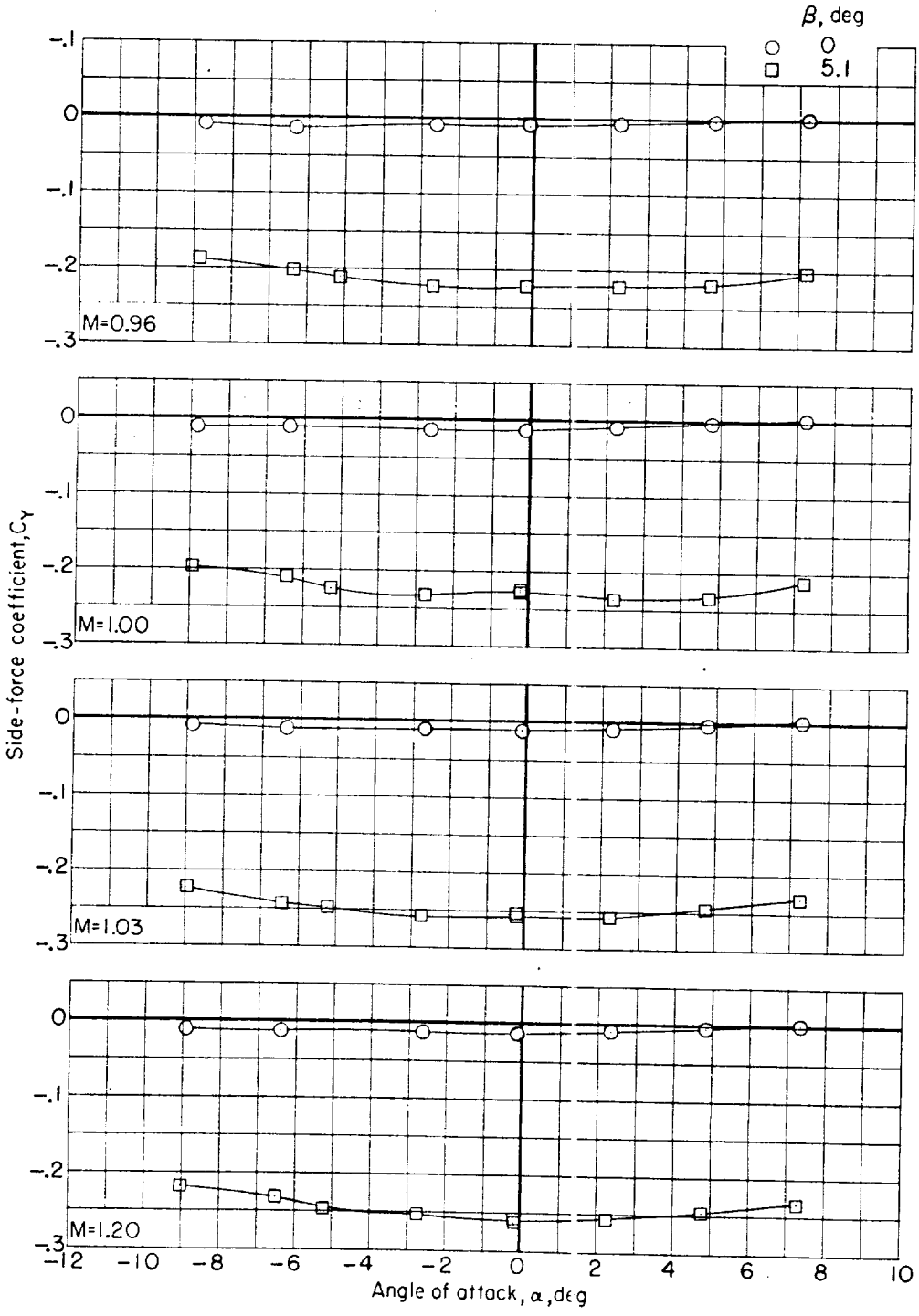

(c) Side-force coefficient. Concluded.

Figure 14.- Concluded.

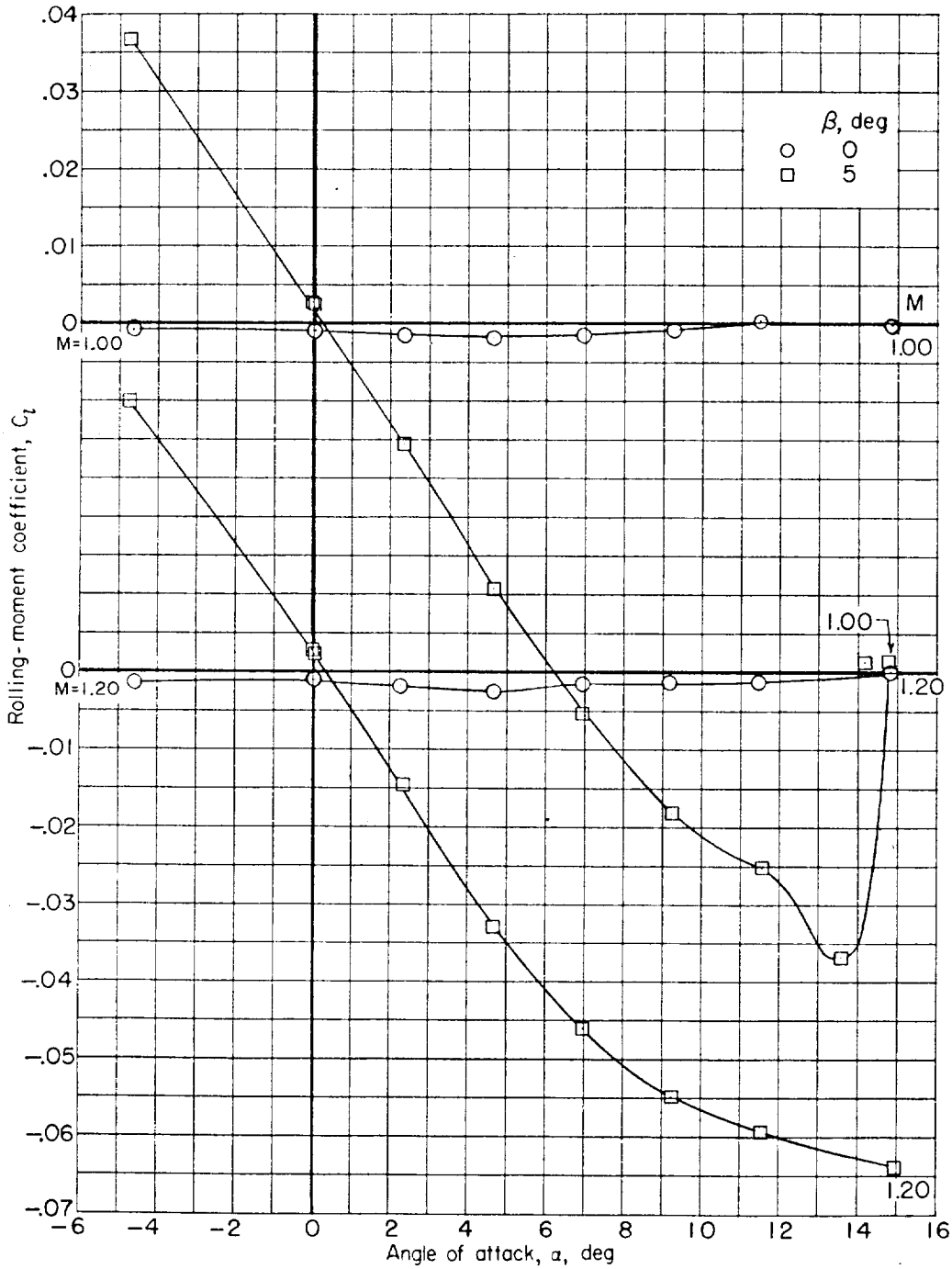

(a) Rolling-moment coefficient.

Figure 15.- Effect of sideslip angle on the aerodynamic characteristics for model without boosters. $\delta_c = 0^\circ$; spoilers off; $p_t = 0.43$ atm.

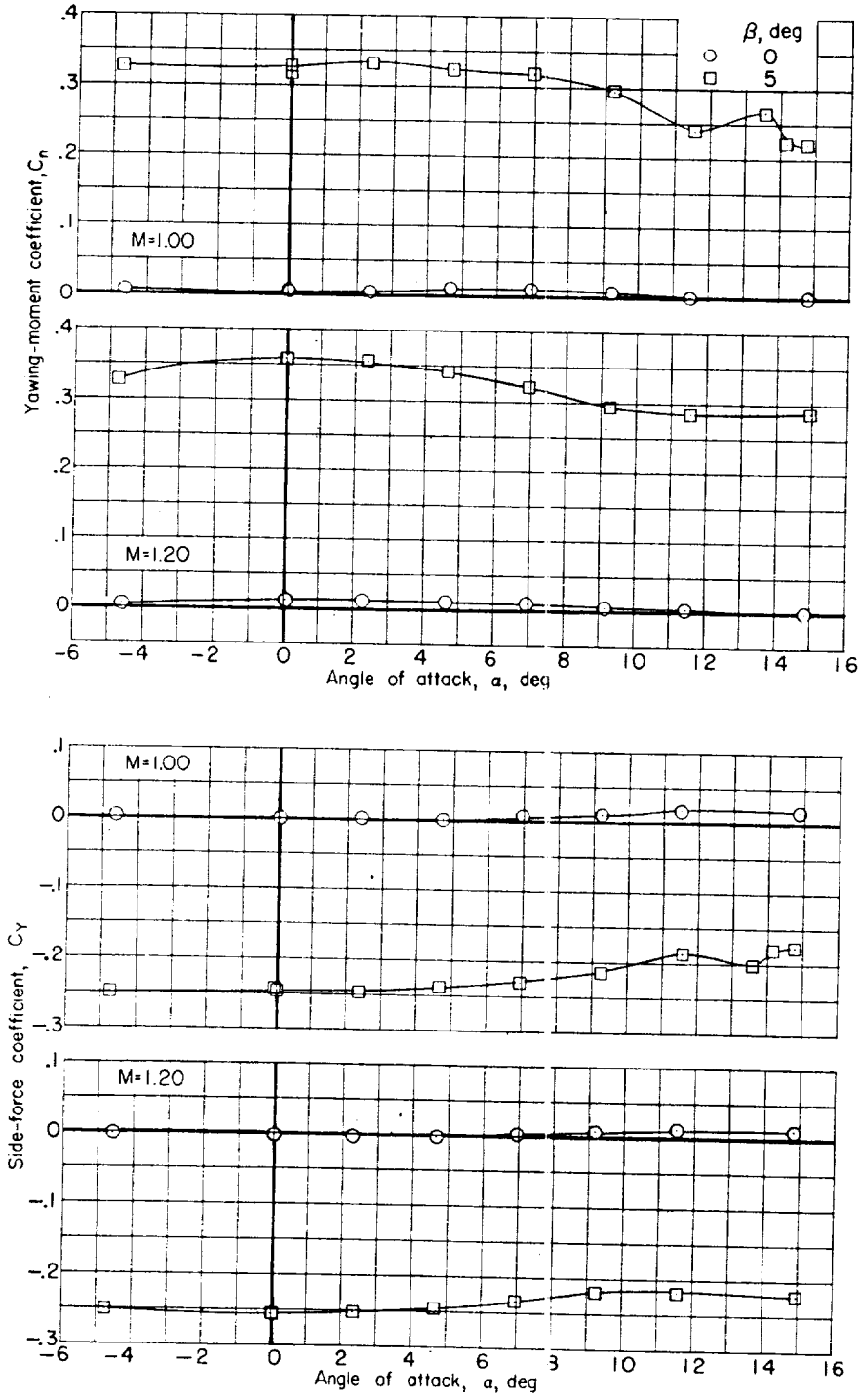

(b) Yawing-moment and side-force coefficients.

Figure 15.- Concluded.

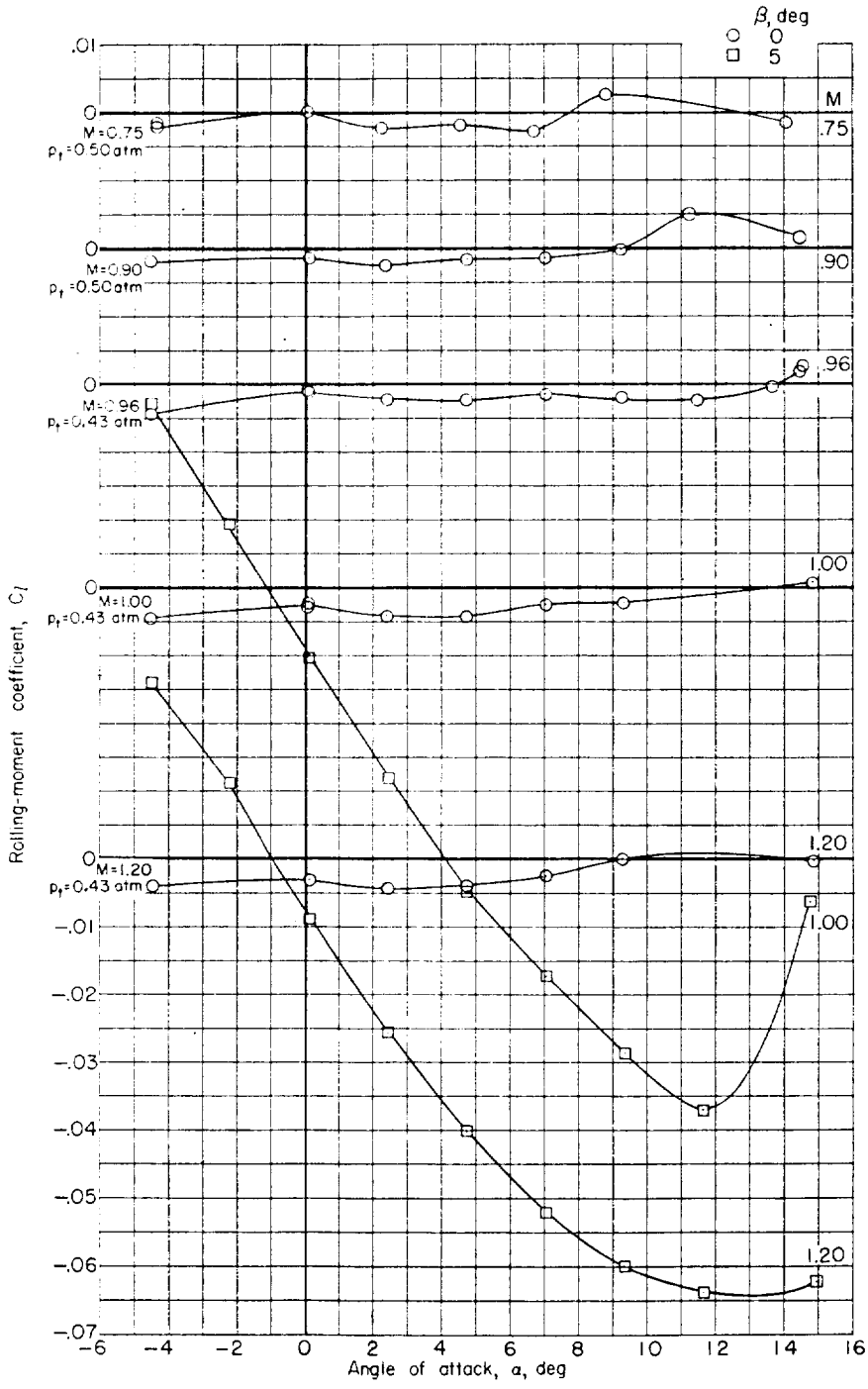

(a) Rolling-moment coefficient.

Figure 16.- Effect of sideslip angle on the aerodynamic characteristics for model without boosters. $\delta_c = 5^\circ$; spoilers off.

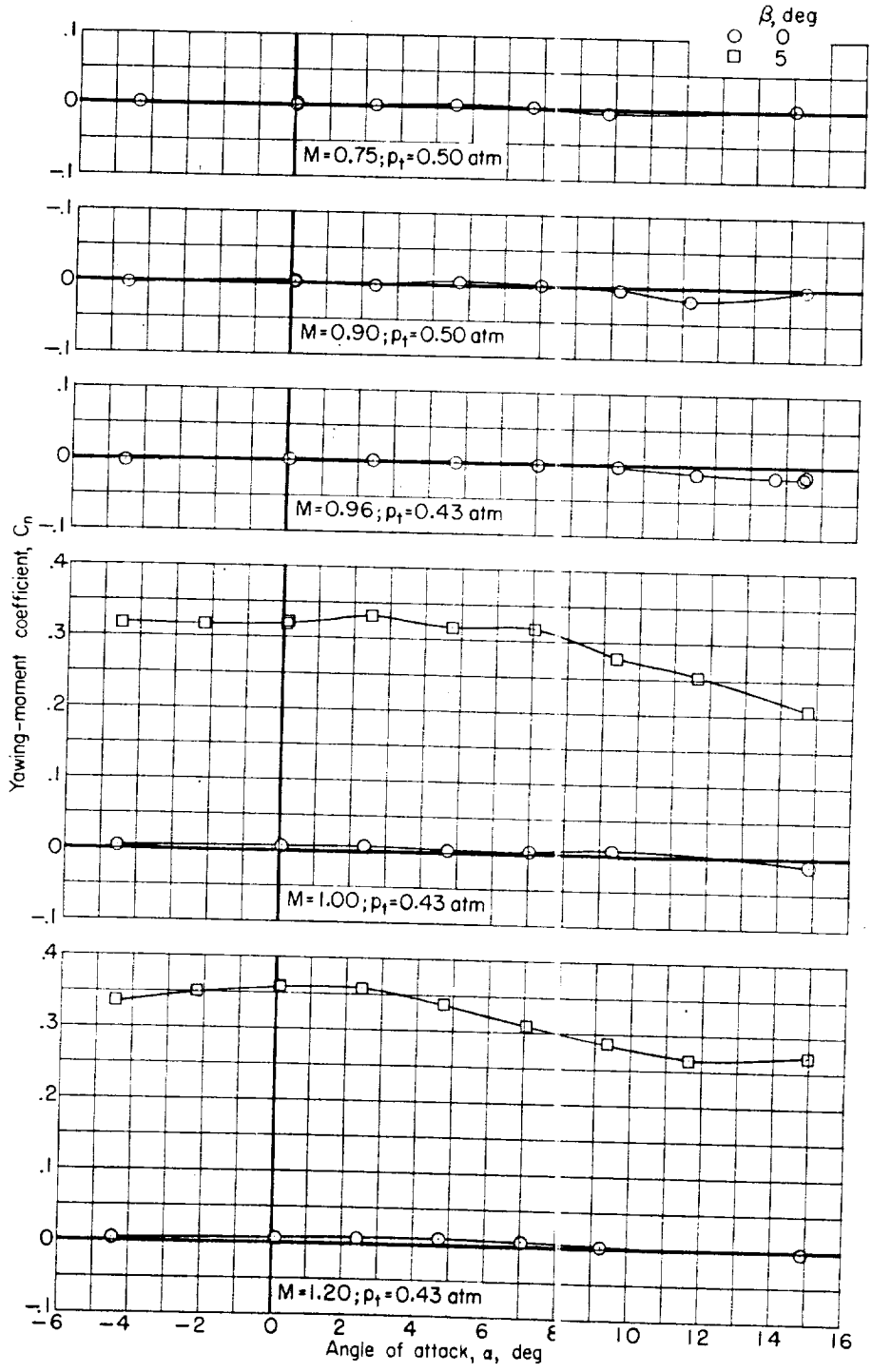

(b) Yawing-moment coefficient.

Figure 16.- Continued.

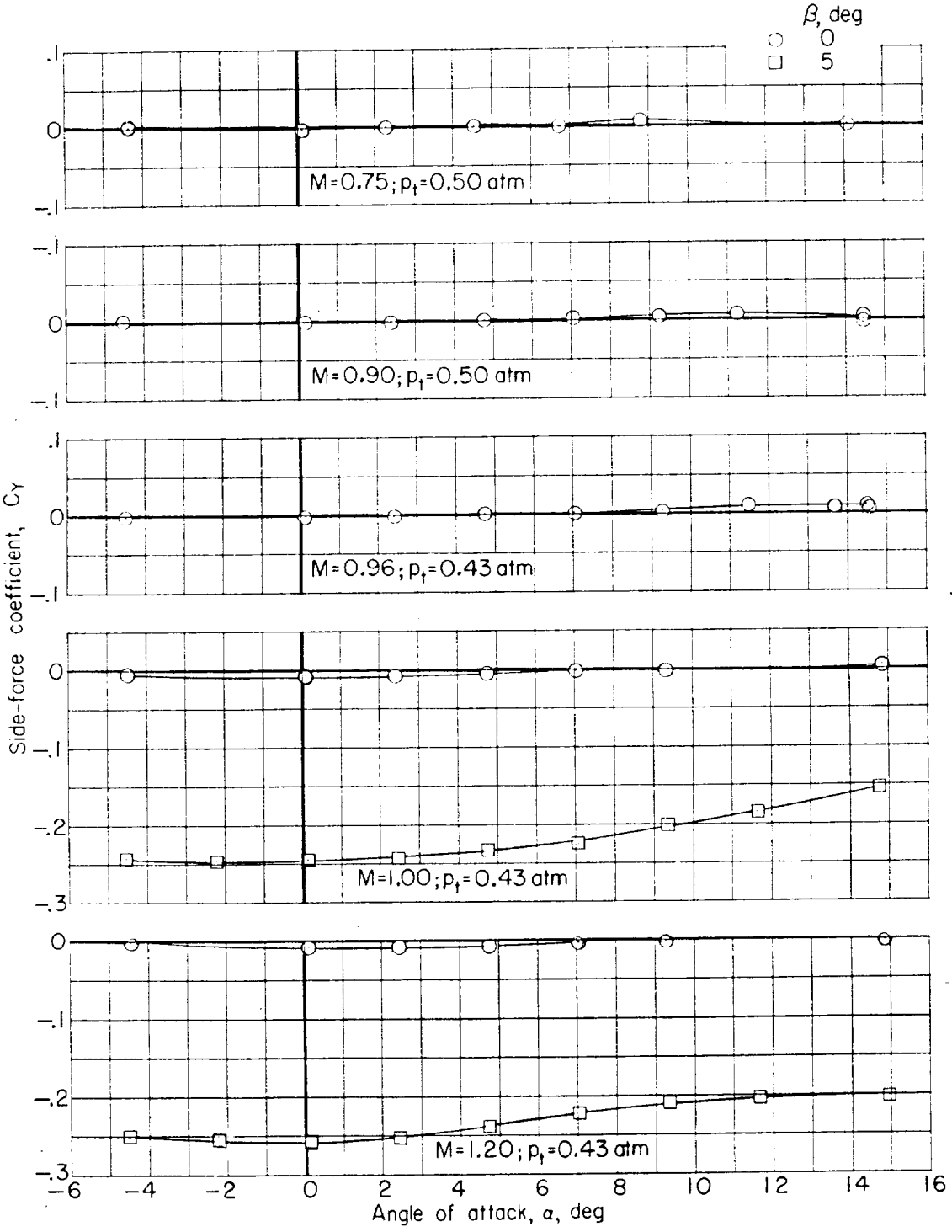

(c) Side-force coefficient.

Figure 16.- Concluded.

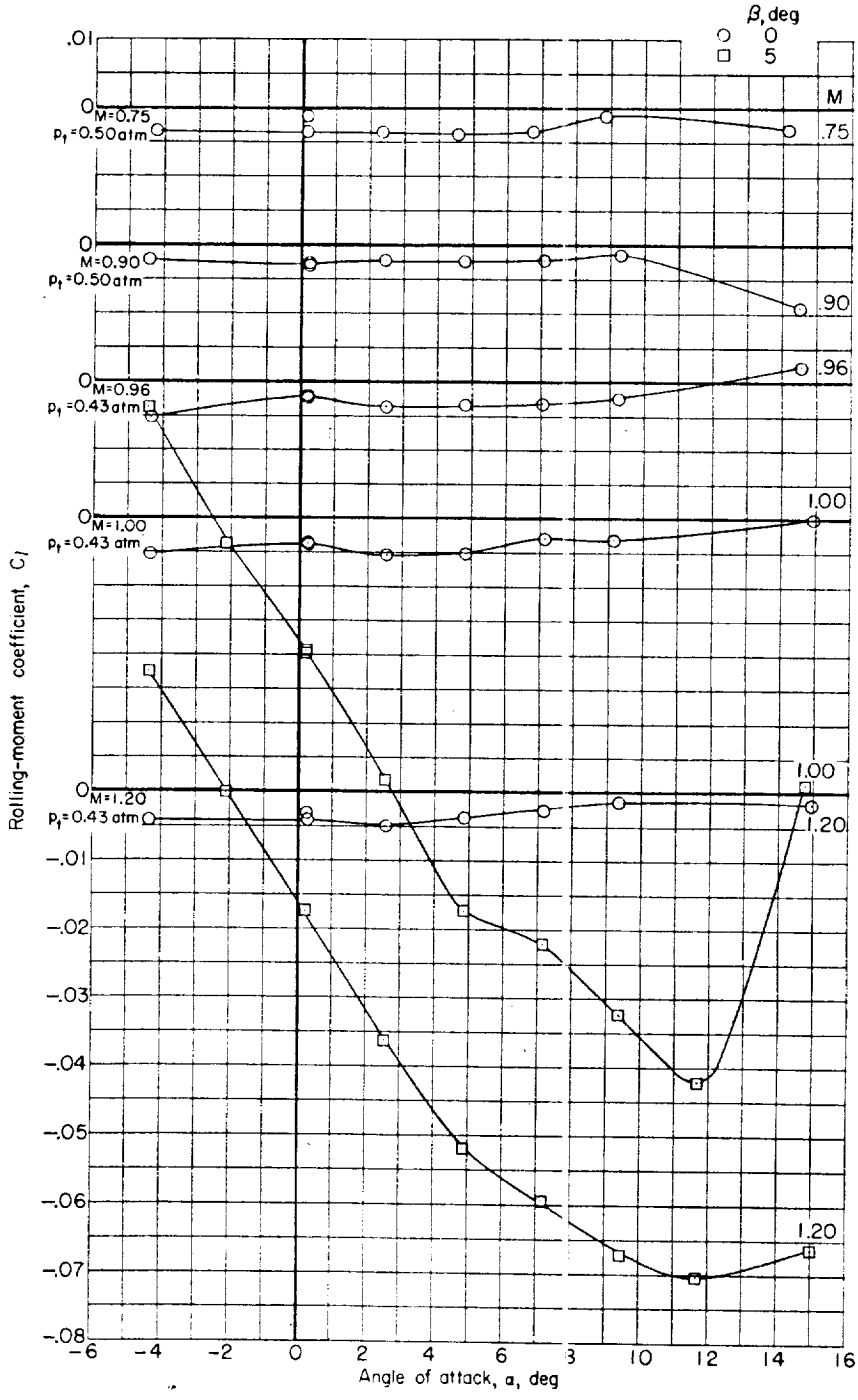

(a) Rolling-moment coefficient.

Figure 17.- Effect of sideslip angle on the aerodynamic characteristics for model without boosters. $\delta_c = 10^\circ$; spoilers off.

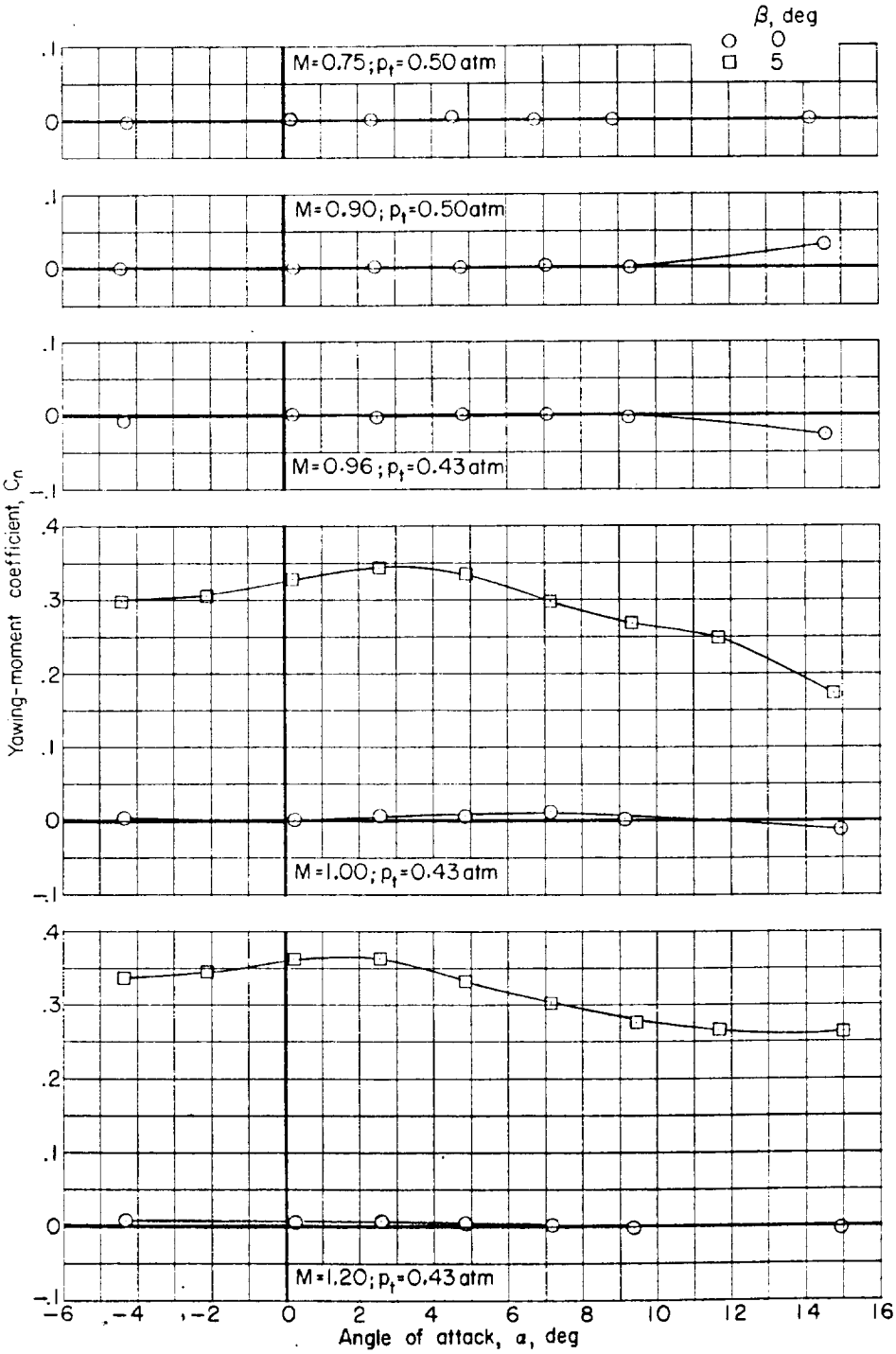

(b) Yawing-moment coefficient.

Figure 17.- Continued.

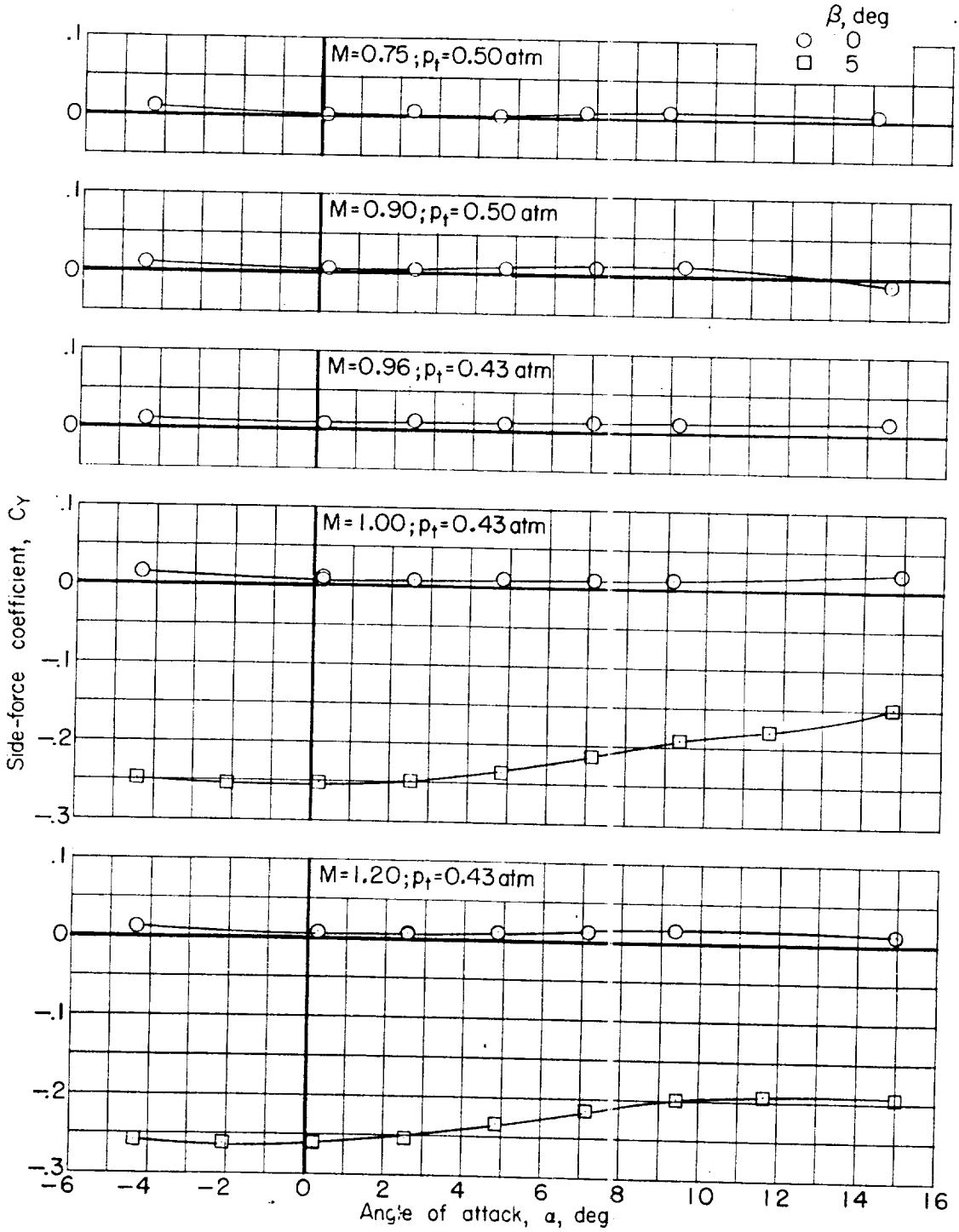

(c) Side-force coefficient.

Figure 17.- Concluded.

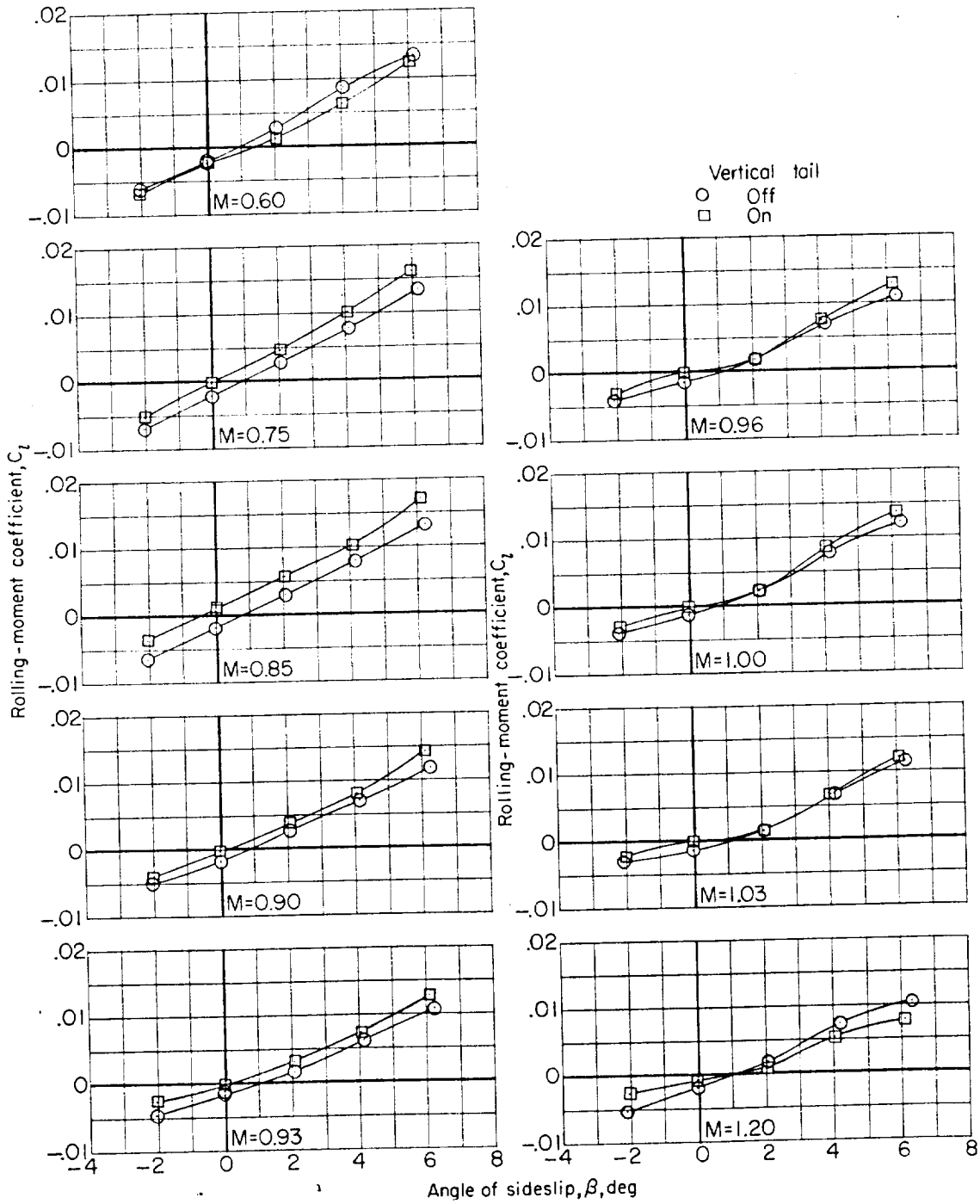

(a) Rolling-moment coefficient.

Figure 18.- Effect of vertical tail on the aerodynamic characteristics in sideslip for model with boosters. $\alpha \approx 0^\circ$; p_t = 0.50 atm.

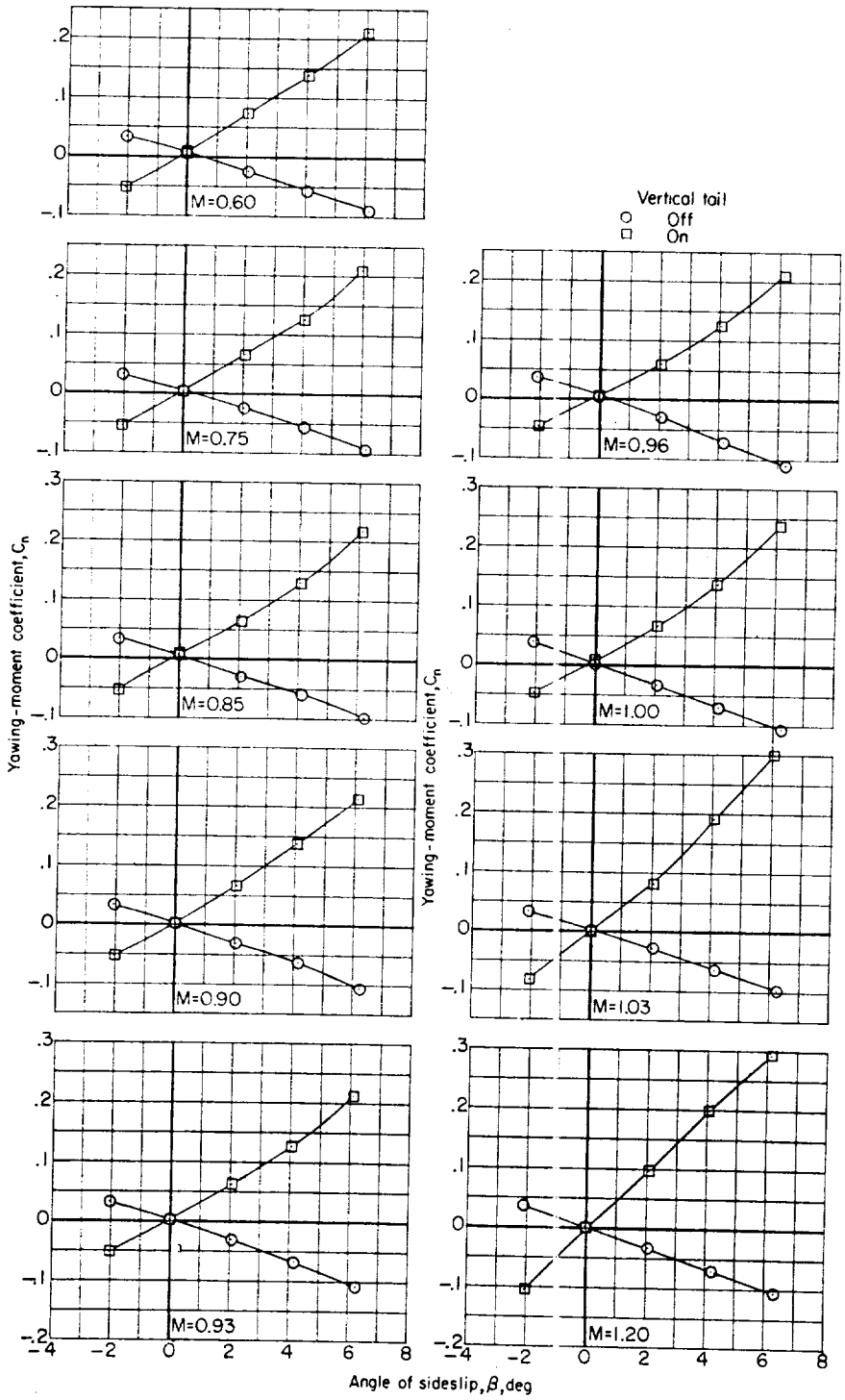

(b) Yawing-moment coefficien..

Figure 18.- Continued.

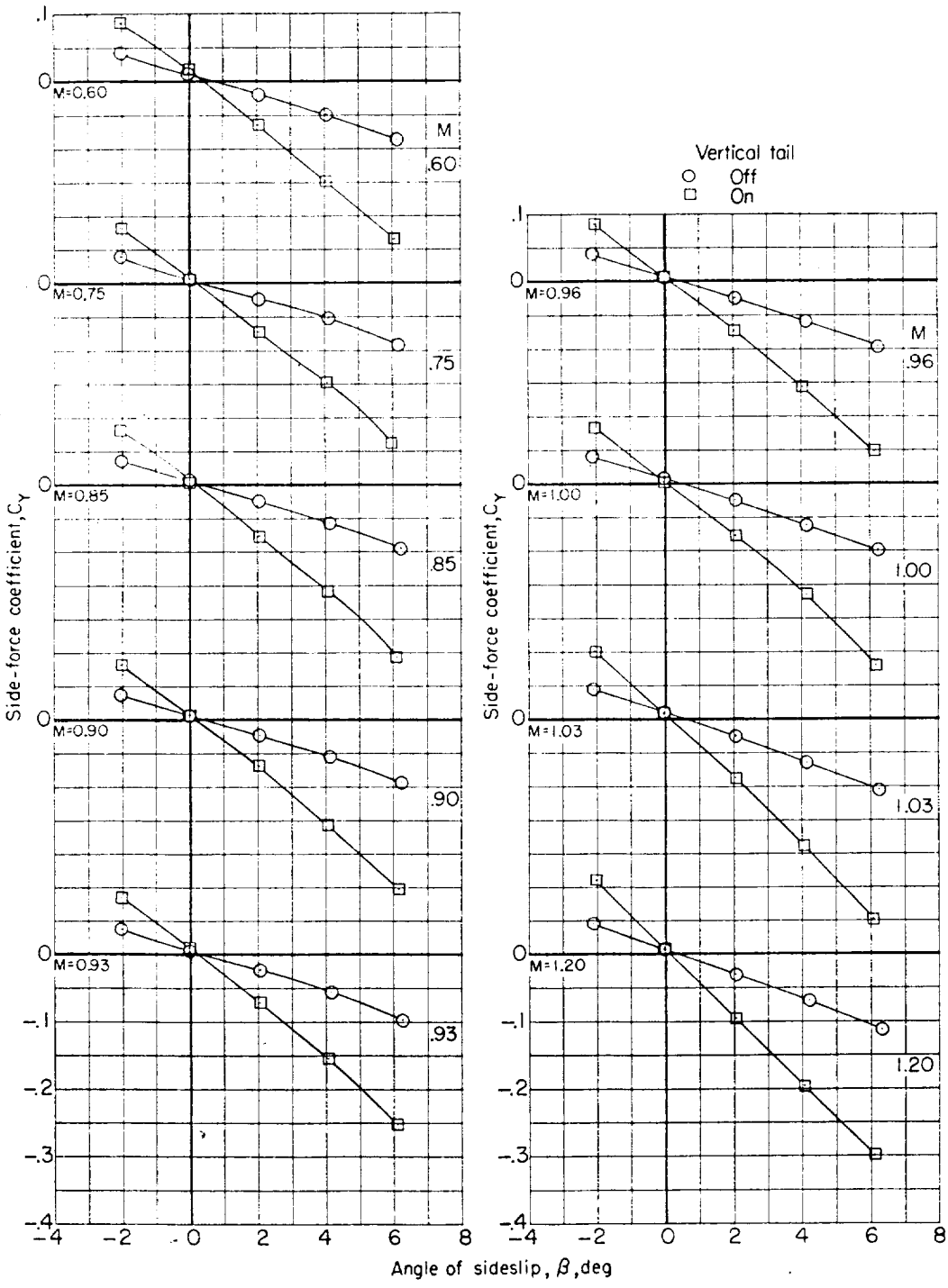

(c) Side-force coefficient.

Figure 18.- Concluded.

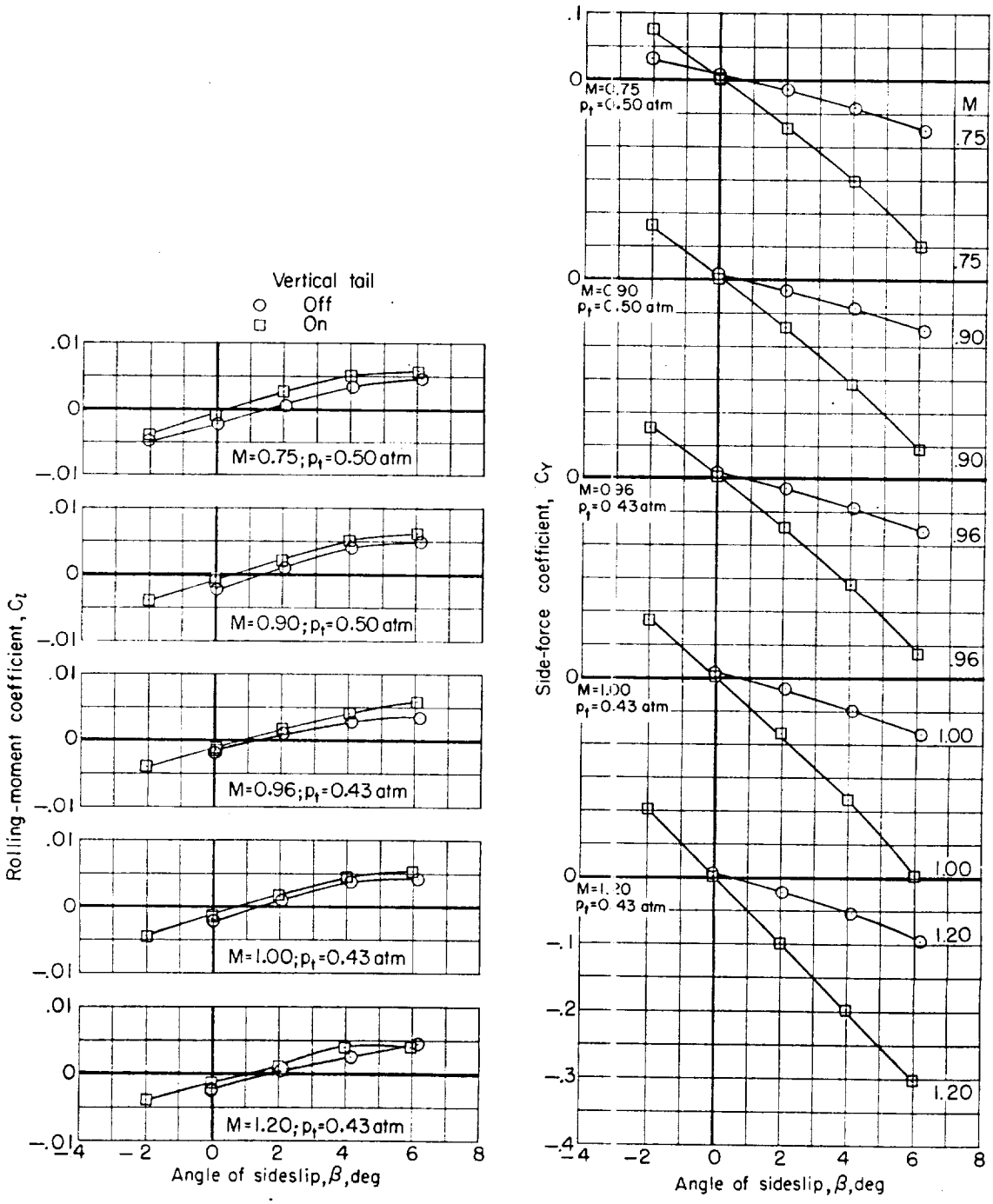

(a) Rolling-moment and side-force coefficients.

Figure 19.- Effect of vertical tail on the aerodynamic characteristics in sideslip for model without boosters. $\alpha \approx 0°$.

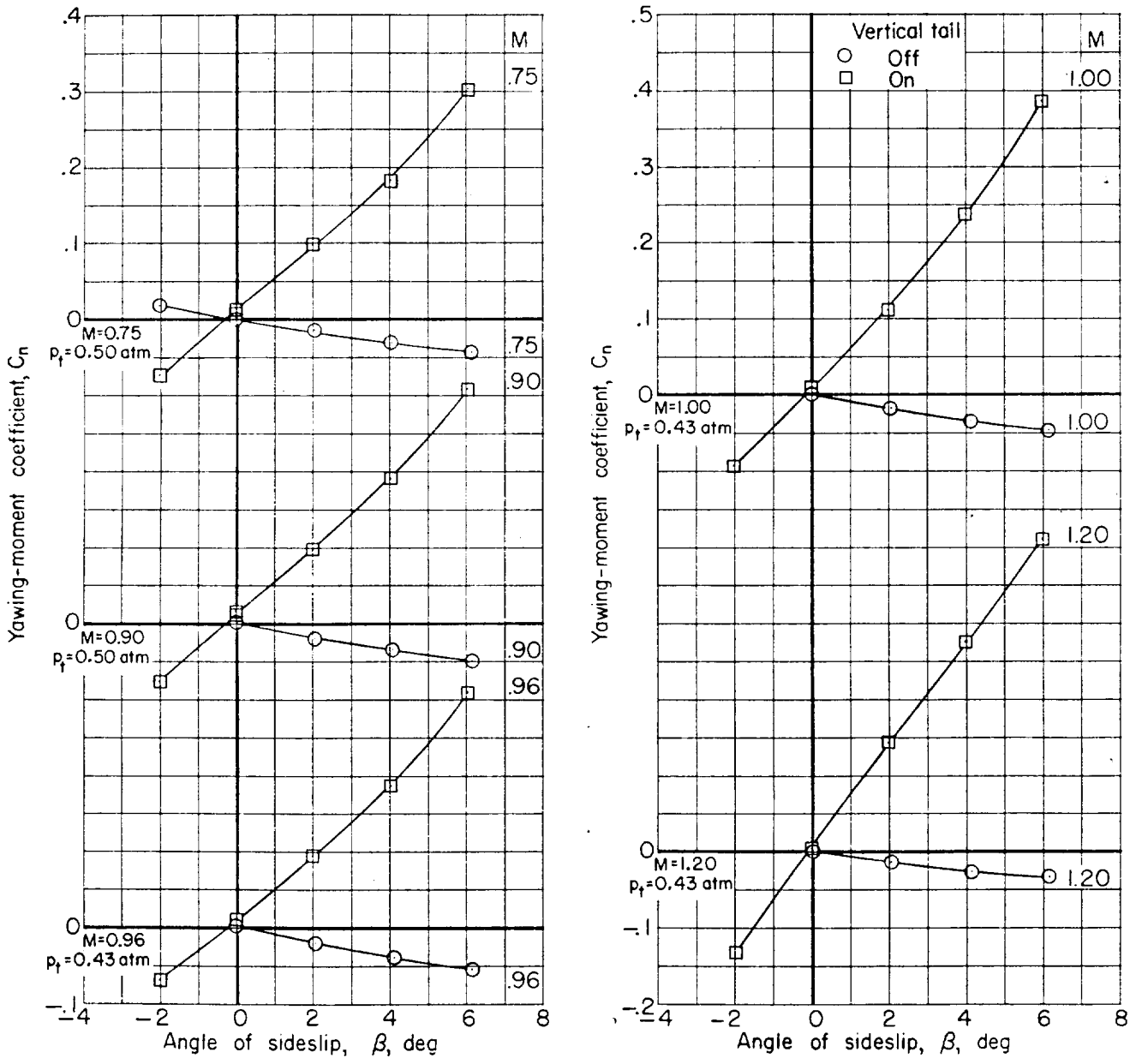

(b) Yawing-moment coefficient.

Figure 19.- Concluded.

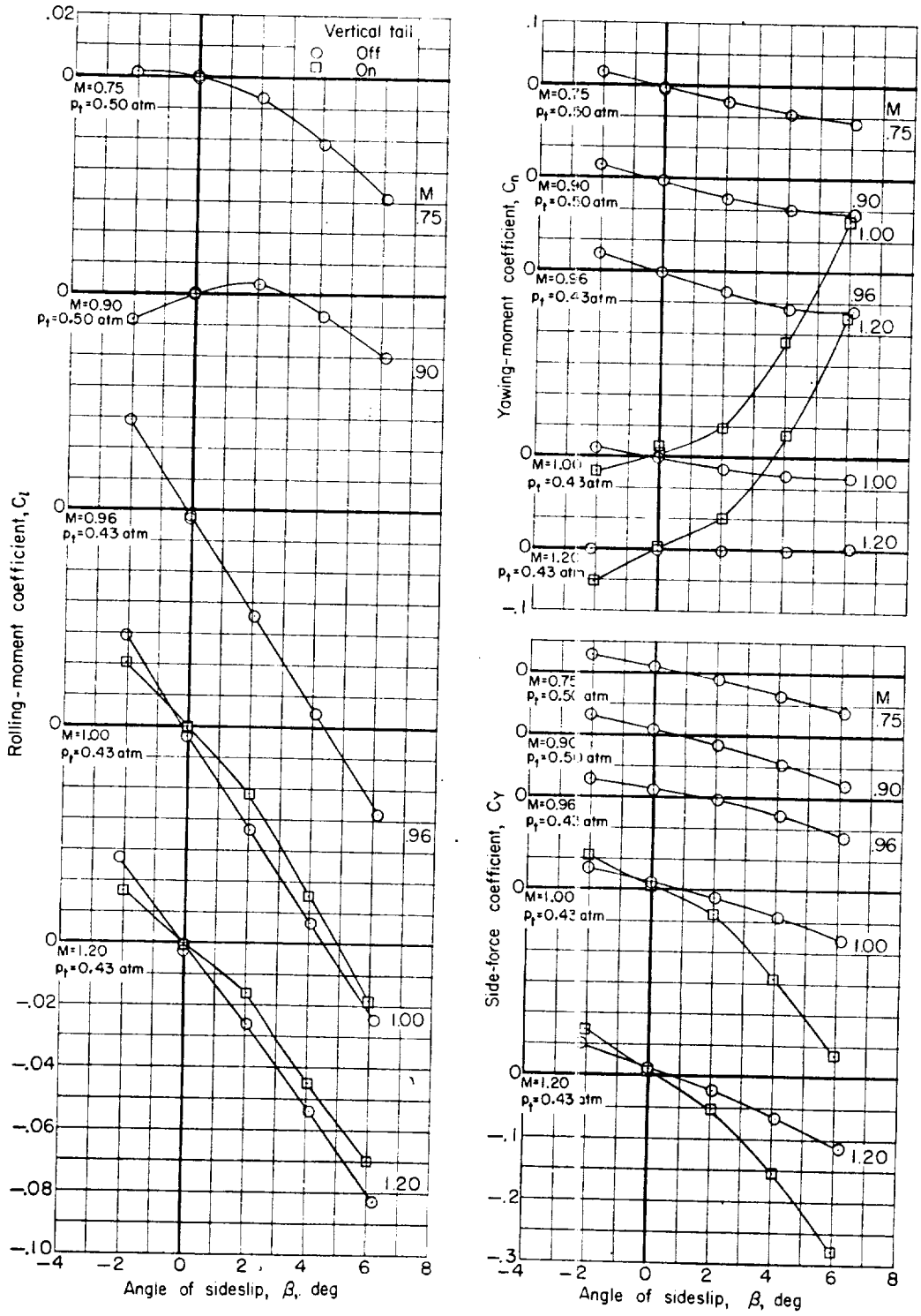

Figure 20.- Effect of vertical tail on the aerodynamic characteristics in sideslip for model without boosters. $\alpha \approx 11^\circ$.

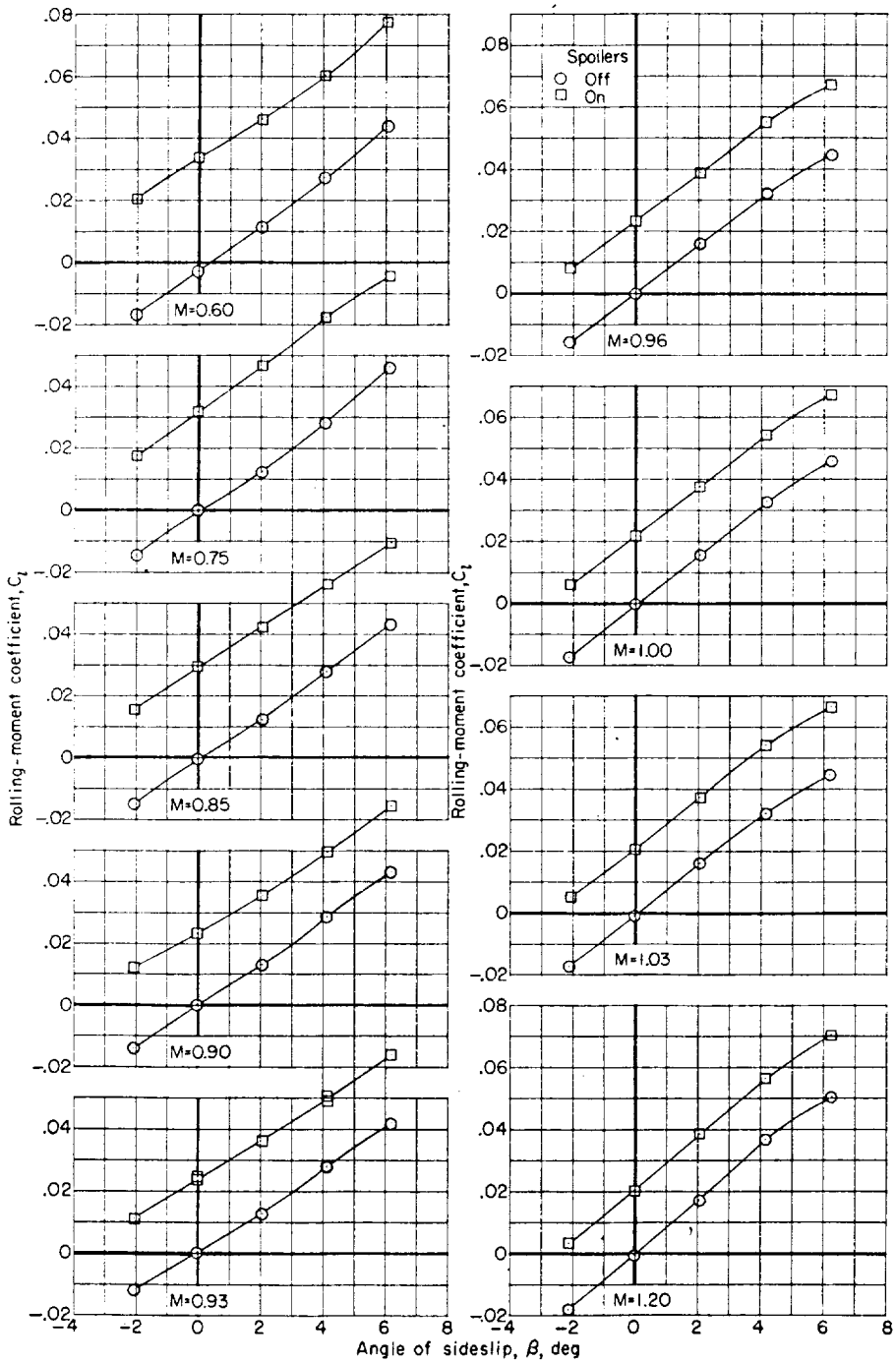

(a) Rolling-moment coefficient.

Figure 21.- Effect of spoilers on the aerodynamic characteristics in sideslip for model with boosters. $\alpha \approx -6^\circ$; $p_t = 0.50$ atm.

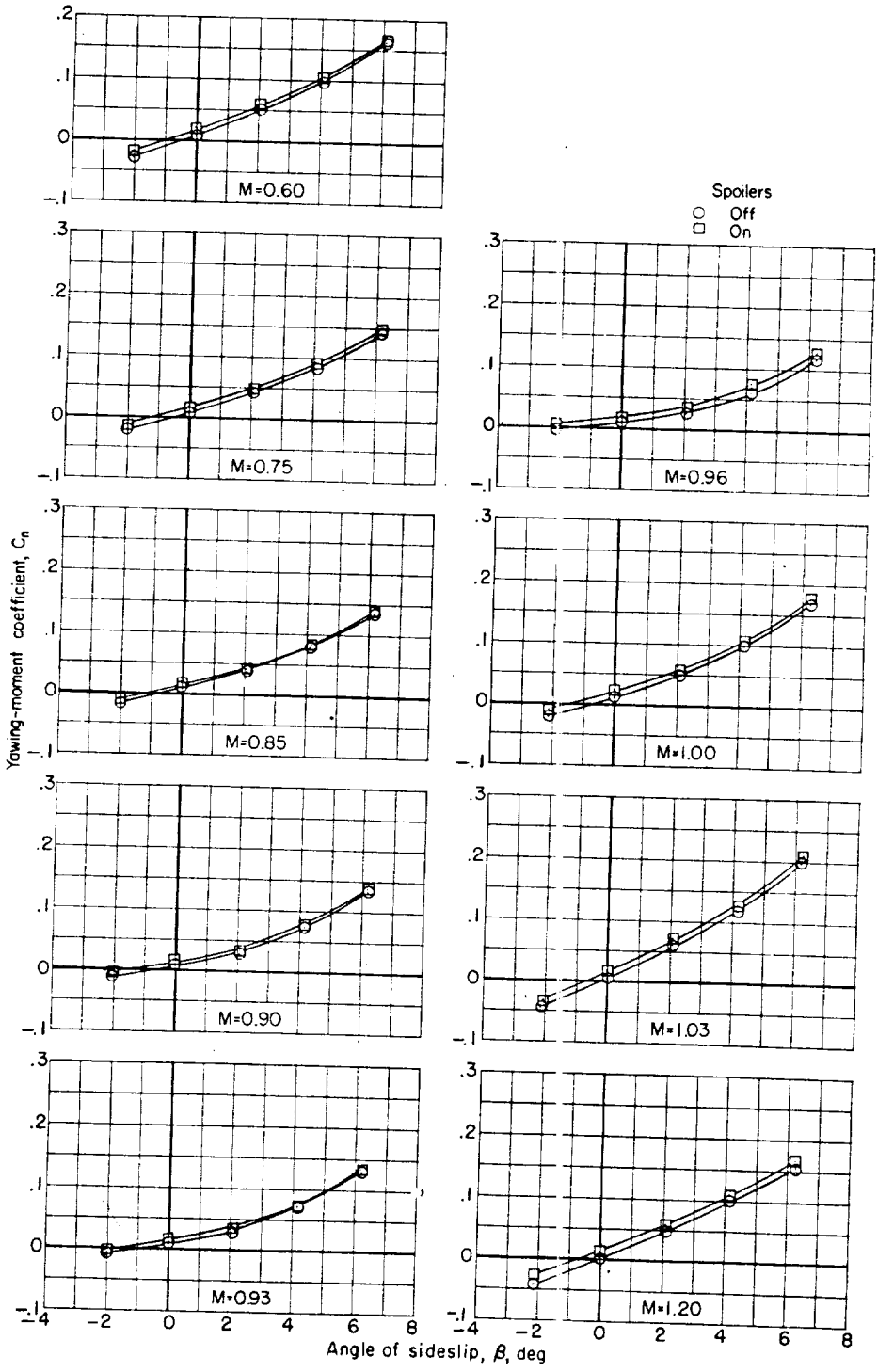

(b) Yawing-moment coefficient.

Figure 21.- Continued.

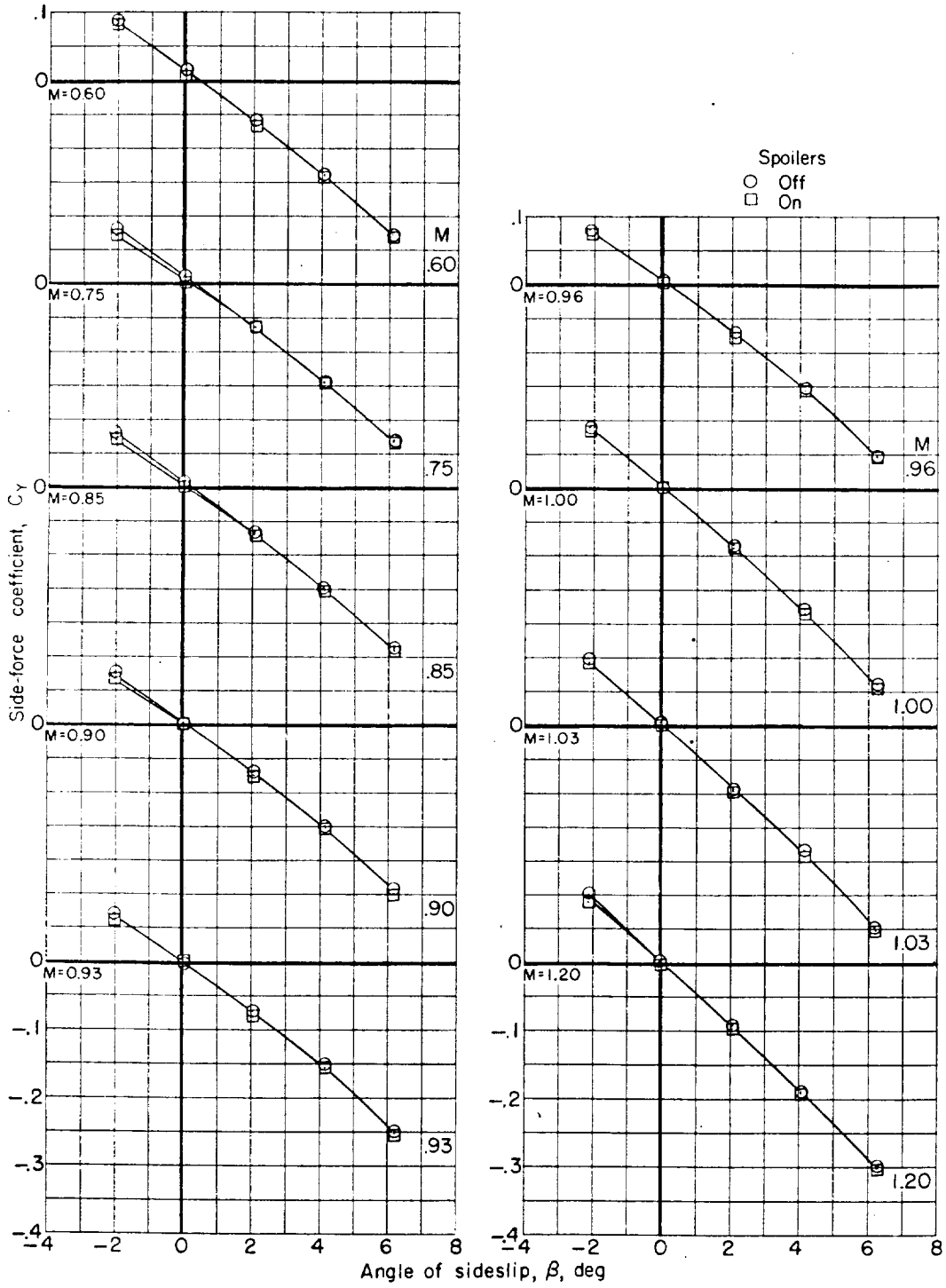

(c) Side-force coefficient.

Figure 21.- Concluded.

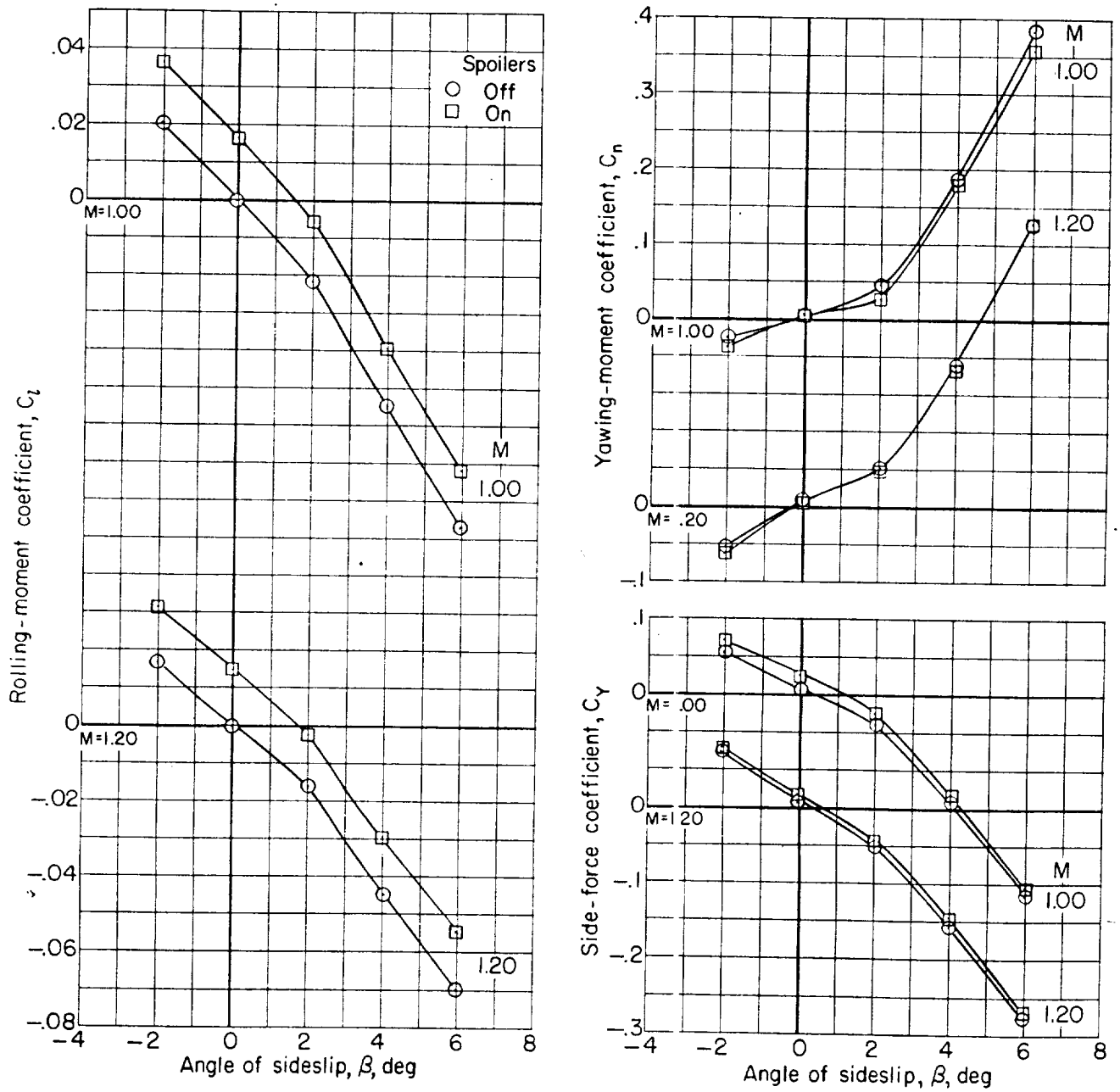

Figure 22.- Effect of spoilers on the aerodynamic characteristics in sideslip for model without boosters. $\alpha \approx 11^\circ$; $p_t = 0.43$ atm.

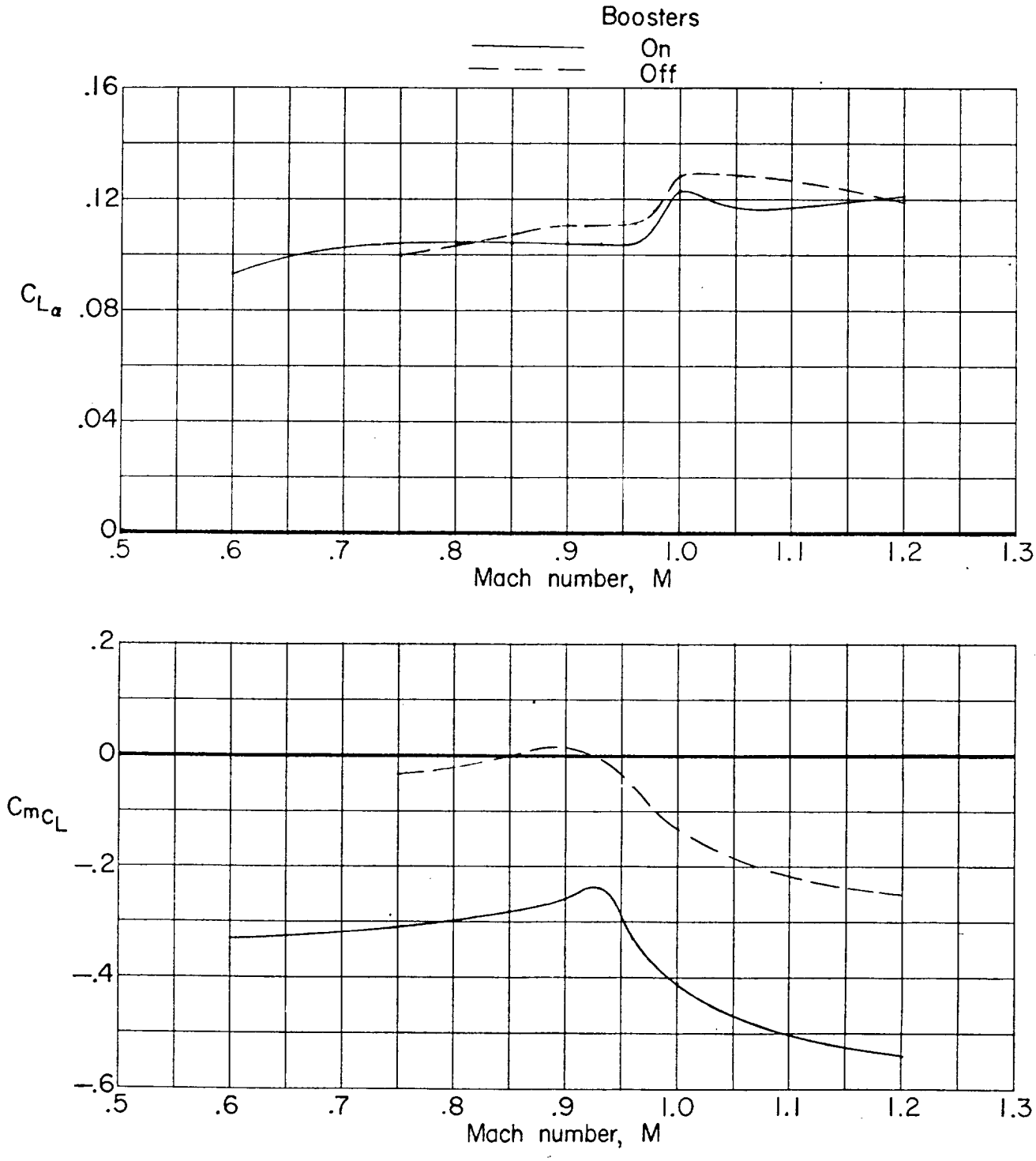

Figure 23.- Variation of lift-curve slope and static longitudinal-stability derivative (evaluated near $C_L = 0$) with Mach number for model with and without boosters. $\beta = 0°$.

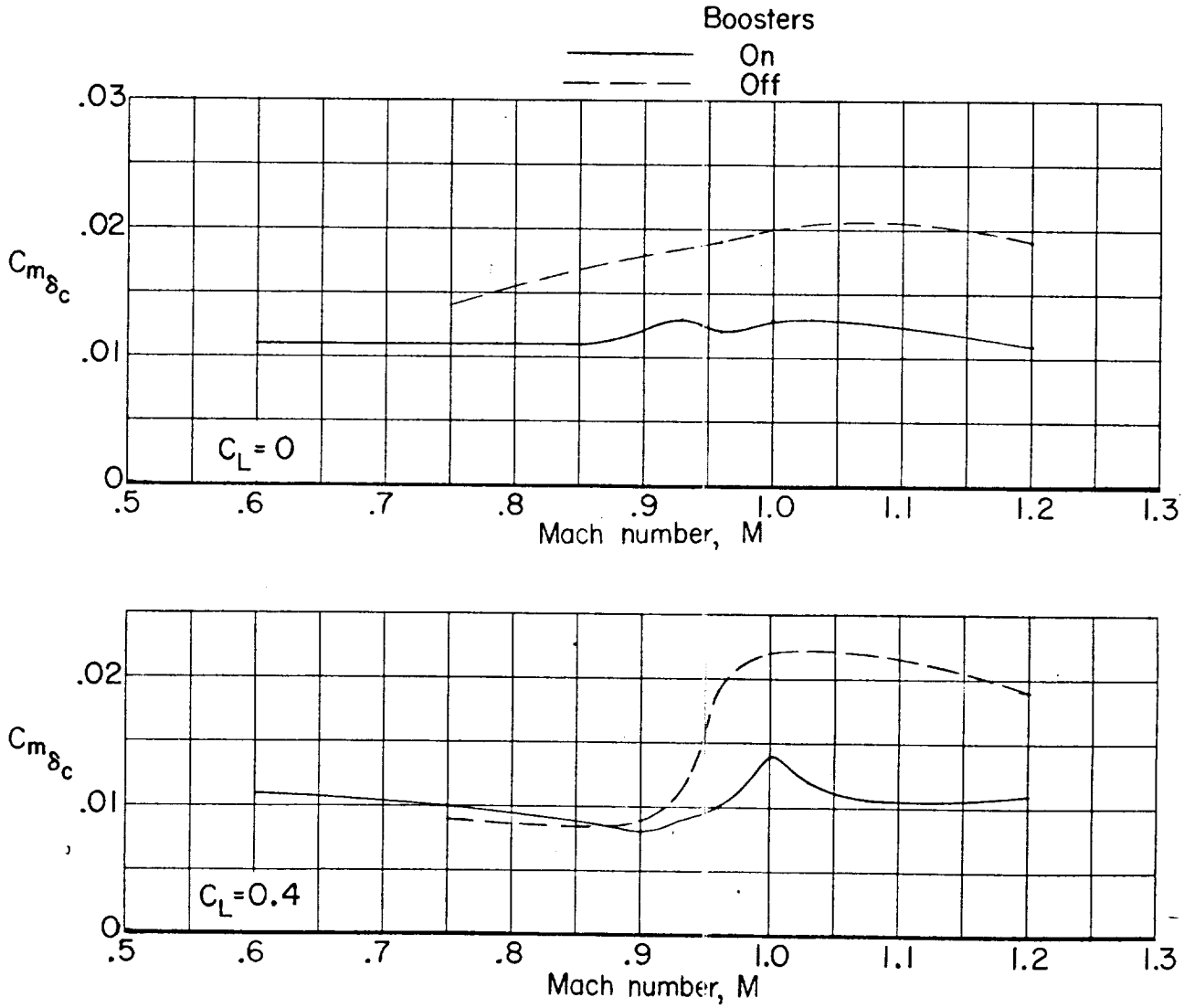

Figure 24.- Variation with Mach number of the canard effectiveness in pitch for model with and without boosters. $\beta = 0^\circ$.

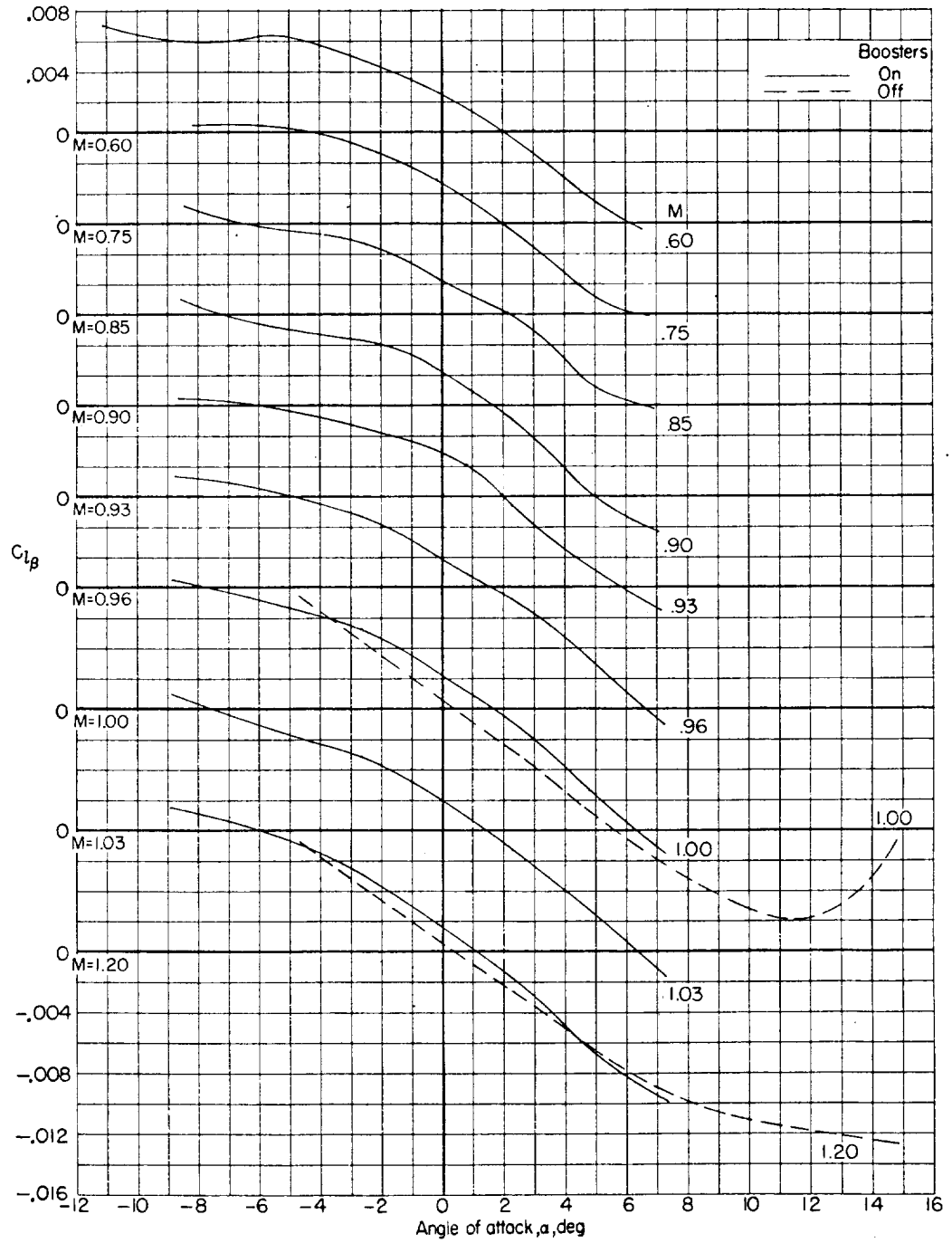

(a) Effective-dihedral derivative.

Figure 25.- Variation of sideslip derivatives with angle of attack for model with and without boosters.

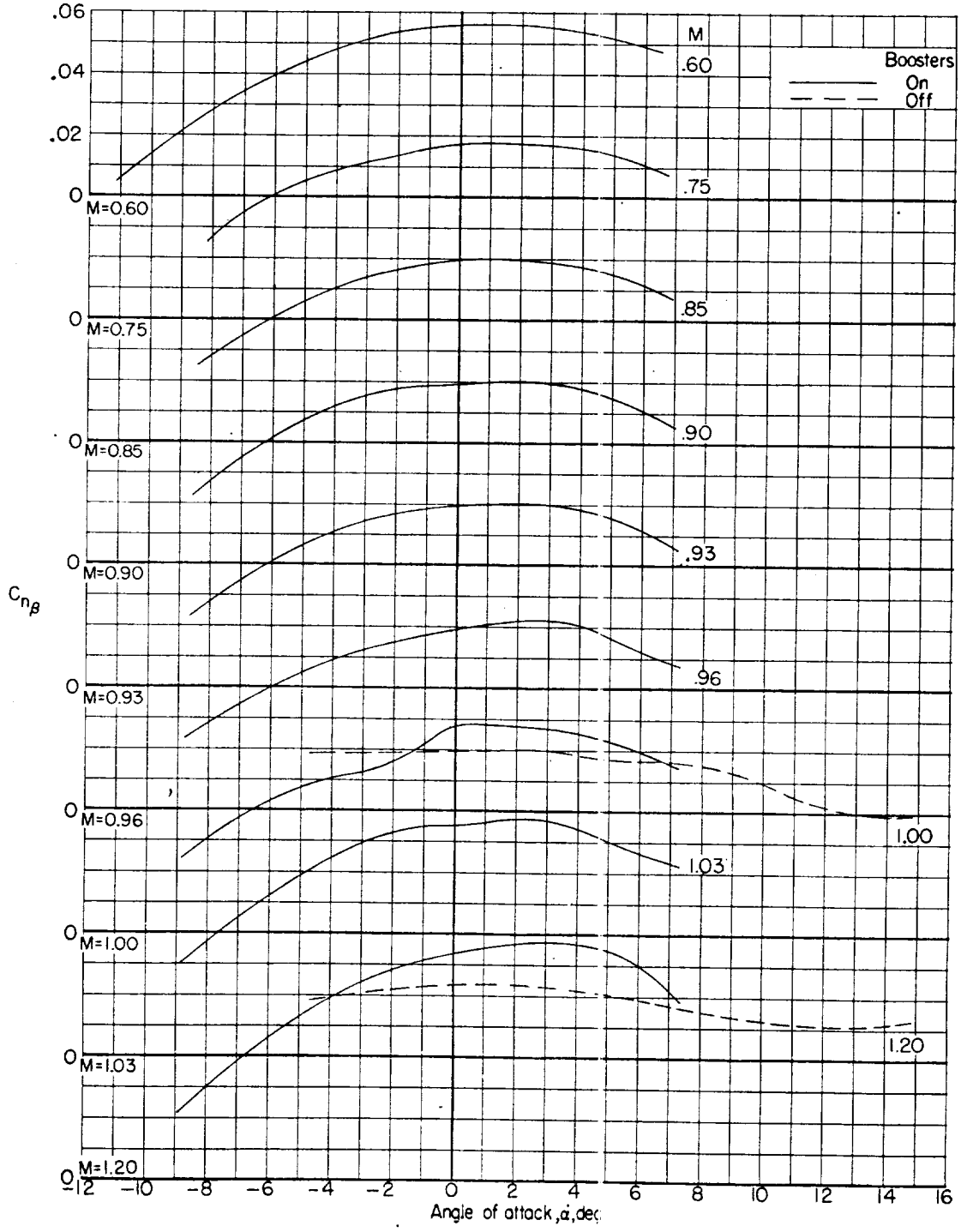

(b) Directional-stability derivative.

Figure 25.- Continued.

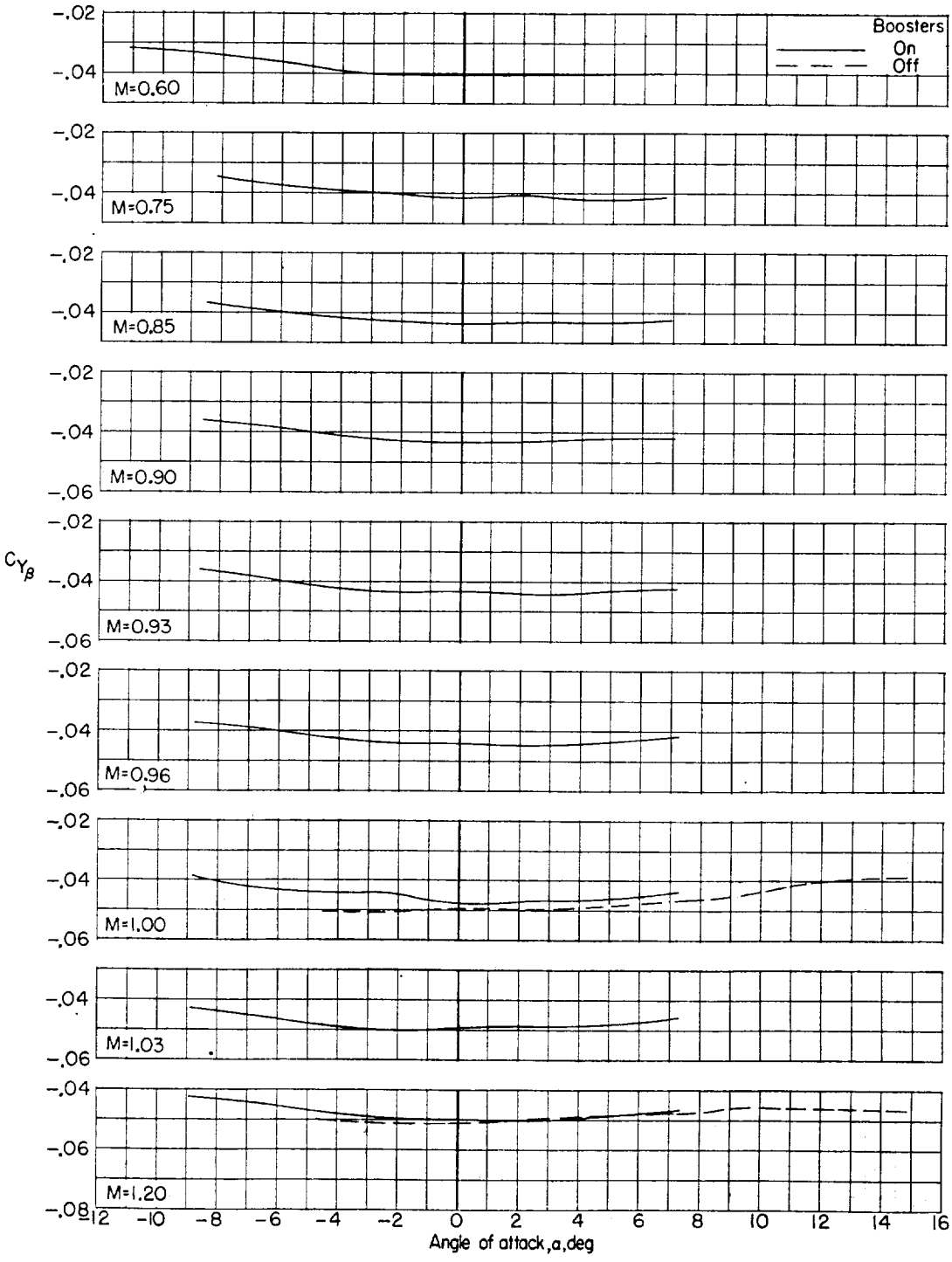

(c) Side-force derivative.

Figure 25.- Concluded.

NATIONAL AERONAUTICS AND SPACE ADMINISTRATION

TECHNICAL MEMORANDUM SX-806

for

Bureau of Naval Weapons, Department of the Navy

TRANSONIC STABILITY AND CONTROL CHARACTERISTICS OF A 1/9-SCALE MODEL OF A CANARD TARGET DRONE POWERED BY TWIN RAMJET ENGINES

By Theodore G. Ayers

ABSTRACT

Tests were conducted in the Langley 8-foot transonic pressure tunnel to determine the static longitudinal and lateral stability and control characteristics of the model at Mach numbers from 0.60 to 1.20. Pitch control was provided by a canard surface and lateral control was accomplished by off-on spoilers located outboard of the sustainer engines. The model was tested with and without boosters at combined angles of attack and sideslip.

L-3045